

THESIS

EFFECT OF ADDITIVES ON LASER IGNITION AND COMPRESSION IGNITION OF
METHANE AND HYDROCARBONS IN A RAPID COMPRESSION MACHINE

Submitted by

Andrew Boissiere

Department of Mechanical Engineering

In partial fulfillment of the requirements

For the Degree of Master of Science

Colorado State University

Fort Collins, Colorado

Fall 2016

Master's Committee:

Advisor: Anthony Marchese

Co-Advisor: Azer Yalin

Alan Van Orden

Copyright by Andrew Boissiere 2016

All Rights Reserved

ABSTRACT

EFFECT OF ADDITIVES ON LASER IGNITION AND COMPRESSION IGNITION OF METHANE AND HYDROCARBONS IN A RAPID COMPRESSION MACHINE

Despite recent efforts to develop new energy systems that do not rely on combustion of fossil fuels, internal combustion (IC) engines powered on fossil fuels (i.e. gasoline, diesel or natural gas) will remain as an integral component of the global energy portfolio for years to come and increasing the efficiency of IC engines will be a necessary means to reduce fossil fuel consumption and greenhouse gas emissions. In this study, the effect of fuel additives on natural gas and gasoline spark ignited engines were investigated using laser ignition and compression ignition experiments performed in a rapid compression machine (RCM). The goal of the laser ignition study was to examine the effect of additives to extend the lean limit of natural gas engines, while the goal of the compression ignition experiments were to examine the ability of fuel additives to decrease knock propensity of gasoline fuels.

For the laser ignition study, methane/air mixtures containing various fuel additives at temperatures and pressures representative of the compressed conditions inside an internal combustion engine were ignited in the RCM. An Nd:YAG laser operating at a wavelength of 1064 nm was used to ignite methane/air mixtures ranging in equivalence ratio from stoichiometric down to 0.4 using a rapid compression machine (RCM). Experiments were conducted to determine the lean limit, minimum spark energy (MSE), and minimum ignition energy (MIE). Three different fuel additives at varying concentrations were tested. The results show that laser ignition exhibits a stochastic behavior which must be interpreted statistically. A

90% probability of occurrence is used to evaluate the MSE and MIE which resulted in $MSE_{90}=2.3$ mJ and $MIE_{90}=7.2$ mJ for methane/air mixtures of equivalence ratio equal to 0.4. The lean limit, defined as greater than 90% of the theoretically possible heat release, was found as equivalence ratio of 0.47 for methane/air mixtures. All three fuel additives resulted in a reduction of the baseline methane/air MIE, while only DTBP and NM resulted in a reduction of the lean limit.

For the compression ignition study, the effects of various fuel additives on the auto-ignition characteristics of gasoline reference fuels were studied in the RCM. Fuel additives were added to stoichiometric fuel/air mixtures of liquid gasoline surrogate fuels and were auto-ignited in a RCM. Experiments were conducted to determine the ignition delay, heat release rate, and net heat release of the gasoline surrogate/air mixtures with and without fuel additives. Five different gasoline fuel additives were tested in an Iso-Octane and Toluene Reference base fuel. The results show that the majority of the additives increased the reactivity and decreased the ignition delays of the base fuels. However, a select few of the tested additives decreased the reactivity and increased the ignition delays of the base fuel at select conditions, which could be beneficial to increasing the efficiency of internal combustion engines.

ACKNOWLEDGEMENTS

I would never have accomplished this journey without the patient assistance and guidance of many people. First and foremost, a massive thanks to Dr. Anthony Marchese for his unwavering support, guidance, and Friday afternoon libations. Thank you to Dr. Marc Baumgardner for investing such a significant amount of time teaching me about the CSU Rapid Combustion Machine and always replying to my frantic emails for help. Ciprian Dumitrache provided never ending laser, optic, and MATLAB assistance throughout my time at the Powerhouse. Thank you to Dr. Azer Yalin for introducing me to the world of lasers and spectroscopy. Thank you to Dr. Daniel Olsen for exponentially expanding my knowledge of internal combustion engines. Thomas Falloon and Colin Gould assisted significantly in countless tasks throughout my time at CSU. Andrew Hockett and Siddhesh Bhoite contributed significant modeling assistance and provided many a sanity check. Thank you to Pat Meier and Eoghan Lavelle at Marine Technology Limited in Galway, Ireland for providing all the RCM technical assistance necessary to bring this project to fruition. Immense thanks to the sponsor of this research. Finally, thank you to my family for supporting me throughout this entire process.

TABLE OF CONTENTS

ABSTRACT.....	ii
ACKNOWLEDGEMENTS.....	iv
LIST OF TABLES.....	vii
LIST OF FIGURES.....	viii
1 INTRODUCTION.....	1
1.1 Motivation.....	1
1.2 Natural gas.....	2
1.3 Previous Research on Natural Gas Additives.....	4
1.4 Laser Ignition.....	8
1.5 Gasoline.....	18
1.6 Thesis Overview.....	22
2 EXPERIMENTAL SETUP.....	24
2.1 Rapid Compression Machine.....	24
2.2 Fuel Blending System.....	28
2.2.1 Pressure Sensors.....	30
2.2.2 Liquid Fuel Mixing Tanks.....	31
2.2.3 Gas Bottles.....	33
2.2.4 Gas Manifold.....	33
2.2.5 Temperature Control System.....	34
2.3 Laser ignition Setup.....	34
2.3.1 Laser.....	35
2.3.2 Optical plug.....	36
2.3.3 Steering and Measuring Optics.....	37
2.4 High Speed Schlieren Imaging System.....	38
2.5 Data Analysis.....	40
2.5.1 Minimum Spark Energy (MSE) and Minimum Ignition Energy (MIE).....	41
2.5.2 Calculation of Apparent Rate of Heat Release.....	43
2.5.3 Lean Limit.....	44
3 THE EFFECT OF ADDITIVES ON LASER IGNITION OF LEAN PREMIXED NATURAL GAS/AIR MIXTURES.....	46
3.1 Ignition of Methane/Air Mixtures.....	46
3.1.1 Lean Limit Measurements.....	49

3.1.2	Minimum Ignition Energy	52
3.1.3	Schlieren Imaging	53
3.2	Investigation of Additives for Spark Ignited Natural Gas Engines.....	54
3.2.1	Effect of Additives on Auto-ignition of Methane/Air Mixtures	55
3.2.2	Effect of Additives on Minimum Ignition Energy of Methane/Air Mixtures	58
3.2.3	Effect of Additives on Lean Limit of Methane/Air Mixtures	62
4	THE EFFECT OF ADDITIVES ON HOMOGENEOUS AUTO-IGNITION OF GASOLINE SURROGATE FUELS	65
4.1	CHEMKIN Modeling.....	65
4.2	Isooctane Ignition Delay Experiments	71
4.3	Toluene Reference Fuel Ignition Delay Testing	76
4.4	Gasoline Fuel Additive Testing.....	80
5	CONCLUSIONS AND FUTURE WORK	96
6	BIBLIOGRAPHY	99
7	APPENDIX A: RAPID COMPRESSION MACHINE OPERATION	106
7.1	Turning the Rapid Compression Machine On.....	106
7.2	Firing the Rapid Compression Machine	107
8	APPENDIX B: RAPID COMPRESSION MACHINE MAINTENANCE	110
8.1	Rapid Compression Machine Disassembly	110
8.1.1	Rapid Compression Machine Center Section Disassembly	111
8.1.2	Rapid Compression Machine End Section Disassembly	116
9	APPENDIX C: RCM SEALS	126
10	APPENDIX D: RAPID COMPRESSION MACHINE TROUBLESHOOTING	135
10.1	Combustion Chamber Valve Tip Deterioration	135
10.2	Piston Seal Deterioration.....	135
10.3	Wiper Seal Deterioration.....	136
10.4	Neck Seal Deterioration	136
10.5	Non-synchronous Piston Firing.....	137
10.6	Air Chamber Release Valve Not Closing	137
11	APPENDIX E: RCM T_C UNCERTAINTY PROPAGATION	139

LIST OF TABLES

Table 3.1 Test conditions for the laser ignited CH ₄ /Air mixtures presented in Figure 3.1.	46
Table 3.2 Test conditions for the lean limit study.	51
Table 3.3 Test conditions for the MIE and MSE investigation as described in Figure 3.5.	53
Table 4.1 Stoichiometric toluene reference fuel ignition delay calculations. Constant volume simulations were conducted with initial temperature and pressure of 634 K and 19.53 bar, respectively. Full volume trace simulations were conducted with initial temperature and pressure of 300 K and 1 bar.	77
Table 9.1 Rapid Compression Machine Seals.	126

LIST OF FIGURES

Figure 2.1 Schematic Diagram of Colorado State University Rapid Compression Machine (RCM).....	24
Figure 2.2 Colorado State University Rapid Compression Machine.....	25
Figure 2.3 RCM Creviced Piston.....	27
Figure 2.4 RCM Fuel Blending System.....	29
Figure 2.5 Schematic Drawing of Liquid Fuel Mixing Tank.	32
Figure 2.6 Laser Ignition Setup positioned next to RCM.....	35
Figure 2.7 Optical plug for focusing the laser beam inside the combustion chamber.....	36
Figure 2.8 Schematic of optical ports and combustion chamber.....	37
Figure 2.9 Experimental setup for RCM Laser Ignition System.....	38
Figure 2.10 Schematic of the bench-top setup for Schlieren Imaging.....	40
Figure 3.1 Pressure traces for laser ignition of methane-air mixtures at various equivalence ratios: $P_0=1$ bar, $T_{comp}=782$ K, and $E_{laser}=20$ mJ.	48
Figure 3.2 Top: Variation of peak pressure with equivalence ratio. Bottom: Variation of ignition delay with equivalence ratio.	49
Figure 3.3 Figure 3.3: Fraction of net heat released for various equivalence ratios. The lean limit is found to be $\phi_{90}=0.47$, $\phi_{50}=0.41$, and $\phi_{20}=0.37$	51
Figure 3.4 Left: an example of a “strong” ignition event ($\chi=0.84$). Right: A “weak” ignition event ($\chi=0.22$).	51
Figure 3.5 Probability of spark formation and ignition versus laser energy. Data was fitted using the logistic function to infer MIE and MSE.....	53
Figure 3.6 Schlieren image sequence depicting the formation of a laser spark in atmospheric air.	54
Figure 3.7 1,1-Di (tert-butylperoxy).	55
Figure 3.8 Nitromethane.	55
Figure 3.9 Dimethoxymethane.....	55
Figure 3.10 Auto-Ignition testing of 1% and 5% 1,1-Di (tert-butylperoxy) (DTBP) in lean ($\phi=0.4$), premixed methane/air mixtures in the CSU RCM.....	56
Figure 3.11 Auto-Ignition testing of 10% Nitromethane (NM) in in lean ($\phi=0.4$), premixed methane/air mixtures in the RCM.....	57
Figure 3.12 Auto-Ignition testing of 5% Dimethoxymethane (DMM) in in lean ($\phi=0.4$), premixed methane/air mixtures in the RCM.....	57
Figure 3.13 Results of Minimum Ignition Energy Testing of 1,1-Di (tert-butylperoxy).	59
Figure 3.14 Results of Minimum Ignition Energy Testing of Nitromethane (NM) in methane/air mixtures at $\phi=0.4$	60
Figure 3.15 Results of Minimum Ignition Energy testing of Dimethoxymethane.	61
Figure 3.16 Results of Continued Minimum Ignition testing of Dimethoxymethane.	62
Figure 3.17 Lean Limit Testing of 1,1-Di (tert-butylperoxy) (DTBP), Nitromethane (NM), and Dimethoxymethane (DMM).	64
Figure 4.1 RCM Volume vs. Time curve.	66

Figure 4.2 Simulated pressure vs. time for a stoichiometric blend of 30% Toluene, 20% isooctane, 50% n-heptane in air with initial conditions of 1 bar and 300 K. Computations were performed using varying volume vs. time data.....	68
Figure 4.3 Simulated pressure vs. time for a stoichiometric blend of 30% Toluene, 20% isooctane, 50% n-heptane in air with initial conditions of 1 bar and 300 K. Computations were performed using constant volume.....	69
Figure 4.4 Simulated, experimental, and published Isooctane Ignition Delay Curves.....	73
Figure 4.5 Pressure Trace from Experimental Run in the RCM of Stoichiometric isooctane/21% O ₂ /X% N ₂ /Y% Ar Mixture at a compressed temperature of 705 K.....	75
Figure 4.6 Pressure Trace from CHEMKIN Simulation of Stoichiometric Isooctane Mixture at a compressed Pressure of 705 K.....	76
Figure 4.7 Simulated and experimental Toluene Reference Fuel Ignition Delay Curves.	80
Figure 4.8 Additive 1 in TRF Base Fuel Ignition Delay Curves.	82
Figure 4.9 Additive 2 in TRF Base Fuel Ignition Delay Curves.	83
Figure 4.10 Comparison of Additive 1 and Additive 2 Performance in TRF Base Fuel.....	84
Figure 4.11 Additive 2 in Isooctane Base Fuel Ignition Delay Curve.....	87
Figure 4.12 Additive 3 in Isooctane Base Fuel Ignition Delay Curve.....	88
Figure 4.13 Diphenyl Amine in Isooctane Base Fuel Ignition Delay Curve.	89
Figure 4.14 MoDTC in Isooctane Base Fuel Ignition Delay Curve.	90
Figure 4.15 Isooctane and Isooctane + 1000 ppm Additive 2 Pressure vs. Time.....	91
Figure 4.16 Isooctane and isooctane + 1000 ppm Additive 2 Instantaneous Rate of Heat Release.	91
Figure 4.17 Isooctane and isooctane + 1000 ppm Additive 2 Low Temperature Heat Release...	92
Figure 4.18 Fractional Low Temperature Heat Release vs. Ignition Delay.	93
Figure 4.19 Fractional Low Temperature Heat Release vs. Delta Ignition Delay.....	94
Figure 7.1 Rapid Compression Machine Piston Head Assembly.	106
Figure 7.2 Rapid Compression Machine Piston Positions.....	109
Figure 8.1 General Assembly Drawing of Rapid Compression Machine.	110
Figure 8.2 Combustion Chamber.....	112
Figure 8.3 Left Combustion Cylinder Fixed End, right Combustion Cylinder Free End.....	113
Figure 8.4 Pistons in retracted position.....	114
Figure 8.5 Right and Left Piston Head Assemblies.....	115
Figure 8.6 Right and Left Cooling Collars with attached Hydraulic Fluid Collection Bottles. .	116
Figure 8.7 RCM Oil Chamber Drain Plug.....	117
Figure 8.8 Removing RCM Linear Transducer.	118
Figure 8.9 RCM with Air Chamber Removed and Hydraulic Fluid draining from External Oil Chamber into roasting pan.....	119
Figure 8.10 View of End of Drive Plunger, which must be manually pushed forward to release trapped hydraulic fluid.....	120
Figure 8.11 RCM with Drive Cylinder Removed and Secondary Hydraulic Line draining.	121
Figure 8.12 Using strap wrenches to unscrew Compression Plunger from Drive Plunger.	123
Figure 8.13 Rapid Compression Machine Main Hydraulic Line.....	124
Figure 8.14 External Oil Chamber supported by Ratchet Strap.	125
Figure 9.1 Combustion Chamber Seals.	127
Figure 9.2 Piston Seals.....	128
Figure 9.3 Wiper Seals.....	128

Figure 9.4 Neck Seals.	129
Figure 9.5 Internal Cooling Collar Seals.	129
Figure 9.6 External Cooling Collar Seals.	130
Figure 9.7 Forward Hydraulic Oil Chamber Seals.	130
Figure 9.8 Forward Taper Seals.....	131
Figure 9.9 Rear Taper Seals.....	131
Figure 9.10 Rear Hydraulic Oil Chamber Seals.	132
Figure 9.11 Rear Neck Seals.....	132
Figure 9.12 Drive Plunger Seals.	133
Figure 9.13 Air Chamber Seals.....	133
Figure 9.14 Combustion Chamber valve Tip.....	134
Figure 9.15 Linear Transducer Seals.	134

1 INTRODUCTION

1.1 Motivation

Today in the United States there are approximately 240 million on-road passenger vehicles that utilize an internal combustion engine for propulsion, with a further 16 million new vehicles replacing old vehicles or adding to total vehicle fleet each year [1]. Vehicles with an internal combustion engine that combust fossil fuels are still the most popular mode of transportation because of the convenience of fossil fuels. Fossil fuels convenience is due to their extremely high energy density and the vast distribution network developed over decades. On-road vehicles use approximately 57% of the United States total petroleum consumption, which is not projected to reduce in the coming decades [1]. Therefore since internal combustion engines are not disappearing anytime soon, efficiency increases must be pursued to preserve the modern lifestyle to which we have become accustomed.

The implementation of laser ignition and various fuel additives in practical combustion devices such as internal combustion engines have been shown to result in increased efficiency. Over the past two decades laser ignition has been investigated as a potential replacement for conventional spark ignition systems in order to improve combustion efficiencies in internal combustion engines [2] [3] [4] [5] [6] [7] [8] [9] [10]. However, very little of this fundamental laser ignition research has been conducted at elevated temperatures and pressures such as those seen at the end of a compression stroke in an internal combustion engine. Fuel additives also offer efficiency improvements by extending the lean limit and/or altering the knock tendencies of various fuels [11] [12] [13] [14] [15] [16]. Additives that extend the lean limit of a fuel increase efficiency by allowing the internal combustion engines to operate at the same Brake Mean

Effective Pressure (BMEP) but with a smaller amount of fuel. Additives that decrease knock tendencies increase efficiency by allowing internal combustion engines to operate at elevated compression ratios. The operation of internal combustion engines at elevated compression ratios increases engine efficiency since thermal efficiency increases with increasing compression ratio [17] [18].

1.2 Natural gas

Over the past three and a half decades the consumption of natural gas in the United States as an energy source has been steadily rising from 19.9 trillion cubic feet in 1980 to 26.7 trillion cubic feet in 2014 [19]. The increase in natural gas consumption in the United States can be attributed to the low price per unit of energy and low amount CO₂ generated during combustion when compared with other fossil fuels energy sources. Natural gas is used for a wide variety of purposes, which can be generalized into five categories: Transportation, Commercial, Residential, Industrial, and Energy. To distribute natural gas from the 514,786 wells [19] to the rest of the country, a vast nationwide natural gas gathering, transmission and distribution network has been constructed over the past nine decades. The transmission network is comprised of over 300,000 miles of pipeline linking together all 48 of the continental United States. To transport the natural gas through the thousands of miles of pipeline, approximately 1400 transmission compressor stations are positioned every 40 to 100 miles. As the natural gas is transported over considerable distances pipeline pressure steadily drops due to pipeline leaks and friction with the pipeline walls. To combat the unavoidable decrease in pressure inside the natural gas pipeline, compressor stations are strategically constructed along the pipeline to recompress the natural gas and propel it further along its journey [19]. In addition to the 1400 transmission compressor stations, the natural gas infrastructure also includes approximately 4600

gathering compressor stations and 600 processing plants, both of which also employ large reciprocating compressors and internal combustion engines [20].

Compressor stations are made up of only a few key components, the most important for the purposes of this study is the compressor unit responsible for increasing the pressure of the natural gas. The compressor unit is composed of a compressor and an internal combustion engine, gas turbine or electric motor that drives the compressor, also known as the prime mover. There are two different types of natural gas compressors used in modern compressor stations: centrifugal gas compressors and reciprocating gas compressors. Centrifugal gas compressors, essentially enclosed fans, increase gas pressure by increasing fluid velocity at a constant pressure, then as fluid velocity decreases the pressure increases due to Bernoulli's equation. Reciprocating gas compressors, also known as positive displacement compressors because they physically compress a fixed amount of gas very similarly to how an internal combustion engines compression stroke operates. Reciprocating natural gas compressors are generally used in conjunction with reciprocating internal combustion engines. Modern compressor stations have three different prime mover options: gas turbines, electric motors, or reciprocating engines. Of the three different commonly used prime movers, both gas turbines and reciprocating engines are fueled by a relatively small fraction of the pipeline gas. The most common compressor unit used in modern natural gas compressor stations is the reciprocating engine/reciprocating compressor setup due to easily being able to adjust flow rate of natural gas through the compressor station as demand increases and decreases [21].

Today in the United States alone there are approximately 1400 natural gas transmission compressor stations and 4600 gathering compressor stations that utilize one or more compressor units in continuous operation [21]. Since the vast majority of compressor stations are operated

using natural gas directly from the pipeline, a vast quantity of natural gas is consumed to simply transport natural gas to all the regions of the United States. Although it is debatable whether or not the world has reached peak oil yet due the resources made available with new extraction technologies, it is undebatable that the finite amount of fossil fuels on earth will not last forever. At the current rate of consumption is theorized that the earth's remaining fossil fuel reserves would potentially last only another 40 years [21]. Therefore any reductions in the amount of fossil fuel required to transport fossil fuel across the country could potentially have a significant impact in the long term. In order to prolong the world's limited supply of natural gas, efficiency improvements of reciprocating natural gas engines must be obtained. Currently the most promising ways to increase the efficiency of natural gas reciprocating engines are: natural gas additives, and laser ignition systems [21].

1.3 Previous Research on Natural Gas Additives

Over the past 30 years, research into fuel additives to improve the combustion of natural gas has been conducted throughout the world [11] [13] [14]. The majority of this natural gas additive research has focused on the addition of hydrogen to natural gas to increase thermal efficiency, decrease emissions, and extend the lean limit. From this extensive research it has been observed that by adding hydrogen to natural gas the brake thermal efficiency can be increased, the lean limit of natural gas can be extended, and emission such as unburned hydrocarbons, CO, and CO₂ and all are reduced [11] [13] [14]. Unfortunately, the addition of hydrogen to Natural Gas has also been shown to increase NO_x emissions, which is the combination of all NO and NO₂ emissions. However, NO_x emission can be significantly reduced either through the use of an after treatment systems or by operating at leaner conditions made possible by the lean limit extension that hydrogen provides.

Nagalingam et al. (1983) [13] investigated the effects of hydrogen supplementation in natural gas on engine performance and emissions in a single cylinder AVL research engine. Methane was used to simulate natural gas throughout the study, and four different fuel mixtures of methane and hydrogen were tested: 100% methane, 80% methane/20% hydrogen, 50% methane/50% hydrogen, and 100% hydrogen. The Indicated Mean Effective Pressure (IMEP) of the engine was measured from in-cylinder pressure measurements while operating the engine on each of the four different fuel mixtures. It was observed that as the percentage of hydrogen substitution increases, the IMEP decreased with a maximum decrease in IMEP of 23% when the engine was fueled with pure hydrogen. The decrease in IMEP when operating with pure hydrogen is due to hydrogen's low energy content per unit volume (because of its lower mass density), but this reduction can be counteracted by increasing engine size or boost pressure. However, when operated with pure hydrogen the research engine was able to reach substantially leaner conditions than when operated with methane alone. This characteristic makes it possible to change engine load without the use of a throttle valve, instead controlling power output by varying the equivalence ratio, thereby reducing pumping losses. Nagalingam et al. also investigated how varying the percentage of hydrogen substitution affected the production of nitric oxide (NO), hydrocarbon (HC), and carbon monoxide (CO) emissions. When operated with hydrogen, the NO emissions from the engine were higher than when operated purely with methane, which was attributed to the higher combustion temperatures. At an equivalence ratio of 0.83, the NO emissions were 750 ppm higher when operating with pure methane. However, HC and CO emissions were almost completely eliminated when the engine was operated with pure hydrogen. The few ppm of HC and CO emissions that were measured when running on hydrogen were thought to be due to combustion of lubricating oil. Finally, Nagalingam et al. investigated

the injection of water into the intake manifold to reduce NO emission when operating with pure hydrogen. It was observed that at higher engine speeds NO emissions reduced exponentially as the water injection flow rate increased [13].

Sierens et al. (2000) [14] studied the effects of various different methane and hydrogen fuel mixtures on the performance and emissions of a 7.4 liter V8 engine. Three different mixtures of methane and hydrogen that were used in the study were: 100% CH₄, 90% CH₄/10% H₂, and 80% CH₄/20% H₂. The efficiency of the engine was investigated for the three different fuel mixtures by varying air-fuel ratio and Brake Mean Effective Pressure (BMEP). It was observed that the maximum engine efficiency was achieved at an air-fuel ratio of between 1.1 and 1.2 for all three fuel mixtures and decreased as air-fuel ratio increased. The 10% addition of H₂ resulted in a measureable increase in efficiency in comparison to pure methane, but the addition of 20% H₂ did not significantly further increase the efficiency. It was also observed that the highest efficiency levels were achieved at the highest BMEP levels investigated and decreasing as BMEP levels were lowered. Sierens et al. (2000) also investigated the volumetric efficiency of the engine for all three fuel mixtures at varying equivalence ratios and noted that volumetric efficiency was nearly independent of fuel mixture while only slightly dependent on air-fuel ratio. Unburned hydrocarbon (UHC) emissions were found by Sierens et al. to be lowest at high load conditions with slightly lean fuel conditions, since the temperature of combustion is high and there is enough oxygen to fully react with the fuel. At near stoichiometric conditions there is negligible difference between the unburned hydrocarbon emissions of the three different fuel mixtures, but at lean conditions a reduction in UHC emissions was observed for the 80% CH₄/20% H₂ fuel mixture. However, the conditions that are optimal for producing low UHC are also those that are conducive for producing maximum NO_x emissions. To reduce NO_x emissions

the engine must be operated at lean fuel conditions, lower BMEP levels, and less H₂ addition percentages. Due to this observation Sierens et al. (2000) concluded that in order to maximize efficiency and minimize emissions the composition of the fuel is engine load dependent [14].

Akansu et al. (2004) [11] conducted a survey of research papers on the use of methane and hydrogen fuel mixtures in internal combustion engines. They found a consensus throughout the literature that when methane/hydrogen mixtures are compared against pure methane at the same operating conditions, brake thermal efficiency and NO_x emissions increase, while the lean limit, UHC, CO, and CO₂ emissions decrease [11].

Other than the potential for increase NO_x emissions under some operating conditions, the literature suggests that there are few downsides to using hydrogen as an additive for enhancing natural gas combustion (e.g. extending the lean limit) in natural gas compressor stations, until one looks at the economic and logistic viability of implementing a hydrogen additive system at natural gas compressor stations. The motivation for adding an additive such as hydrogen to methane is to allow for leaner operation of internal combustion engines, which results in higher efficiencies, decreased UHC emissions, and hopefully decreased NO_x emissions. To utilize the benefits of hydrogen addition to natural gas, approximately 20-30% by volume must be added. Supplying that volume of hydrogen to a natural gas compressor station would require the installation of either large compressed hydrogen tanks (along with the logistics required to transport the hydrogen to the facility) or a methane partial oxidation plant to be constructed in the vicinity of the compressor station, both costly solutions. Therefore, for economic reasons, hydrogen addition has not yet been implemented across the nation.

Given the potential for additives to enable natural gas engines to operate at leaner conditions, the sponsor of the research reported in this thesis was interested in evaluating liquid

additives that when combined in low concentrations with natural gas would provide similar effects as hydrogen but would be potentially more cost effective and logistically feasible to implement at natural gas compressor stations across the country.

1.4 Laser Ignition

In all practical modern SI engines, spark plugs play a crucial role in the conversion of chemical energy into useful work by supplying the initial energy required to overcome the activation energy of combustion initiation reactions. Before the invention of the spark plug, also known as Capacitive Discharge Ignition (CDI) systems, the few prototype internal combustion engines were ignited using a Hot Tube Igniter, Wire Spark Ignitor, or a Low Tension Igniter. However, none of these ignition methods proved reliable or safe enough for the internal combustion engine to progress past the initial prototype phase. The first spark plug is believed by historians to have been invented by Edward Berger on February 2, 1839 [22]. However, since Berger never patented this early spark plug it is difficult to credit the invention to Berger with complete certainty. What is known is that by the turn of the 20th century there existed multiple different patents for spark plug designs from such visionaries as Nikola Tesla and Robert Bosch, two men whose names figure prominently in the automotive industry even today. By the turn of the 20th century, several companies had been established specifically to produce spark plugs for the rapidly expanding internal combustion engine market such as Robert Bosch GmbH [23], Lodge Plugs Ltd. [24], and the Champion Ignition Company [25].

Although the spark plug has persisted as the source of ignition in SI internal combustion engines for over 170 years, the design is not without its drawbacks. The main drawbacks of the spark plug are that sparks can only be created in close proximity to the combustion chamber walls, the spark plug itself is a cold thermal mass inside the combustion chamber, additional

crevice volume is created around the spark plug, and routine maintenance is required to replace spark plugs as they wear out. Moreover, the higher compressed pressures that result from higher compression ratios in modern IC engines, require increased spark energies, which increases the rate of erosion of the spark plug electrodes and therefore the rate at which spark plugs need to be replaced. The maintenance costs associated with spark plug replacement is particularly problematic for large, industrial engines that operate continuously, such as natural gas compressor engines described above. Over the past two decades a solution to replace the time tested spark plug has been under development at universities and research labs across the world in the form of laser ignition.

There are four different types of laser ignition: thermal ignition, photochemical ignition, resonant breakdown, and nonresonant breakdown [8]. Each of the four different types of laser ignition offer different advantages and disadvantages that can make one type more advantageous for a specific application than another. Of the four different types of laser ignition, the only one not requiring a laser tuned to the wavelength of a target molecule is nonresonant breakdown. In this context the term breakdown refers to the formation of a plasma or spark by laser excitation.

Laser ignition by thermal ignition involves a laser beam being fired through a flammable gaseous mixture and raising the temperature of the gases along the laser path length high enough to cause thermal decomposition of the fuel. To increase the temperature of the gases along the path length of the laser, the wavelength of the laser must be very finely tuned to a vibrational or rotational mode of a target molecule, which would typically be a fuel molecule. During thermal ignition, breakdown of the gases into plasma does not occur. Due to heat transfer within the gas, thermal ignition is characterized by a long induction time, typically measured in milliseconds, when compared with other types of laser ignition [8].

Laser ignition by photochemical ignition is similar to thermal ignition in that it involves the use of a laser tuned to the wavelength of a specific target molecule. However, instead of increasing the temperature of gas by transferring energy into the rotation and vibration of the target molecule, the photons cause the target molecule to dissociate into highly reactive radicals. For photochemical ignition to successfully initiate the chain-branching reactions that lead to self-sustaining combustion, the rate of radical production due to the dissociation of target molecules must be greater than the recombination rate of radicals. Due to the physics that govern photochemical ignition, very little direct heating occurs and no breakdown of the gases takes place. When compared with thermal ignition, photochemical ignition exhibits shorter induction periods since the time required to form a radical pool is reduced. Also, since no gas heating occurs, heat transfer does not slow the induction time by transferring energy away from the ignition site. In general, the most effective wavelengths for photochemical ignition are those found in the UV range, since the energy of photons in the visible and IR ranges are smaller than the dissociation energy of most gases [8].

The final type of laser ignition that requires the use of a tuned laser is resonant breakdown. In resonant breakdown a nonresonant multiphoton photodissociation of target molecules is followed by a resonant photoionization of the newly formed molecules. The resonant photoionization of the gases causes breakdown to occur, which creates a high temperature and pressure kernel, on the order of 10^6 K and 10^3 atm. This high temperature and pressure kernel propagates outward in a rapidly expanding shock wave on a timescale much shorter than the timescale of the chemical kinetics of the fuel. In the region of the outward propagating shock wave, a radical pool develops, and it is this radical pool that leads to the eventual self-sustaining combustion of the gaseous mixture. Only two cases of resonant

breakdown have ever been demonstrated [8]. For resonant breakdown laser ignition, the wavelength of the laser required to initiate ignition is in the UV range.

Of the four different types of laser ignition, the only type that does not require a laser tuned to a specific wavelength is nonresonant breakdown. In this type of laser ignition, the laser beam is focused down to a point causing breakdown of the gas inside the combustion chamber. Since any wavelength laser can be employed for this type of laser ignition, this is the most prolifically researched type of laser ignition, including the research described in this thesis. The process of the formation of a plasma kernel in nonresonant breakdown is governed by two different mechanisms: multiphoton ionization and electron cascade, also sometime referred to as electron avalanche [4] [6] [8].

During multiphoton ionization, gas molecules are bombarded by photons. If a sufficient number of photons collide with the gas molecule to exceed its ionization potential the molecule becomes ionized and liberates one or more valence electrons. These liberated valence electrons now become free electrons floating throughout the gas until they either recombine with an ionized gas molecule or are hit by photons. If these free electrons are involved in a collision with a photon before recombining with a gas ion, their kinetic energy will be significantly increased. When these high kinetic energy free electrons collide with non-ionized gas molecules, the non-ionized gas molecules can then ionize, thereby liberating more free electrons eventually leading to breakdown of the gas. This process is known as electron cascade. For electron cascade to cause breakdown of gases, free electrons must be initially present. These initial free electrons can be supplied by multiphoton ionization, a process which on its own is unable to create breakdown of gases under most circumstances. In this way both multiphoton ionization and electron cascade are both responsible for nonresonant breakdown of gases.

In general, nonresonant breakdown is the most similar to ignition by traditional Capacitive Discharge Ignition (CDI) systems, of the four different types of type of laser ignition discussed above. However, significant differences between CDI and nonresonant breakdown laser ignition still exist including the power requirements and pressure dependence. Nonresonant breakdown typically requires high power fluxes on the order of 10^{10} W/cm² to cause breakdown, which is much higher than the theoretical minimum ignition energy of gaseous fuel/air mixtures. CDI systems have been shown to produce ignition with spark energies much closer to the theoretical minimum ignition energy. However, as pressure increases, the power requirements for nonresonant breakdown decrease while CDI power requirements increase. This pressure dependence makes nonresonant breakdown particularly well suited for high BMEP engines [8].

Phuoc and White (1999) [7] investigated nonresonant breakdown laser ignition of methane and air at 1 atm using a single-mode Q-Switched Nd:YAG laser operating at 1064 nm wavelength. They observed that as pressure was increased from 17 torr to 1010 torr the breakdown energy of the Nd:YAG laser decreased from 190 mJ to 15 mJ. The experimental setup that was employed for this study yielded a lean limit equivalence ratio of $\phi=0.61$ and a rich limit equivalence ratio of $\phi=1.95$. Equivalence ratio is defined as the ratio of the air-fuel ratio to the stoichiometric air-fuel ratio. They also investigated the minimum ignition energy (MIE) of methane/air mixtures ranging from $\phi=0.61$ to $\phi=1.95$, concluding that the minimum ignition energy of 3 mJ occur for mixtures between $\phi=1.058$ to $\phi=1.68$. Finally, it was also observed that the MIE increased at equivalence ratios near the lean and rich limits [7].

Bradley et al. (2004) [4] investigated nonresonant breakdown of isooctane and air mixtures using a Q-switched Nd:YAG laser operating at its fundamental wavelength along with a high speed He-Ne laser Schlieren imaging system. The gaseous isooctane/air mixtures were

contained in an optically accessible constant volume chamber capable of elevated pressures. Minimum breakdown energies at pressures ranging from 0.025 MPa to 1.5 MPa in air, and fuel conditions ranging lean isooctane to rich isooctane mixtures were investigated. It was observed that, as pressure increased, the minimum breakdown energy decreased, which was consistent to the results of Phuoc and White [7]. Similarly, it was observed that there was virtually no difference between the minimum breakdown energy for lean or rich isooctane mixtures. Bradley et al. also observed that at varying laser energies, varying probabilities of breakdown exist. A high speed He-Ne Schlieren imaging system was used to observe the initial spark kernel shock wave propagation and development. The imaging system was also used to observe flame speeds as the flame front propagated through the combustion chamber, noting that initial flame speeds exceeded the laminar flame speed of isooctane/air for approximately 1.5 ms. Finally the lean limit of ignitable mixtures was investigated at three different pressures yielding a lean limit equivalence ratio for isooctane/air of $\phi=0.62$. The lean limit measured by Bradley et al. was higher than the theoretical lower flammability limit of isooctane/air, leading to the conclusion that laser ignition is ineffective at fuel lean conditions [4].

Kopeck et al. (2005) [5] investigated laser ignition of methane/air mixtures at elevated temperatures and pressures inside a constant volume combustion chamber and a single cylinder of a large bore natural gas engine using a pulsed Nd:YAG laser. The effects of varying equivalence ratios on the minimum ignition energy were investigated in the constant volume combustion chamber at initial conditions of 30 bar and 200 °C. Minimum ignition energies of 4 mJ were observed for methane/air mixtures between $\phi=1$ to $\phi=0.056$, which then increased to 40 mJ for $\phi =0.45$ mixtures. The equivalence ratio of the leanest mixture capable of being ignited was found to be $\phi =0.45$. In the constant volume combustion chamber at 30 bar and 200 °C,

Kopeck et al. also investigated the relationship between ignition delay and equivalence ratio of the mixture. They observed that the shortest ignition delays occurred at equivalence ratio of 1, and then increased in duration as the mixture became leaner. Also, as the methane/air mixtures became leaner the peak pressure due to combustion inside the combustion chamber decreased until at $\lambda=2.2$ there is virtually no pressure rise. Inside the large born natural gas engine Kopeck et al. investigated how varying laser pulse energies affected the cylinder pressure, observing a direct relationship between the laser pulse energy and the peak cylinder pressure. Finally, Kopeck et al. investigated the relationship between the Mean Effective Pressure (MEP) of the engine and the required MIE, noting that, as the engine MEP increases, the required MIE decreases [5].

Beduneau et al. (2002) [3] investigated the MIE required to ignite laminar premixed methane/air mixtures using a Nd:YAG laser operating at 532 nm and compared the results to ignition using a conventional CDI system. A parametric study was conducted to characterize the effects of flow velocity, equivalence ratio, and focal length on the MIE. It was observed that as flow velocity increased, the MIE for rich mixtures increased but decreased for lean mixtures. The MIE increased for rich mixtures because convective heat losses also increased due to the increase in flow velocity, which required more energy to produce ignition. The decrease in MIE for lean mixtures was explained by the difference between a lean and rich mixture. The authors suggested that lean mixtures are difficult to ignite because of a scarcity of fuel molecules in the vicinity of the spark kernel. Therefore, as flow velocity increases more fuel molecules come in contact with the spark kernel decreasing the MIE of lean mixtures. Similar to many other laser ignition studies, Beduneau et al. reported that the lowest MIE occur when the fuel air mixture is near stoichiometric conditions. Finally, when the effect of focal length on MIE was investigated, it

was found that increasing the focal length increased the MIE for lean mixtures. Conversely, for rich mixtures, increasing the focal length decreased the MIE. This difference was explained to be a consequence of the difference in spark kernel size. In the lean case, the decrease in MIE with decreasing focal length was attributed to the fact that shorter focal lengths create smaller spark kernels. For a fixed quantity of energy, a smaller spark kernel will have a higher power density than a larger spark kernel, and high power density is required to ignite lean mixtures. In the rich case, the decrease in MIE with increasing focal length was attributed to the fact that the larger spark kernel created by the longer focal length comes in contact with more fuel molecules than a smaller spark kernel. At stoichiometric conditions, it was observed that an increase in the focal length always resulted in an increase in the MIE of the mixture [3].

Strozzi et al. (2014) [9] investigated the spark ignition of n-decane/air mixtures in a constant volume vessel at varying pressures and equivalence ratios, using a focused Nd:YAG laser operating at 1064 nm to cause nonresonant breakdown. Due to the stochastic nature of nonresonant breakdown, there exists a transition region as laser energy is increased between no breakdown and systematic breakdown. To characterize this phenomenon, Strozzi et al. first investigated spark formation in a nonreactive mixture of n-decane and nitrogen. It was found that, between 0 mJ and 31 mJ of incident laser pulse energy, no breakdown was observed. When the laser energy was increased to greater than 52 mJ, systematic breakdown occurred every time the laser was fired. However, in the region between 31 mJ and 52 mJ, it was observed that breakdown occurred stochastically with high normalized standard deviations of 50% or more. Next Strozzi et al. investigated the percentage of ignition events for n-decane/air mixtures at various equivalence ratios and laser pulse energies. Similar to many other nonresonant breakdown studies, it was observed that, as the equivalence ratio of the mixture increases or

decreases away from stoichiometric conditions, the required laser pulse energy to initiate combustion increases. Also, in the transition energy region, the variation in probability of ignition with laser pulse energy curves for each equivalence ratio can be accurately modeled by a logistic function. Finally, Strozzi et al. investigated the effect of pressure on the percentage of ignition at different laser pulse energies. They discovered that as pressure increased the energy required to achieve the same probability of ignition decreased linearly. However, they did observe that if this pressure/energy trend continued, negative energies would be required to initiate combustion at the high pressures experienced inside internal combustion engines. Therefore, a change of behavior is expected at higher pressures [9].

Bak et al. (2014) [2] investigated successive laser induced breakdowns in air and ethane/air mixtures by focusing a 532 nm wavelength Nd:YAG in a premixed ethane air flow. The time between the two laser pulses, along with the fuel air flow velocity and equivalence were varied to observe their effects on ignition. Time intervals between the two pulses ranging from as little as 10 ns to as large as 50 ms were investigated to determine the time period between the two pulses that resulted in the highest absorption of the second laser pulse. If the second pulse was fired between 10 ns and 30 ns after the first pulse, more than 80% of the second pulse was absorbed by the plasma created by the first pulse. Similarly, if the second pulse was fired approximately 1 ms after the first pulse, more the 60% of the pulse was absorbed into the propagating flame ignited by the first pulse. However, if the second pulse was fired between 200 ns and 100 μ s after the first pulse, virtually zero of the pulse energy was absorbed. This result was due to the fact that as the blast wave created by the first pulse propagates away from the focus region a low density region is left in its wake. This low density region is unable to absorb the energy of the second pulse because of a lack of gas molecules in the low density region.

Also, if the second pulse is fired more than 1 ms after the second pulse a very small percentage will be absorbed. This is due to the fact that, as the flame front propagates outwards from the ignition site, the density of the burned gasses are low, and therefore do not absorb much of the second laser pulse. When the effect of equivalence ratio on the absorption of the second laser pulse was investigated, it was observed that at both fuel lean and fuel rich conditions the recovery of the absorption of the second pulse increased at earlier times after the firing of the first pulse when compared with stoichiometric conditions. Finally, when the flow velocity of the fuel and air mixture was varied from 3.1 m/s to 6.1 m/s it was observed that the recovery of the absorption of second pulse increased with increasing flow velocity [2].

Weinrotter et al. (2004) [10] investigated multi-point laser ignition of lean methane/hydrogen/air mixtures in a constant volume vessel at elevated initial temperatures and pressures using an Nd:YAG laser operating at 1064 nm. First, the lean limit of pure methane/air mixtures was investigated using single point laser ignition to later compare to lean limit testing with hydrogen substitution. Tests indicated a lean limit of $\phi=0.53$ for pure methane/air mixtures. Since one of the major focuses of laser ignition work is to increase the lean limit of fuel/air mixtures, hydrogen substitution was investigated at three different equivalence ratios near the previously discovered lean limit. The combustion of methane/hydrogen/air mixtures at equivalence ratios of $\phi=0.56$, 0.53, 0.5 and hydrogen substitution percentages ranging from 0% to 50% was investigated. At $\phi =0.56$ complete combustion occurs without the addition of hydrogen. Because of this result, increasing the hydrogen substitution percentage dramatically increases the rate of combustion of the fuel/air mixture but only slightly increases the peak combustion pressure of the mixture. However, at $\phi =0.53$ the substitution of 15% hydrogen results in a combustion pressure increase of 12 times greater than the pure methane/air case. This

result is due to the incomplete combustion of methane as the lean limit for methane/air is approached. After 15% hydrogen substitution, the increase in peak combustion pressure slows dramatically similar to the $\phi = 0.56$ case and only the rate of combustion continues to dramatically increase. Finally, when $\phi = 2.0$ was investigated, it was observed that at 0% Hydrogen substitution the mixture would not ignite. Only with a 40% hydrogen substitution ratio was complete combustion of the fuel/air mixture able to be achieved. Finally multipoint ignition was compared to single point ignition to investigate if increased combustion rates could be achieved. In the case of two point ignition, an ignition source located at either side of the combustion chamber, resulted in a 50% increase in combustion rate and a 7% increase in peak combustion pressure. However, when three point ignition was investigated using a diffractive lens, all three spark kernels located on the same side of the combustion chamber, no significant difference was observed from single point ignition [10].

1.5 Gasoline

Over the past century, gasoline fueled internal combustion engines have become synonymous with personal transportation throughout the developed world. Gasoline is a mixture of thousands of different liquid hydrocarbon species that are distilled from crude oil. Depending on the source, gasoline can be composed of significantly different percentages of each species of hydrocarbon. Today, it is widely accepted that the peak in the conventional production of oil has already been reached and less than half the world's reserves for conventional oil production remain. To increase the efficiency and reduce greenhouse gas and pollutant emissions from the combustion of gasoline, different fuel additives have been investigated and implemented throughout the world over the past century [26]. However, due to the widely varying compositions of gasoline throughout the world, one fuel additive may have different effects on

gasolines of different compositions. Controversies still surround the performance of old and new additives because of the variable nature of gasoline composition. The most effective fuel additives that have been investigated to date have been oxygenated hydrocarbons, which have been shown to reduce the knock tendency and emissions from internal combustion engines fueled by gasoline at stoichiometric conditions [12] [15] [16]. The sponsor of this study, is interested in fuel additives to increase the anti-knock properties of gasoline which will enable internal combustion engines to operate at increased compression ratios, increasing engine efficiencies. However, due to the proprietary nature of gasoline fuel additives, little has been published on the topic and the sponsor has elected to not reveal the names of the gasoline additives tested in this study [16].

Geng et al. (2015) [12] investigated the effects on combustion performance and emissions in a direct injection gasoline engine by the fuel additive Methyl-cyclopentadienyl Manganese Tricarbonyl (MMT). Three different mixtures of ultra-low sulfur gasoline containing varying levels of MMT additive were compared to a base ultra-low sulfur gasoline in an inline four cylinder gasoline direct injection engine under stoichiometric conditions. At low and medium loads, the addition of increasing levels of MMT additive slightly increased the peak combustion pressure inside the cylinder but lengthened the ignition delay and combustion duration. At high loads the addition of MMT additive had no effect on peak combustion pressures, ignition delays, or combustion durations. However, at all three engine loads the addition of MMT did increase the rate of heat release inside the combustion chamber. In general, the addition of MMT fuel additive increased the CO, NO_x, and particulate matter (PM) emissions while significantly decreasing the unburned hydrocarbon emissions. The increase in CO emissions as MMT content increased was thought to be due to the increasing mass of fuel

inside the combustion chamber as MMT content is increased resulting in a lack of oxygen to fully oxidize the fuel. Under equal operating conditions the addition of MMT additive resulted in significantly increased PM emissions, both in terms of particle count and particle size. The significant increase in PM was a result of the formation of airborne manganese, branched chain hydrocarbons, alkenes, and aromatics during the combustion of MMT, which act as nucleation particles for PM to grow around. At high engine loads the PM emission increased by 880.8% with the addition of MMT [12].

De Silva et al. (2005) [16] investigated the changes in octane number of two chemically different gasoline formulations by the addition of oxygenated and non-oxygenated fuel additives. The oxygenated fuel additives that were tested in the different gasolines were ethanol, ethyl tert-butyl ether (ETBE), and methyl tert-butyl ether (MTBE) and the non-oxygenated fuel additives tested were isooctane and toluene. All of the additives were tested at 5, 10, 15, 20, and 25% by volume in both of the different base gasolines. All octane number testing was carried out in a Cooperative Fuels Research (CFR) engine according to the ASME standards for RON and MON testing. Base gasoline A was composed predominantly of isoparaffins and aromatic compounds with a RON of 98 and a MON of 90 and an average chemical formula C_8H_{15} . Base gasoline B was predominantly isoparaffins and naphthenes with a RON of 82 and a MON of 80 and an average chemical composition of C_7H_{14} . When the various fuel additives were added to the base gasolines it was observed that all of the additives increased the RON and MON, but the oxygenated additives had a significantly more pronounced effect. When the research octane number was investigated, ethanol was the most effective additive at increasing the octane numbers of gasoline A and B by 6% and 21% respectively when 25% by volume was blended with the base gasolines. However, the non-oxygenated additive isooctane had very little to no

effect on the RON number of either of the base gasolines, due to isooctane having the lowest octane rating of all the additives. When the effect on MON was investigated for each of the additives, it was discovered that the oxygenated additives were the most effective in increasing the MON. Under MON testing, the performance of all of the oxygenated additives was virtually identical and the performance of all the non-oxygenated additives was almost identical [16].

Weber de Menezes et al. (2005) [15] investigated the effect of using an azeotropic mixture of ETBE/ethanol as a possible fuel additive to improve gasoline to eurosuper standards. Eurosuper gasoline has a RON value of 95 and a MON value between 85 and 86. During the distillation of ETBE, an azeotropic mixture is formed with ethanol which cannot be separated by distillation. Therefore, if the azeotropic mixture of ETBE/ethanol is an effective gasoline fuel additive, the costs of separating ETBE and ethanol can be avoided. Pure ETBE and ethanol were also investigated to provide comparison to the ETBE/ethanol mixture. Two chemically different base gasolines were used: G1 had a high content of aromatic hydrocarbons, and G2 had a high content of isoparaffinic hydrocarbons. To characterize the performance of the different fuel additives, the RON and MON were investigated. In general, RON increased as additive content in the base gasoline increased for all three different additives. In G1 there was no significant difference between the effects of any of the additives. However, ethanol was measurably more effective at increasing the RON of G2 compared to the other two additives. When MON was investigated, it was observed that all three additives increased the MON in the same manner and there was no significant difference between their performances. These results show that the azeotropic mixture of ETBE/ethanol performs well as a gasoline additive for increasing octane number, especially in gasolines with high contents of aromatic hydrocarbons [15].

1.6 Thesis Overview

This thesis presents the results of natural gas fuel additive and gasoline fuel additive studies that were conducted as part of a sponsored project. The effect of fuel additives on natural gas and gasoline spark ignited engines were investigated using laser ignition and compression ignition experiments performed in a rapid compression machine (RCM). The goal of the laser ignition study was to examine the effect of additives to extend the lean limit of natural gas engines, while the goal of the compression ignition experiments were to examine the ability of fuel additives to decrease knock propensity of gasoline fuels. Three different natural gas fuel additives and two different gasoline fuel additives were investigated over the course of the study.

Chapter 2 discusses in detail the various instrumentation and analysis tools used to perform the different tests that comprise the two fuel additive studies. Special attention is paid to the operation and maintenance of the Colorado State University Rapid Compression Machine (RCM) in the hopes that this thesis will serve as the definitive reference for future generations of CSU RCM stewards. In addition to the overall description of the RCM in Chapter 2, the appendix of this thesis includes detailed information on disassembly and maintenance of the RCM.

Chapter 3 describes in detail the study of laser ignition of methane/air mixtures at elevated temperatures and pressures. First, results of the Minimum Ignition Energy (MIE) and Lean Limit testing of pure methane/air mixtures are presented. After concluding the baseline testing of pure methane/air mixtures, MIE and Lean Limit testing of the three natural gas fuel additives is extensively detailed.

Chapter 4 focuses on the auto-ignition of gasoline fuel additives at elevated temperatures and pressures. Ignition delay period as a function of compressed temperature for

isooctane/O₂/inert mixtures has become the standard against which the performance of different RCM facilities are benchmarked [27]. Extensive ignition delay testing of isooctane/air mixtures in the RCM along with ignition delay modeling were conducted as part of this study thereby establishing a baseline ignition delay curve for comparison to the additive results. These results were then compared to results published in the literature to benchmark the performance of the CSU RCM. In addition to using isooctane as a baseline fuel for the gasoline fuel additive testing, a Toluene Reference Fuel (TRF) blend was also modeled using CHEMKIN and tested in the RCM to establish a second baseline ignition delay curve for comparison to additive results. Finally, the ignition delay results of the two different gasoline fuel additives are presented.

In Chapter 5 the conclusions from the two different fuel additive studies are presented along with recommendations for further work that will advance the fields of combustion research and laser ignition.

2 EXPERIMENTAL SETUP

All of the experimental testing for this study has been conducted at the Colorado State University (CSU) Engines and Energy Conversion Laboratory (EECL) and Center for Laser Sensing and Diagnostics (CLSD). The EECL was founded in 1992 in an abandoned power plant and has since grown into a globally recognized energy research facility. The CLSD was moved to the Powerhouse Energy Campus in the spring of 2014 when Dr. Azer Yalin and Dr. Anthony Marchese moved into a shared lab.

2.1 Rapid Compression Machine

The CSU Rapid Compression Machine (RCM) served as the main test bed for all of the testing described in this thesis. An RCM is a machined designed to replicate the thermodynamic conditions (e.g. pressure and temperature) inside the cylinder of an internal combustion engine during the compression stroke, but more repeatedly than in an actual engine. The CSU RCM was built by Marine Technologies Ltd. in Galway Ireland, and was delivered to CSU in the summer of 2012. The RCM is a modernized adaptation the original Shell/National University of Ireland Galway RCM. The original Shell/NUIG RCM was designed and constructed in the 1960's by Shell UK Ltd., and is still in use today [28].

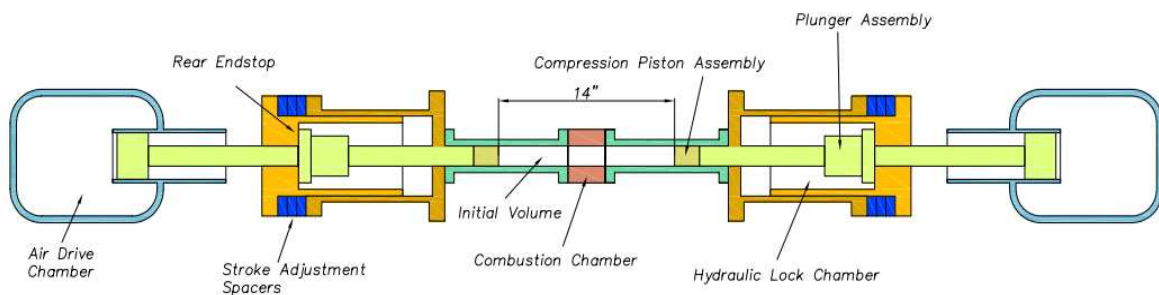


Figure 2.1 Schematic Diagram of Colorado State University Rapid Compression Machine (RCM).



Figure 2.2 Colorado State University Rapid Compression Machine.

The CSU RCM is a dual opposed piston design allowing for the nearly adiabatic and homogeneous compression of gaseous mixtures in approximately 10 ms as shown schematically in Figure 2.1. A photograph of the CSU RCM is included in Fig. 2.2. The compression ratio of the RCM can be varied by use of different piston geometry, but for all the experiments carried out for this study the compression ratio was held constant at 11.6:1. Traditionally, RCMs have been used for chemical kinetics studies of various fuels that auto-ignite due to the elevated temperature and pressures inside the RCM combustion chamber at the end of compression.

In typical RCM auto-ignition experiments, initial conditions are selected such that the fuel-oxidizer mixture auto-ignites within 5 to 200 ms after the end of compression, thus allowing

the ignition delay period to be measured from the pressure vs. time traces. During the ignition delay period, which is the time period from the end of compression to the start of ignition, the temperature and pressure of the mixture decreases due to heat transfer to the combustion chamber walls. As a result, if the ignition delay period is too long, the temperature will decrease to a sufficiently low temperature such that the mixture will never ignite. For this study, two different types of fuel and oxidizer mixtures were studied in the RCM: auto-reactive and spark-reactive mixtures. For the purposes of this study, auto-reactive mixtures were defined as gaseous mixtures of fuel and oxidizer that auto-ignite solely due to the elevated temperatures and pressures the RCM creates in the combustion chamber at the end of the compression cycle. Spark-reactive mixtures were defined as fuel and oxidizer mixtures that do not auto-ignite solely due to the elevated temperatures and pressures created in the combustion chamber at the end of the compression cycle. To ignite the spark-reactive mixtures, an external energy source such as a laser spark is required to initiate combustion within the combustion chamber. For this study, a laser ignition setup was designed to generate sparks inside the combustion chamber of the RCM. The spark-reactive fuel air mixtures were used when studying laser ignition to insure that ignition events were the result of a laser generated spark and not auto-ignition.

The post compression temperature of the fuel/air mixture is determined by the thermodynamic properties of the gaseous mixture (air/fuel ratio, fuel type, diluents) and the initial temperature and pressure. Compressed pressure and temperature (P_{comp} , T_{comp}) are found from the initial pressure and temperature (P_0 , T_0), i.e. those before compression, by modeling adiabatic compression using the Gaseq program [29]. Gaseq relates the pressures and temperatures using Eq. 1:

$$\ln \frac{P_{comp}}{P_0} = \int_{T_0}^{T_{comp}} \frac{\gamma}{\gamma-1} \frac{dT}{T} \quad (1)$$

Gamma (γ) is the specific heat ratio (taken here as a function of the bulk gas temperature based on the gas mixture). This approach neglects heat transfer from the gas mixture to the combustion chamber walls; however, past research has shown that, for most RCM investigations, these effects can be treated by use of the so-called “adiabatic core region”, wherein the main core of the gas can be considered to compress isentropically [30] [31] [32].

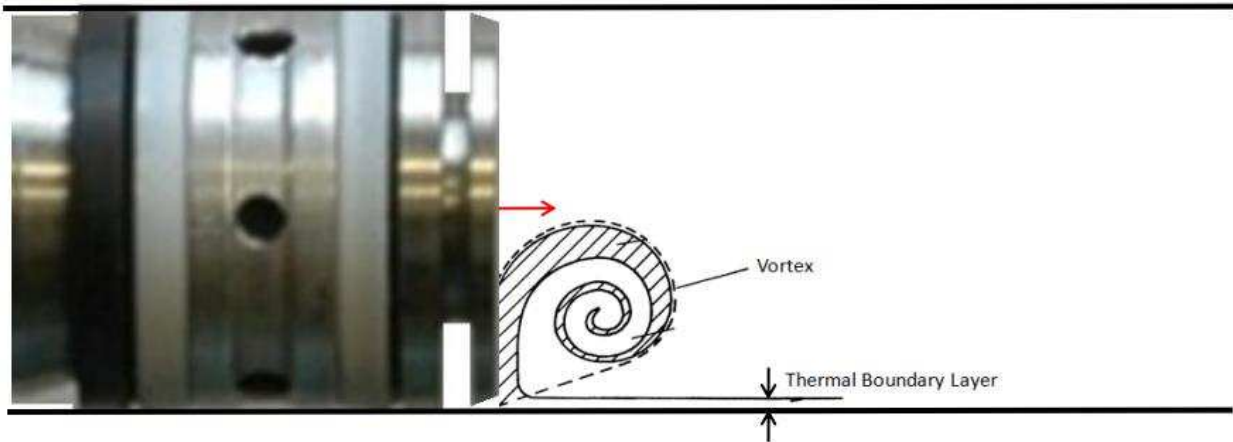


Figure 2.3 RCM Creviced Piston.

The fluid dynamics within the combustion chamber present another source of temperature variation in the compressed gas mixture. A feature of the CSU RCM that serves to greatly reduce the temperature variation in the adiabatic core region is the creviced pistons (see Figure 2.3) [33], which minimize the formation of roll-up vortices that would otherwise force the cool boundary layer gases to mix with the hot core [34]. The creviced piston design also helps maintain the homogenous temperature profile across the core region that is required for the adiabatic core hypothesis to remain valid. Mittal and Sung [35] used acetone planar laser-induced fluorescence (PLIF) to measure temperature across the core region of both flat-topped and creviced pistons and were able to confirm the adiabatic core region assumption. The design of the CSU RCM is especially favorable for studying laser ignition due to the lack of velocity

fields in the center of the chamber, helping to ensure that the laser spark kernel remains free from flow disturbances.

Appendix A presents instructions for operating the RCM, including procedures for turning on the RCM and firing the RCM. Appendix B discusses the step necessary for maintaining the RCM, including step by step instructions to disassemble the RCM's center section and end sections. Appendix C provides details on each of the RCM's seals. Appendix D bestows solutions to common RCM issues. Finally, Appendix E presents an uncertainty propagation for the temperature inside the RCM combustion chamber at the end of compression.

2.2 Fuel Blending System

The RCM is designed to adiabatically compress fuel and oxidizer mixtures extremely rapidly and repeatedly to replicate the pressure and temperature conditions inside an internal combustion engine at the end of the compression stroke. However, unlike an internal combustion engine the RCM does not have an internally integrated fuel and oxidizer blending system. Therefore, to accurately and precisely blend fuel and oxidizer mixtures for testing in the RCM, a fuel blending system was designed and constructed to be used in conjunction with the RCM. Figure 2.4 displays a schematic drawing of the fuel blending system.

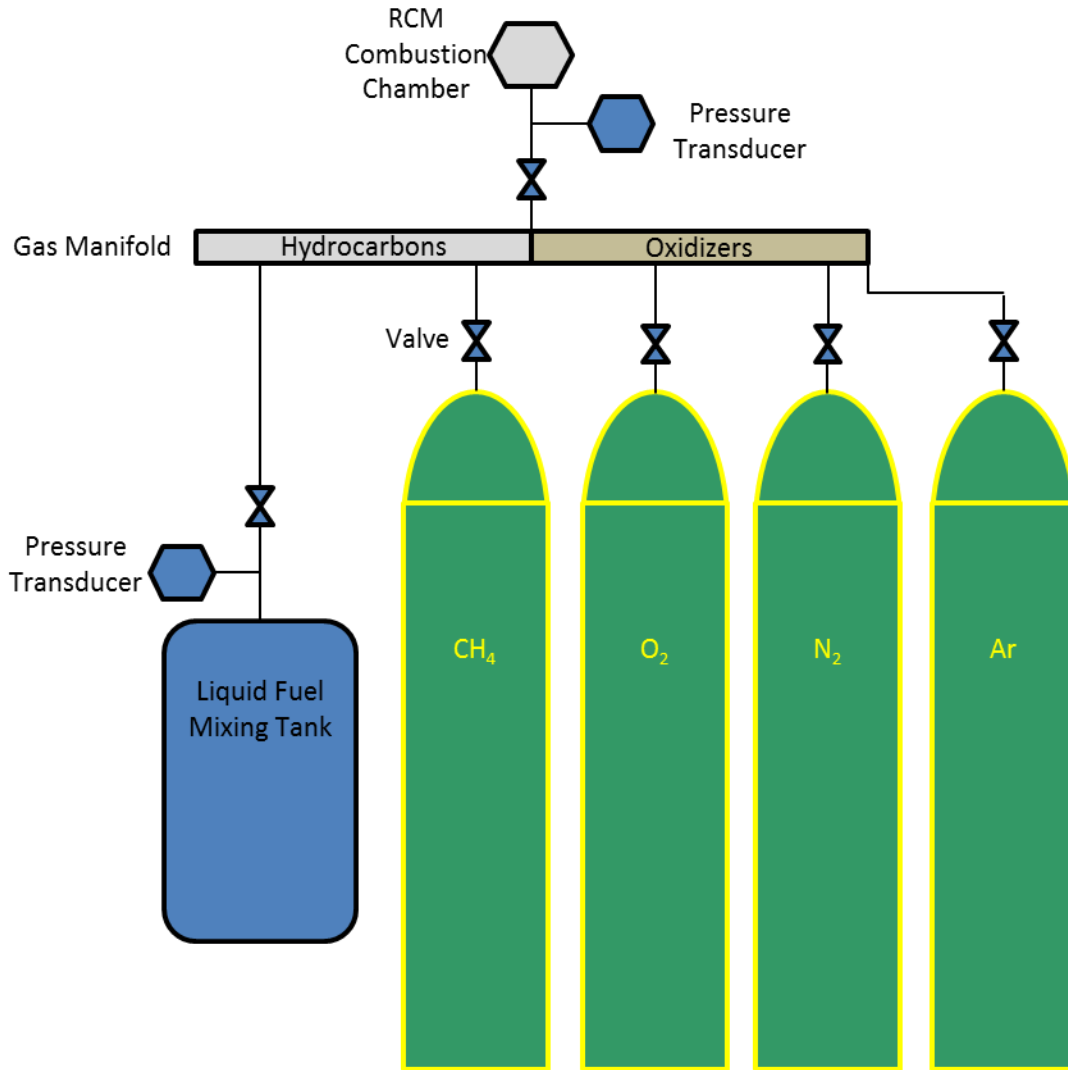


Figure 2.4 RCM Fuel Blending System.

The fuel blending system uses Dalton's Law of Partial Pressures to specify the mole fraction of each individual species in the fuel and oxidizer mixture. Dalton's Law of Partial Pressure states that the total pressure of a mixture of ideal gases in a closed volume is the sum of the partial pressures of the individual species. The partial pressure of a species is the pressure that individual species would exert if it was the only species in the closed volume.

$$P_{Total} = P_1 + P_2 + P_3 + \dots \quad (2)$$

$$P_i = \frac{(n_i RT)}{V} \quad (3)$$

P_{total} is the total pressure, P_i is the partial pressure of the i^{th} species, n_i the number of moles of the i^{th} species, R the universal gas constant, T the temperature and V the volume of the system.

Dalton's Law of Partial Pressure allows the pressure of a mixture to be related to the number of moles of each of the individual species in the mixture. Therefore the partial pressure of each individual gas species can be expressed in terms of the mole fraction of each species.

$$X_i = \frac{n_i}{n_{total}} \quad (4)$$

$$P_i = X_i P_{total} \quad (5)$$

X_i is the mole fraction of i^{th} species and P_i the partial pressure of i^{th} species. The fuel blending system is comprised of five main components: pressure sensors, liquid fuel mixing tanks, gas bottles, gas bottle manifold, and temperature control system. Together these components allow gaseous and liquid fuels to be accurately mixed with oxidizers and injected into the combustion chamber of the RCM.

2.2.1 Pressure Sensors

The fuel blending system utilizes two different types of pressure sensors: gas line pressure gages, and mixing tank pressure transducers. The absolute pressure in the combustion chamber is measured during filling and evacuating by two different independent pressure transducers, an Omegadyne DPG409 [36] and a MKS Baratron 722B [37]. It is vital that the pressure in the combustion chamber is known, since the ratio of each constituent species in the fuel and oxidizer is specified according to their individual partial pressures (in accordance with equations 2 to 5 above). Two independent pressure transducers are used to measure the pressure in the combustion chamber because the MKS transducer only has a range of 0-1000 mbar but in some specific tests the combustion chamber is required to be filled to pressures greater than 1000

mbar. Therefore, the Omegadyne pressure transducer was added later to allow for tests to be conducted that require initial pressures higher than 1000 mbar.

Each of the banks of the gas bottle manifold has a Span Compound Pressure Gauge with a range of 1 bar vacuum to 28 bar. The gas bottle manifold pressure gauges serve two different purposes. First, the manifold pressure gauges indicate whether the manifold is under pressure or vacuum when switching between gases or filling the combustion chamber. Second, the manifold pressure gauges allow the operator to insure that the gas bottle manifold is fully sealed and not leaking gas to the atmosphere.

The final pressure sensor in the fuel blending system is an Omegadyne DPG409 connected to the liquid fuel mixing tanks. These digital pressure gauges serve three purposes. First, they allow the operator to confirm the liquid fuel mixing chambers have been evacuated to very low pressures before filling. Second, they allow for the accurate filling of the liquid fuel mixing chambers using the partial pressure method. Third, they allow the operator to determine if the mixing chamber is leaking or holding pressure.

2.2.2 Liquid Fuel Mixing Tanks

The fuel blending system has two identical liquid fuel mixing tanks that are connected by ¼” stainless steel Swagelok tubes to the hydrocarbon bank of the gas bottle manifold. The liquid fuel mixing tanks allow hydrocarbon fuels that are liquid at standard temperatures and pressures to be vaporized and then tested in the RCM. The liquid fuel mixing tanks were designed and implemented by Marc Baumgardner, emulating the mixing tank design utilized with the RCM at the National University of Ireland Galway. To fill the liquid fuel mixing tanks, the mixing tanks are evacuated down to a sufficiently low pressure as indicated by a reading of 0 mbar on the Omegadyne DPG409 pressure gauge. Next, a liquid hydrocarbon fuel is injected into the mixing

chamber through a gas tight septum injection port. When the liquid fuel is injected into the low pressure mixing tank the fuel undergoes a phase shift from the liquid to gas phase. Next, the pressure gauge and the gas bottle manifold are used in conjunction to fill the mixing chamber with oxidizer and diluent gases, once again using the partial pressure method. Finally, the mixing tank magnetic stirrer is turned on and the mixing tank is left for two hours to insure that the gas mixture inside is sufficiently well mixed so that it can be considered a homogenous mixture.

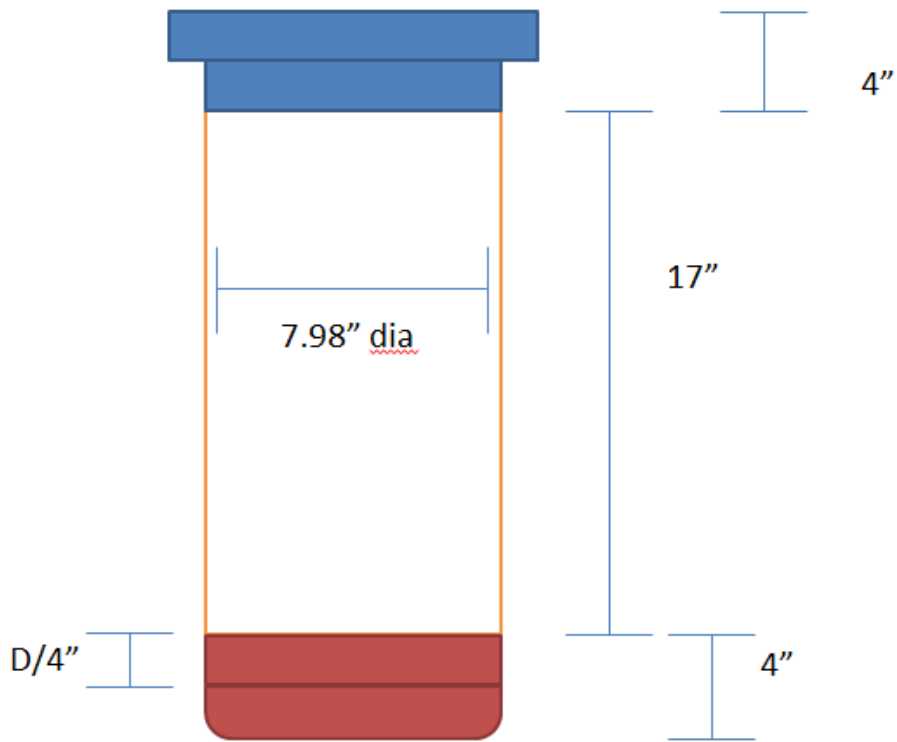


Figure 2.5 Schematic Drawing of Liquid Fuel Mixing Tank.

Table 2.1 Liquid Fuel Mixing Tank Dimensions.

Mixing Tank Diameter [D]	20.27 cm
Mixing Tank Height*	57.61 cm
Depth Below Cylinder [a]	5.07 cm

Volume of Cylindrical Section	18.59 L
Volume of Ellipsoidal Bottom	0.64 L
Total Volume of Liquid Fuel Mixing Tank	19.23 L

*Not including dished end

2.2.3 Gas Bottles

The compressed gas bottles are critical components of the fuel blending system. The fuel blending system was designed to accept high pressure gas cylinders as large as a size 50, which have a height of 63 inches and an internal water volume of 50 liters [38], but can accept smaller size high pressure gas cylinders as well. To reduce output pressure from the high pressure gas bottles to a useable pressure that can be used to fill the RCM, Airgas model Y11-N245B regulators are attached to each gas bottle. The regulators accept a maximum input pressure of 3500 psi and have a maximum output pressure of 50 psig. The regulators are connected to the gas manifold by semi-rigid ¼” nylon tubing with a maximum pressure of 800 psig.

2.2.4 Gas Manifold

The fuel blending system includes a gas manifold allowing for multiple different compressed gas bottles to be integrated into the system in addition to connecting the liquid fuel mixing tank to the RCM. There are two separate banks of the gas manifold. The left bank is where all oxidizer and diluent gases are connected to the system and the right bank of the manifold is where all hydrocarbon fuels are connected to the system. The reason the gas manifold has two separate banks is to prevent uncontrolled reactions between fuels and oxidizers. There is a possibility that a small amount of gas could adhere to the inside of tubing or valves that comprise the gas manifold after evacuation and react in an uncontrolled manor with another gas at a later time. By creating two independent banks the risk of uncontrolled reactions

is significantly reduced. The left bank of the gas manifold has three ports to which high pressure oxidizer and diluent gas bottles are connected. The right bank of the gas manifold has five ports to connect high pressure hydrocarbon gas bottles and one port that connects to the liquid fuel mixing tanks.

2.2.5 Temperature Control System

The entire fuel blending system is temperature controlled to prevent liquid fuel condensation inside the tubing between the liquid fuel mixing tanks and the combustion chamber. Swagelok stainless steel tubing is wrapped in Omegalux heat cable model DHT05 1060LD, and controlled by Versatile Control Temperature Control Devices model JDL612. The heating system has a maximum temperature of 1400° F, but typically the system is only used to heat the fuel blending system to 100° C or less. Finally, the entire fuel blending system has been wrapped in fiberglass exhaust manifold wrap to reduce the temperature fluctuations of the fuel blending system and reduce the load on the heating system.

2.3 Laser ignition Setup

A major component of the research conducted for this study was centered on fundamental studies of laser ignition at elevated temperatures and pressures such as those experienced at the end of a compression cycle inside an internal combustion engine. To replicate the high temperature and pressure conditions, the CSU RCM was selected as the test bed for laser ignition testing due to ability to repeatedly adiabatically compress gas mixtures. Although the CSU RCM was originally designed for auto-ignition chemical kinetics studies, it was adapted to be used for the laser ignition. For the laser ignition tests, fuel and oxidizer mixtures that did not auto-ignite under the RCM's high temperature and pressure conditions were employed (the so called spark-reactive mixtures defined above). These types of fuel and oxidizer mixtures were employed for

laser ignition tests because it ensured that ignition was a result of an external ignition source, which in the case of this study is a laser ignition setup. The laser ignition setup is composed of three different components: the laser, the optical plug, and the steering and measuring optics as shown in Figure 2.6. The laser delivery setup was designed and implemented with support from members of Professor Yalin's research group, in particular Ciprian Dumitrache.

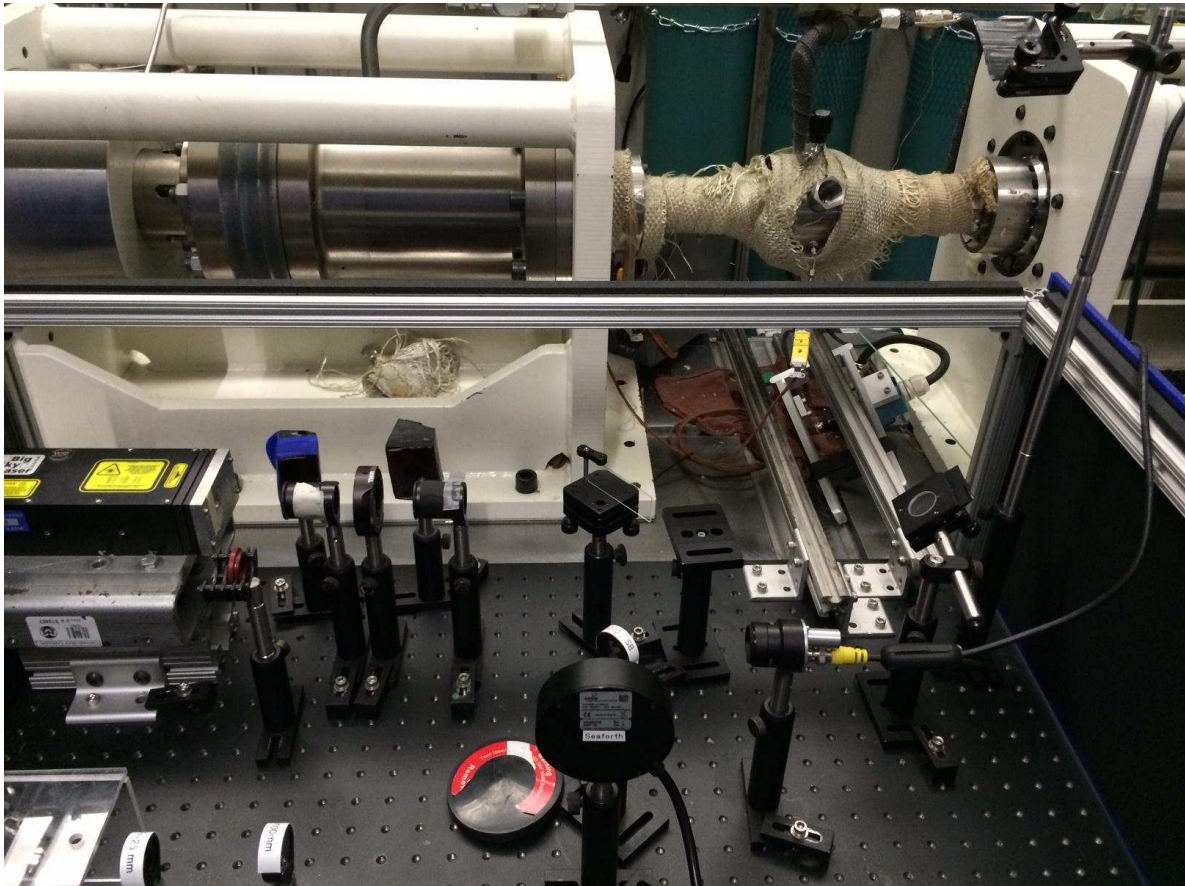


Figure 2.6 Laser Ignition Setup positioned next to RCM.

2.3.1 Laser

The laser source used during all laser ignition experiments was a Big Sky Ultra Nd:YAG compact laser operating at its fundamental wavelength of 1064 nm, with a pulse duration of 12 ns, and beam quality of $M^2=1.9$.

2.3.2 Optical plug

The laser beam was delivered to the combustion chamber of the RCM using the optical plug shown in Figure 2.6. The optical plug was designed to tightly focus the laser beam inside the RCM combustion chamber and prevent the high pressure gases from escaping out of the combustion chamber. Beam focusing is achieved by an interchangeable plano-convex lens with a focal length ranging from 10 to 25 mm. By using different focal length lenses the location of the spark inside the combustion chamber can be varied. High pressure gasses are sealed inside the combustion chamber by a 3 mm thick sapphire window held between two copper gaskets. Sapphire was chosen due to its high strength and good transmission of 1064 nm light. Figure 2.7 shows how the optical plug mates with the combustion chamber. Schlieren imaging ports are also shown.

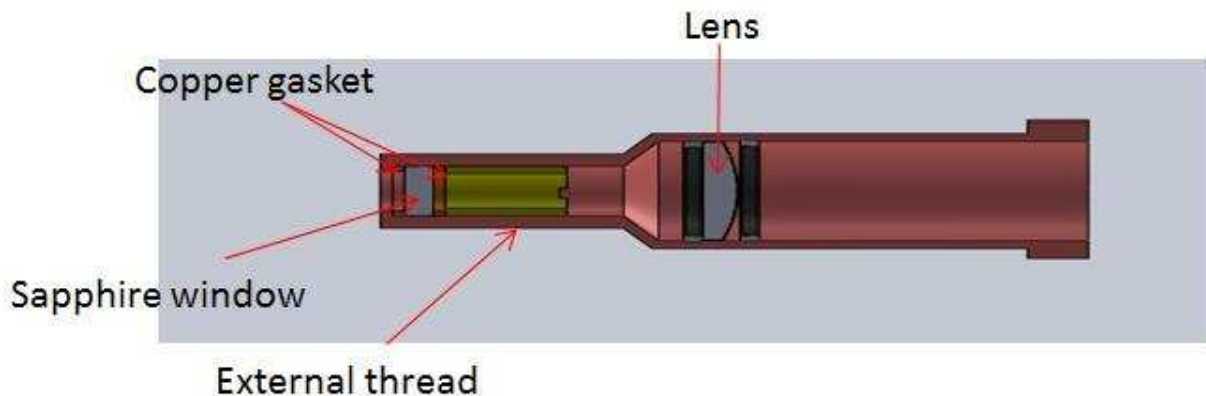


Figure 2.7 Optical plug for focusing the laser beam inside the combustion chamber.

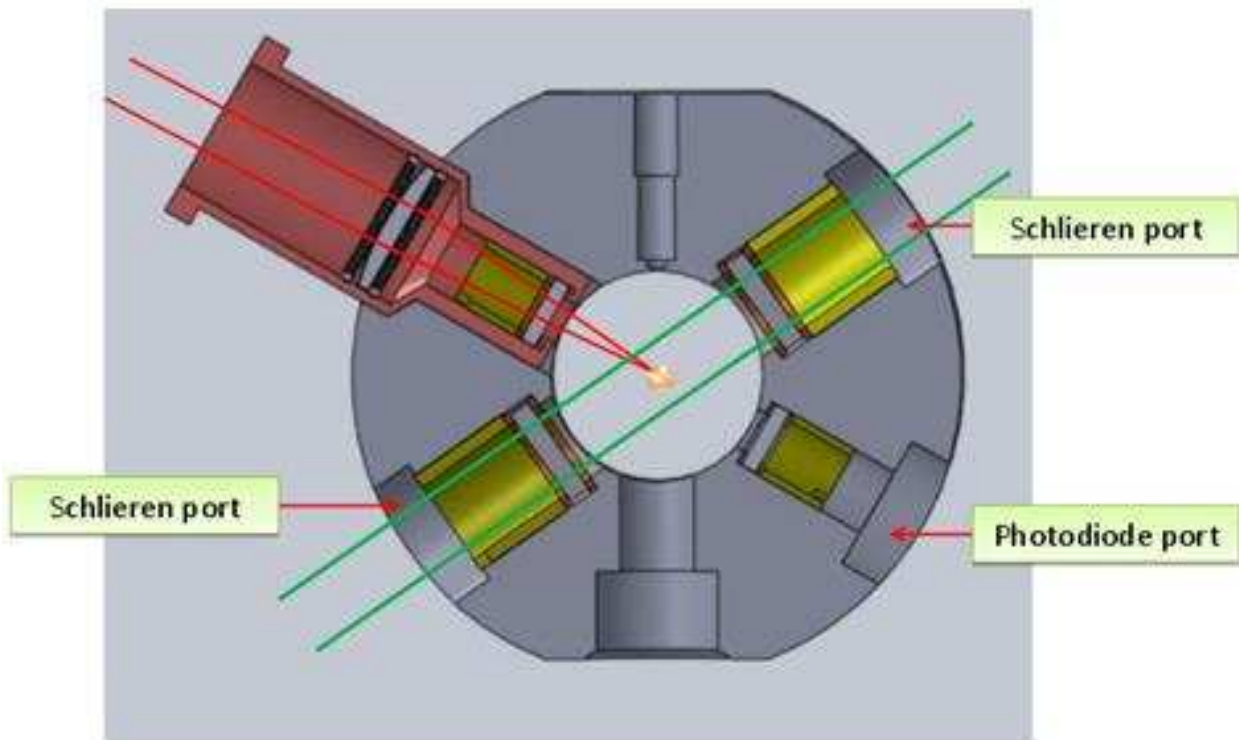


Figure 2.8 Schematic of optical ports and combustion chamber.

2.3.3 Steering and Measuring Optics

After the laser beam exits the laser head, the beam travels through a series of steering and measuring optics. The optical layout is shown in detail in Figure 2.8. The beam leaves the laser head and first passes through a polarizer that establishes a p-polarization. Next, the beam is passed through a half-waveplate and then through a second polarizer. By rotating the half-waveplate, while keeping the position of the polarizers constant, the amount of laser energy delivered to the combustion chamber can be varied from zero to 100%. A beam splitter is employed next to allow a small fraction of the laser beam (~3%) to reach the energy meter and the photodiode. The energy meter enables the measuring of individual laser pulse energies delivered to the combustion chamber, while the photodiode provides an accurate timing of the laser firing. The remainder of the beam (~97%) is transmitted through the beam splitter and is

steered using two mirrors through the optical plug into the combustion chamber. The beam is focused by a plano-convex lens that is located inside the optical plug. Spark formation occurs at the focus of this lens. A second photodiode is mounted at the exit optical port of the combustion chamber, 180° opposed to the incoming laser beam, to detect the formation of a spark. To ensure that only spark luminosity is measured (not the laser beam itself) a lens is used to image the spark on the photodiode through a 1064 nm blocking filter. A pulse-delay generator is used to synchronize laser firing with the RCM firing.

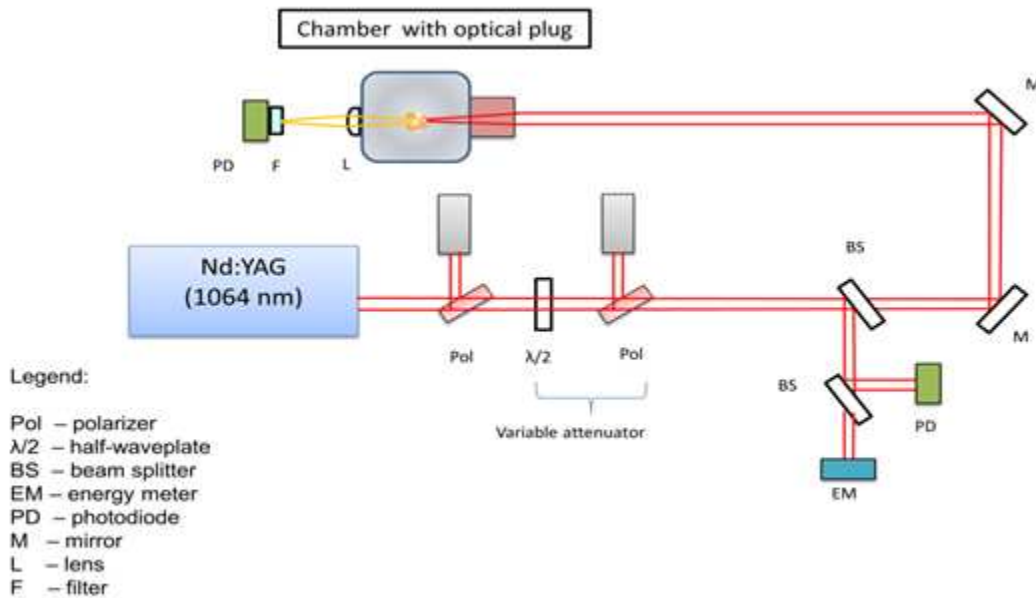


Figure 2.9 Experimental setup for RCM Laser Ignition System.

2.4 High Speed Schlieren Imaging System

The main output data from all the auto-ignition and spark ignition tests in the RCM for this study are pressure versus time traces. These traces are used to determine the ignition delay, to calculate the bulk mean temperature of the gaseous mixture in the combustion chamber and to calculate the apparent rate of heat release from reacting fuel/oxidizer mixtures. However, since

the pressure inside the combustion chamber is measured at the wall of the combustion chamber only the bulk or average pressure inside the combustion chamber is known. Since only the bulk pressure is known, a high speed Schlieren imaging setup was developed to image the evolution of the plasma kernel and flame propagation during laser ignition events. Schlieren imaging allows visualization of flow-field density variations due to the associated variations of the index-of-refraction, and when recorded using a high speed camera can provide temporally and spatially resolved images. A high speed Schlieren imaging setup, using an ultra-bright LED as the light source, has been developed to interface with the RCM's combustion chamber and is shown in Figure 2.9. The high speed Schlieren imaging setup was developed in collaboration with Ciprian Dumitrache and Marc Baumgardner. The beam from the LED passes through a slit that spatially filters the light and is subsequently collimated and steered through the combustion chamber with a pair of mirrors. After leaving the combustion chamber, the light is focused on a knife-edge that partially blocks the beam path, allowing only those photons bent by changes in index of refraction to pass. The light that passes the knife-edge is collected using a high speed CMOS camera (PCO 1200).

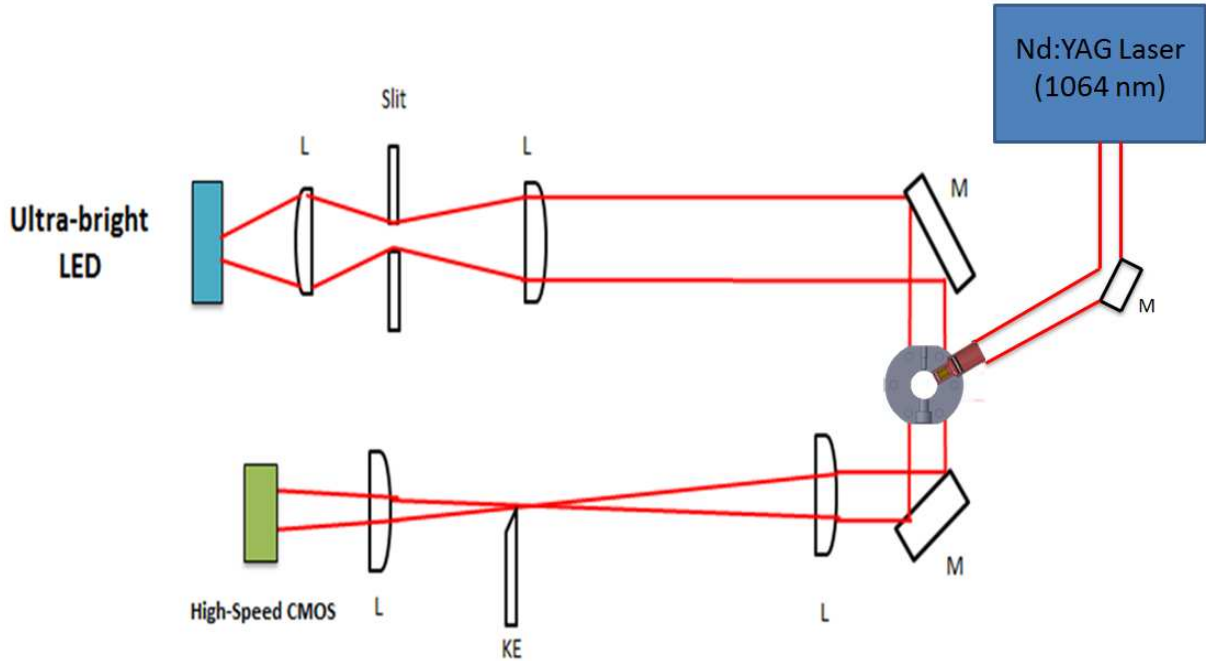


Figure 2.10 Schematic of the bench-top setup for Schlieren Imaging.

2.5 Data Analysis

The main data acquired during the experiments performed for this study are pressure versus time traces. For any meaningful conclusions to be drawn, these traces must be individually analyzed to extract the details about the combustion process that occurs inside the RCM combustion chamber. Some details such as the ignition delay, compressed pressure, and peak combustion pressure can be directly extracted from the instantaneous pressure data by closely examining specific regions of the pressure curve. However, other details about the combustion events such as the apparent heat release rate, minimum ignition energy, and lean limit require additional data analysis. In each of these cases, computer codes were developed in MATLAB to analyze the data. MATLAB computer codes were developed in collaboration with Ciprian Dumitrache.

2.5.1 Minimum Spark Energy (MSE) and Minimum Ignition Energy (MIE)

When conducting laser ignition experiments, two of the most important metrics are the Minimum Spark Energy (MSE) and the Minimum Ignition Energy (MIE) for different fuel/oxidizer mixtures. The MSE is defined as the laser pulse energy required for creating a spark inside the RCM combustion chamber, while the MIE is defined as the minimum laser pulse energy required to ignite the mixture as indicated by the presence of a measureable pressure increase in the instantaneous pressure data. In general the MIE is higher than the MSE, but depending on the test conditions the MIE and MSE can be equal. MIE and MSE are important metrics when comparing laser ignition studies because they have direct bearing upon the specifications of the laser that can be used in the future for laser ignition applications. One of the major factors that currently limits the widespread utilization of laser ignition technology is the prohibitively high cost of lasers powerful enough to initiate combustion. Therefore the lower the MIE and MSE, the less powerful a laser that can be used for a laser ignition application, and in general the less powerful a laser the lower the cost of the laser.

To visually represent the MSE and MIE data, the single laser pulse energy is plotted versus the probability of spark formation/ ignition. However, due to the stochastic nature of laser ignition fuel/oxidizer, fuel/air mixtures do not instantly change from not igniting to igniting as the laser pulse energy increases, which would create a step function MIE or MSE graph. Instead, as the laser pulse energy increases from a non-igniting level to an igniting level, or non-sparking to sparking levels, the fuel/oxidizer mixture experiences a transition region where laser pulse energies exist that cause the fuel/oxidizer mixtures to ignite/spark only a percentage of the test runs. Due to this transition region the MIE and MSE curves were plotted using a logistic function:

$$P(E) = \frac{1}{1 + \exp\left(\frac{-(E - E_{50})}{\Delta E}\right)} \quad (6)$$

$P(E)$ is the probability of ignition/spark formation at a specific laser pulse energy E , E_{50} represents the laser energy that results in a 50% probability of ignition, and ΔE represents the energy width of the transition region. Also due to the stochastic nature of laser ignition there is an inherent level of error in the measured probability of ignition. To account for this inherent error the MSE and MIE are graphed with error bars and 95% confidence bounds. To calculate the error bar, σ , (uncertainty) for each different data point, the following equation, assuming a normal approximation to the binomial distribution, was used:

$$\sigma = \pm Z \sqrt{\frac{P(P-1)}{n}} \quad (7)$$

P is probability of ignition/spark formation, n is the number of tests, and $Z=1.96$ (based on 95% confidence). To calculate the confidence bounds the previously calculated errors were used to calculate corresponding weights for each data point using the equation:

$$W = \frac{1}{\sigma^2} \quad (8)$$

In the special cases where $P=1$ or 0 the nominal error of $\sigma=0.1$ was assigned to allow a weight of $W=0.01$ to be used for calculating the 95% confidence bounds. The special cases ($P=1$ or 0) nominal σ value was chosen specifically to represent the confidence with which the extreme values on the MIE and MSE graphs are known.

For this study, MIE curves were produced for a variety of different additives and compared to one another to determine if there exists a fuel additive that can improve the combustion characteristics of Methane and Natural Gas. The results from these studies are presented in Chapter 3.

2.5.2 Calculation of Apparent Rate of Heat Release

One of the most important parameters for understanding real world combustion events is the heat release rate and net heat release. In order to be able to quantify the heat release rate and the total heat release of an igniting case the main data output from the experiment, the pressure versus time curve, is analyzed by a code written in MATLAB which outputs both a heat release rate versus time graph and the numerical value of the net heat release. To convert the pressure versus time trace into heat release rate the 1st Law of Thermodynamics was used to derive an equation relating the change in pressure and volume versus time to the rate of heat release inside the combustion chamber [39] [40].

$$\frac{\gamma_{mix}P}{\gamma_{mix}-1} \frac{dV}{dt} + \frac{1}{\gamma_1-1} V \frac{dP}{dt} + \dot{Q}_w = \frac{dQ}{dt} \quad (9)$$

γ is the ratio of specific heats of the fuel and oxidizer mixture, P is the pressure inside the combustion chamber, V is the volume of the combustion chamber, \dot{Q}_w is the rate of heat transfer to the combustion chamber walls, and $\frac{dQ}{dt}$ is the heat release rate. The γ of each individual species is calculated at each time step using the five variable polynomial specific heat equation for each different species. Both pressure and volume are input variables from the output data file from each experimental run. Heat transfer to the walls of the combustion chamber is calculated by comparing the pressure versus time trace of a non-igniting case to an adiabatic pressure versus time trace. In the adiabatic pressure versus time trace the pressure after compression remains constant independent of time, while the real pressure versus time trace decreases with time due to the heat transfer from the hot compressed gases to the cold the combustion chamber walls. Net heat release is calculated by integrating under the heat release rate curve.

2.5.3 Lean Limit

The lean limit of a fuel/oxidizer mixture is the highest Air Fuel ratio, or lowest equivalence ratio, that will result in a flammable mixture. The lean limit of a fuel/oxidizer mixture is very important for real world combustion applications, especially large bore natural gas engines which are typically operated very near the lean limit, since it dictates how much fuel must be used to run the engine and therefore a large portion of the operating costs.

To calculate the lean limit of a specific fuel/oxidizer mixture an equivalence ratio sweep is performed in which a series of tests are run at varying the equivalence ratios. For equivalence ratio sweeps the equivalence ratio ranges from a high equivalence ratio that will result in complete combustion of the fuel, typically $\phi=0.6$, all the way down to an equivalence ratio that will no longer ignite, roughly $\phi=0.25$. To ensure that the results of the equivalence ratio sweep are solely due to changes in equivalence ratio, the fuel energy and laser energy are held constant for each different equivalence ratio. Next, the pressure verse time curve from each of the different equivalence ratio runs is input into the Heat Release Code and the corresponding net heat release from each different equivalence ratio is collected. Using the net heat release from each individual case the combustion efficiency is calculated. The combustion efficiency, termed χ , is a non-dimensional number that represents the completeness of combustion by taking the ratio of the net heat release to the total initial fuel energy.

$$\chi = \frac{Q_{net}}{E_{CH_4/Air}} \quad (10)$$

Q_{net} is the net heat release and $E_{CH_4/Air}$ is the total initial fuel energy. The total initial fuel energy is calculated by multiplying the mass of fuel in the combustion chamber by the Lower Heating Value of the fuel.

$$E_{CH_4/Air} = m_{CH_4} * LHV \quad (11)$$

Finally, the combustion efficiency of each different equivalence ratio run is plotted and a logistic curve fit is applied to the data. The lean limit is then defined as the equivalence ratio at which the combustion efficiency is equal to 0.9.

3 THE EFFECT OF ADDITIVES ON LASER IGNITION OF LEAN PREMIXED NATURAL GAS/AIR MIXTURES

In this chapter, the results of experiments aimed at determining the effect of fuel additives on spark ignited natural gas engines are presented. Laser ignition experiments were conducted in the CSU RCM to determine the effectiveness of additives in extending the lean flammability limit of methane/air mixtures at elevated temperatures and pressures.

3.1 Ignition of Methane/Air Mixtures

Laser ignition of methane/air inside the RCM was investigated at various equivalence ratios with the support of Ciprian Dumitrache. For the experiments described in this section, the fuel and air were brought inside the chamber separately and the desired equivalence ratio was set by the partial pressures of the constituents. For proper comparisons between the various RCM test runs it is important to have a constant compression temperature and pressure in each case. Therefore, due to the differing specific heats for the different equivalence ratios studied, the initial temperature (before compression) was varied accordingly as governed by Equation 1. In this manner it was possible to achieve $T_{comp}=782$ K for all tests. More information about the test conditions are provided in Table 3.1 below.

Table 3.1 Test conditions for the laser ignited CH₄/Air mixtures presented in Figure 3.1.

ϕ	P_o [bar]	T_o [K]	P_{comp} [bar]
1	1	328	27.6
0.9	1	326	27.8

0.8	1	324	28
0.7	1	322	28.2
0.6	1	320	28.4
0.5	1	318	28.6
0.4	1	316	28.8

It should be noted again that none of the test conditions summarized in Table 3.1 resulted in auto-ignition. Pressure traces of laser ignited methane-air mixtures for various equivalence ratios are presented in Figure 3.1. For each test condition, a minimum of three tests were performed and each curve is plotted with a confidence interval corresponding to one standard deviation. Each pressure trace exhibits two peaks. The first peak (at time of ~12 ms) corresponds to the end of compression, while the second peak is caused by the heat release from chemical reaction. As the equivalence ratio is varied, the amplitude of the second peak varies since varying amounts of fuel were used (in order to keep the initial pressure constant at $P_0=1$ bar). For all the results shown in Figure 3.1, the laser energy was held constant at 20 mJ. Another feature that is evident from Figure 3.1 is the increase in the ignition delay period for leaner mixtures. In this laser ignition experiments described in this chapter, the ignition delay period was defined as the time period between when the laser is fired (time of ~26 ms) to the moment when the pressure gradient becomes positive. Figure 3.1 also shows that the rate of pressure rise decreases for leaner mixtures, which likely corresponds to lower flame speeds. Variations in peak pressure and ignition delay are shown in Figure 3.2.

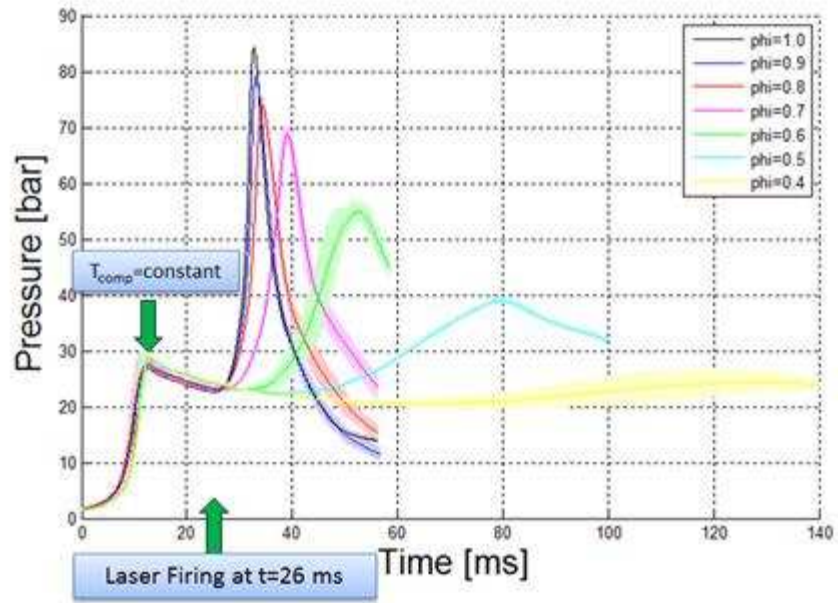


Figure 3.1 Pressure traces for laser ignition of methane-air mixtures at various equivalence ratios: $P_0=1$ bar, $T_{comp}=782$ K, and $E_{laser}=20$ mJ.

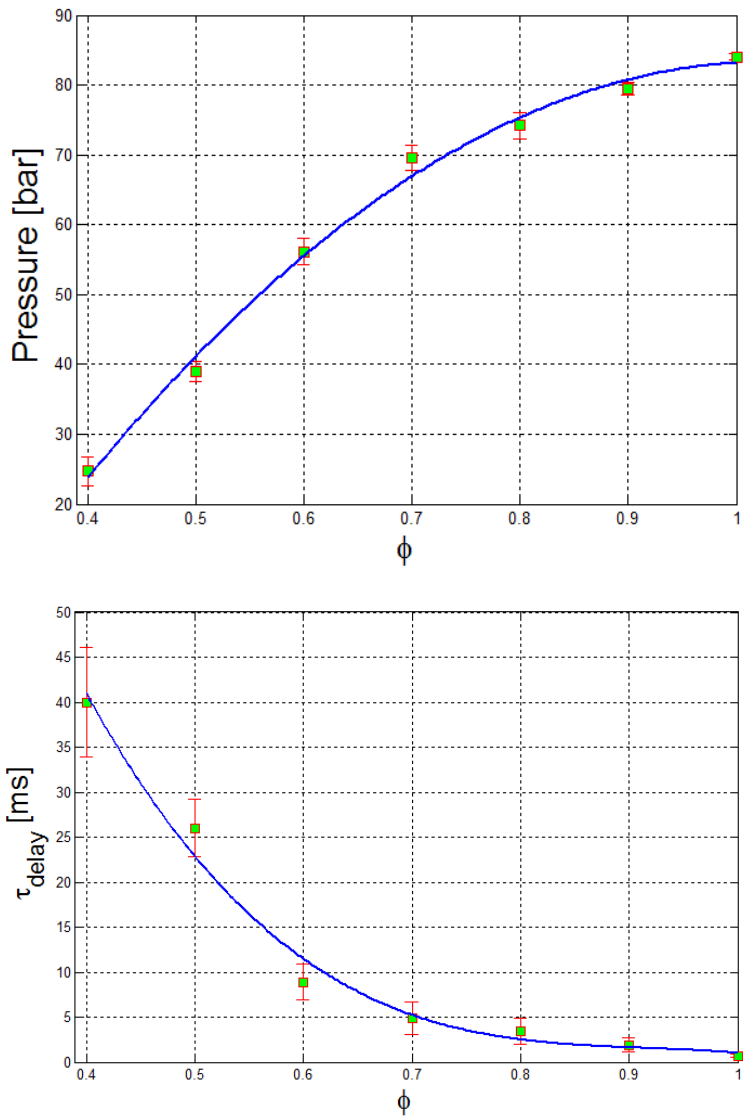


Figure 3.2 Top: Variation of peak pressure with equivalence ratio. Bottom: Variation of ignition delay with equivalence ratio.

3.1.1 Lean Limit Measurements

As is observed from Figure 3.1, leaner mixtures lead to decreasing peak pressures. However, since fuel energy was not kept constant for the above experiments, it cannot be inferred that the decrease in peak pressure is due to incomplete combustion. As a consequence, the lean limit of methane/air mixtures was explored by keeping fuel energy constant (which is also more consistent with real engine operation where varying the boost pressure is used to keep

the fuel energy constant). Laser energy and laser firing time were fixed at constant values of 5 mJ and 26 ms, respectively, for all lean limit experiments. Results for the lean limit experiments are presented in Figure 3.3, and the test conditions are listed in Table 3.2. The energy content of the fuel charge, $E_{\text{CH}_4/\text{Air}}$, is found from the lower heating value (LHV) and the mass of the fuel in the combustion chamber (see equation 11).

To study the completeness of combustion for the different conditions a dimensionless efficiency completeness parameter χ , was used, which was defined as the ratio of the net heat release (found from the pressure traces) to the energy content of the fuel charge (see equation 10).

Results of the lean limit studies are shown in Figure 3.3. The heat release computation is based on the pressure data analysis as described by Heywood [39] [40]. If complete combustion is achieved, the net heat release should match the fuel energy, minus a small fraction corresponding to mass losses due to the presence of blow-by, giving χ approaching unity. Figure 3.3 shows that as the equivalence ratio drops below ~ 0.44 the heat release during the combustion process decreases (i.e. χ decreases) thus indicating incomplete combustion. The selection of which χ to adopt to characterize the lean limit is arbitrary and for this study the lean limit was defined as the equivalence ratio that results in $\chi=0.9(=90\%)$, denoted ϕ_{90} . In a real engine, turbulent mixing and shearing effects are more predominant than in the RCM so somewhat different lean limits may be expected. Figure 3.4 shows two example pressure traces: one for a “strong” (complete) ignition event ($\chi=0.84$) and one for a “weak” (incomplete) ignition event ($\chi=.22$). The “weak” ignition pressure trace exhibits a lower peak pressure reduced and combustion efficiency compared to the “strong” ignition pressure trace.

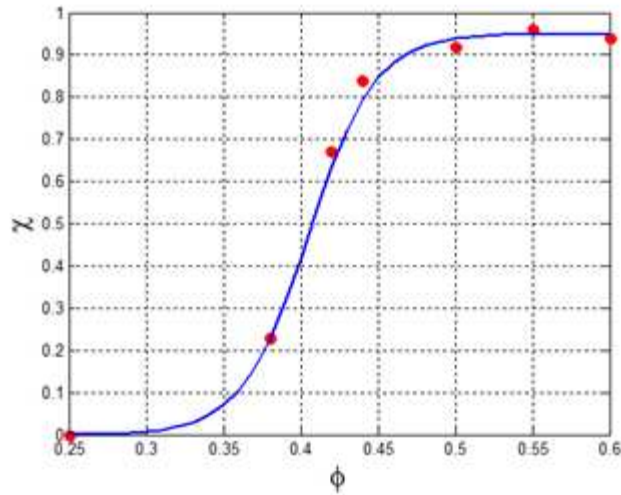


Figure 3.3 Figure 3.3: Fraction of net heat released for various equivalence ratios. The lean limit is found to be $\phi_{90}=0.47$, $\phi_{50}=0.41$, and $\phi_{20}=0.37$.

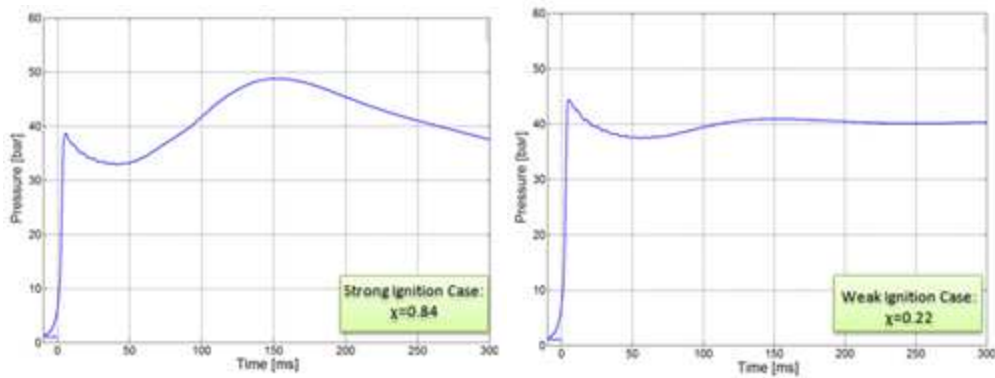


Figure 3.4 Left: an example of a “strong” ignition event ($\chi=0.84$). Right: A “weak” ignition event ($\chi=0.22$).

Table 3.2 Test conditions for the lean limit study.

ϕ	P_o [bar]	T_o [K]	P_{comp} [bar]
0.6	1	320	28.4
0.55	1.086	319	30.9

0.5	1.188	318	34
0.44	1.342	317	38.5
0.42	1.4	316	40.2
0.25	2.314	312	67.4

3.1.2 Minimum Ignition Energy

Other important parameters to characterize the laser ignition are the Minimum Ignition Energy (MIE) and Minimum Spark Energy (MSE). Generally the MIE is greater than the MSE though this is not always the case. In certain cases the MIE and MSE are equal (for example when MSE is very high due to use of a long focal length lens). Past studies have shown that laser ignited mixtures can require more energy than conventional CDI systems [41] [42] which is largely attributed to different processes of plasma formation [6] [43]. Results of MSE and MIE studies are shown in Figure 3.5. Specifically, for MIE we plot the probability of successful ignition (based on multiple tests) versus laser energy, while for MSE we plot the probability for spark formation. Table 3.3 shows test conditions for all methane/air mixtures at fixed compression temperature. The test conditions were specifically chosen such to have a large difference between MSE and MIE. (For example, at the tests conditions of Table 3.1 and Figure 3.1 it was found that even the lowest energy spark ignited all the fuel-air mixtures attempted, i.e. MSE~MIE.). Figure 3.5 shows that both MSE and MIE exhibit a stochastic behavior as has been reported by other research groups. The MIE and MSE data plotted in figure 3.5 was fitted using the logistic function and weighting method discussed in section 2.13.1.

We infer values of MIE and MSE from the fits yielding $MIE_{90}=7.2$ mJ, $MIE_{50}=6.2$ mJ, $MIE_{20}=5.7$ mJ, $MSE_{90}=2.3$ mJ, $MSE_{50}=1.9$ mJ, and $MSE_{20}=1.5$ mJ. MIE_{90} is defined as the laser energy resulting in a 90% probability of ignition (and analogous for MSE and probability of spark formation).

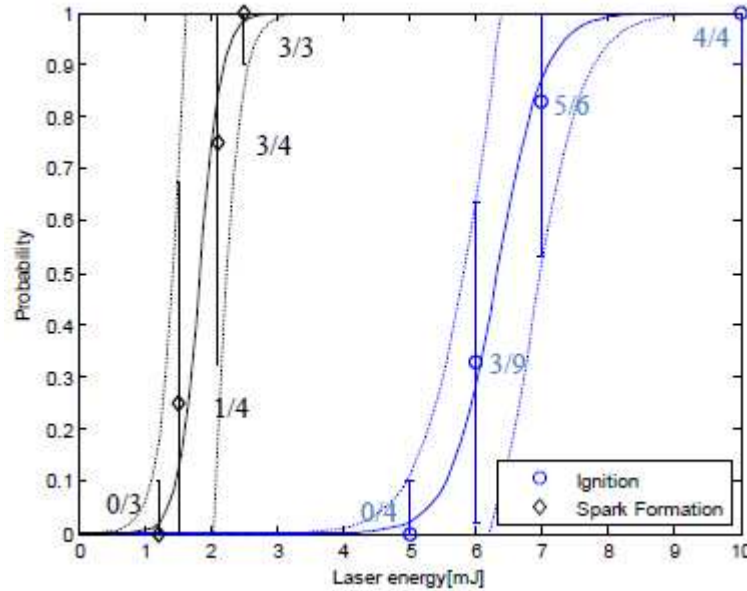


Figure 3.5 Probability of spark formation and ignition versus laser energy. Data was fitted using the logistic function to infer MIE and MSE.

Table 3.3 Test conditions for the MIE and MSE investigation as described in Figure 3.5.

ϕ	P_0 [bar]	T_0 [K]	P_{comp} [bar]	T_{comp} [K]	τ_{Laser} [ms]
0.4	1	300	29	750	100

3.1.3 Schlieren Imaging

The sequence of events leading to the laser spark formation was revealed using the high speed Schlieren Imaging setup described in Figure 2.9 (on the bench top, not RCM). Depicted in Figure 3.6 is the spatial and temporal evolution of the spark. In the pictures below the beam

enters the focal region from the left. At a time of $1\ \mu\text{s}$ after the pulse ends, the hot plasma kernel is already formed. Due to the rapid heating of the plasma, a blast wave is being generated and it is becoming visible in the pictures at $3\ \mu\text{s}$. While the blast wave propagates outward, the plasma contracts slightly as it cools down and, $30\ \mu\text{s}$ later, plasma recombination takes place. At later times (above $30\ \mu\text{s}$) thermal/fluid dynamics processes dominate including the presence of a toroidal structure (as has also been reported in the literature [4] [44]). The structure of the spark kernel plays important role in combustion, the formation of a third lobe which is seen here propagating in the direction of beam. It has been shown in the literature that, although the third lobe arises from gas-dynamics rather than chemical effects, it leads to an enhancement of flame spreading [4].

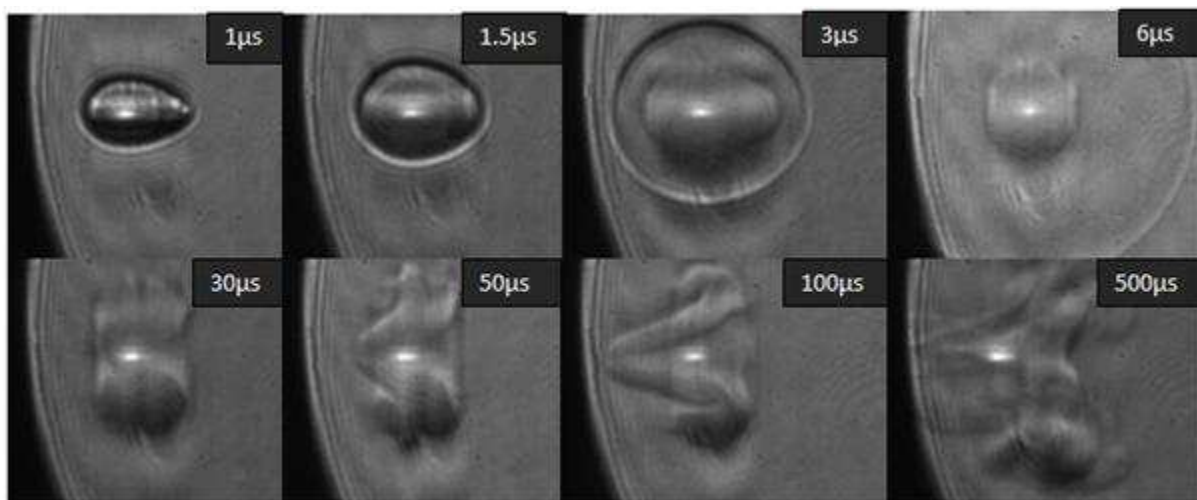


Figure 3.6 Schlieren image sequence depicting the formation of a laser spark in atmospheric air.

3.2 Investigation of Additives for Spark Ignited Natural Gas Engines

After conclusion of baseline MIE and Lean Limit testing for pure methane/air mixtures, it was possible to test various different fuel additives and compare their performance to the baseline. The specific methane additives tested were specified by the sponsor of the project. The three different additives that were tested were 1,1-Di (tert-butylperoxy) (DTBP), Nitromethane

(NM), and Dimethoxymethane (DMM) at varying concentrations determined based on the reactivity of the individual additive. See Figures 3.7 [45], 3.8 [46], and 3.9 [47].

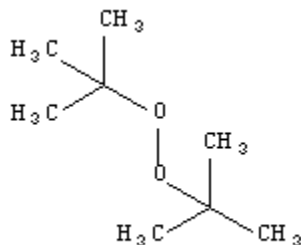


Figure 3.7 1,1-Di (tert-butylperoxy).

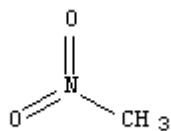


Figure 3.8 Nitromethane.



Figure 3.9 Dimethoxymethane.

3.2.1 Effect of Additives on Auto-ignition of Methane/Air Mixtures

The natural gas additive testing described in this chapter was performed in the RCM using the laser ignition set up as the ignition source. As such, it was vital to prove that the source of ignition was the laser spark kernel and not auto-ignition of the compressed mixture. To be certain that auto-ignition would not be an issue, the highest concentration of each additive for which auto-ignition would not occur was determined by performing compression ignition experiments in the RCM without firing the laser. If the mixture did not auto-ignite, then it could be concluded that when tested with the laser ignition set up it was the firing of the laser that

initiated combustion. The initial conditions of the auto-ignition testing were the same as those listed in Table 3.3, with the exception of no laser firing. Figures 3.7, 3.8, and 3.9 illustrate the pressure vs. time curves of the three different natural gas additives.

All three additives were initially tested at a concentration of 5% to confirm that auto-ignition would not occur. In the cases of NM and DMM, no auto-ignition was observed at this concentration and, therefore, these additives were tested at concentrations of 5% and less. In the case of DTBP, auto-ignition was observed at the 5% concentration, therefore the concentration of 1% was also tested. At the lower 1% concentration no auto-ignition was observed so it was concluded that concentrations of 1% and less of DTBP could be tested in the subsequent laser ignition experiments.

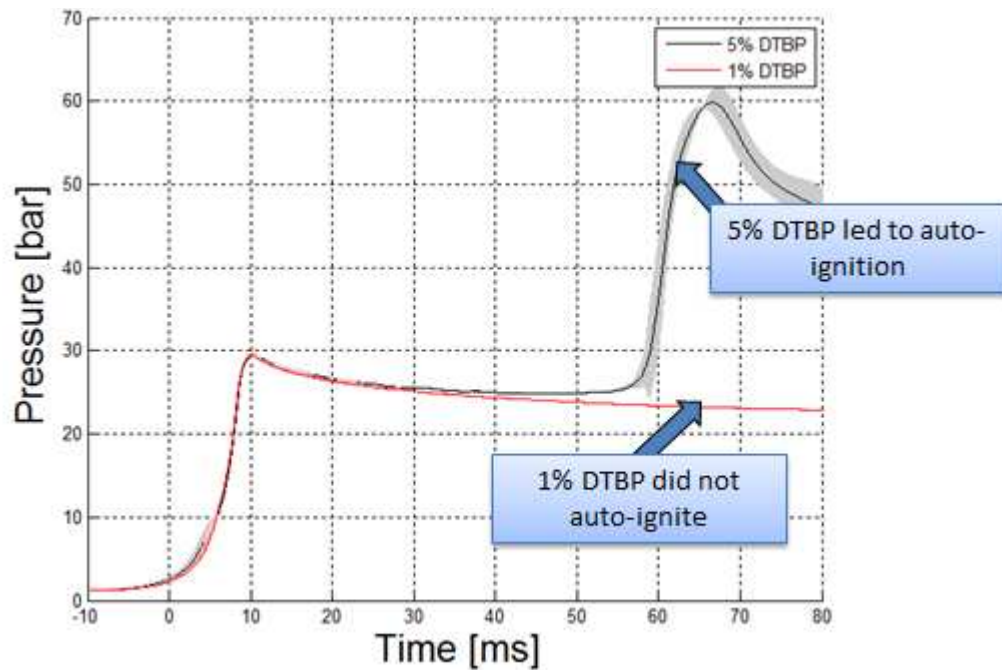


Figure 3.10 Auto-Ignition testing of 1% and 5% 1,1-Di (tert-butylperoxy) (DTBP) in lean ($\phi= 0.4$), premixed methane/air mixtures in the CSU RCM.

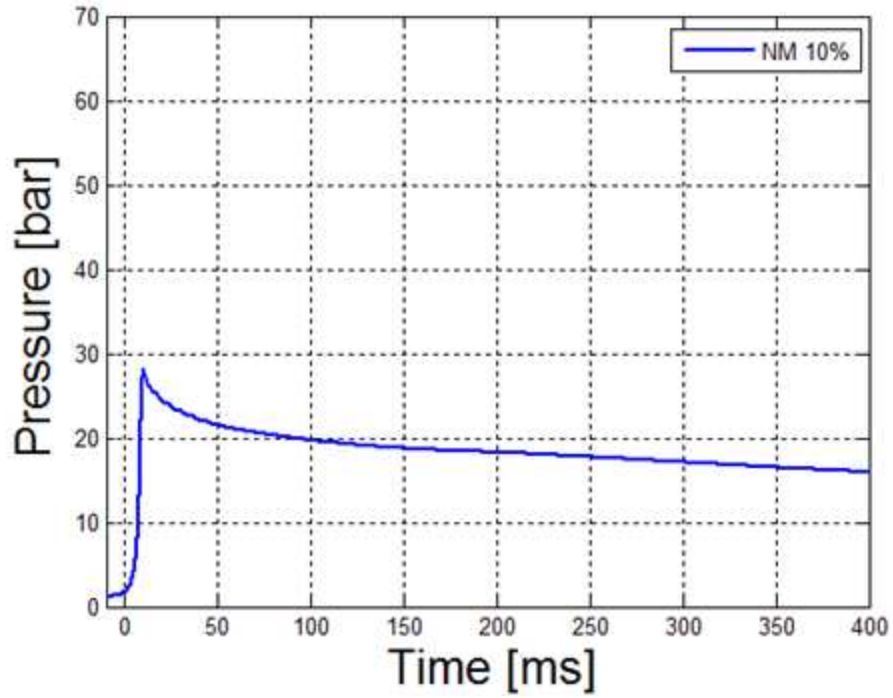


Figure 3.11 Auto-Ignition testing of 10% Nitromethane (NM) in in lean ($\phi= 0.4$), premixed methane/air mixtures in the RCM.

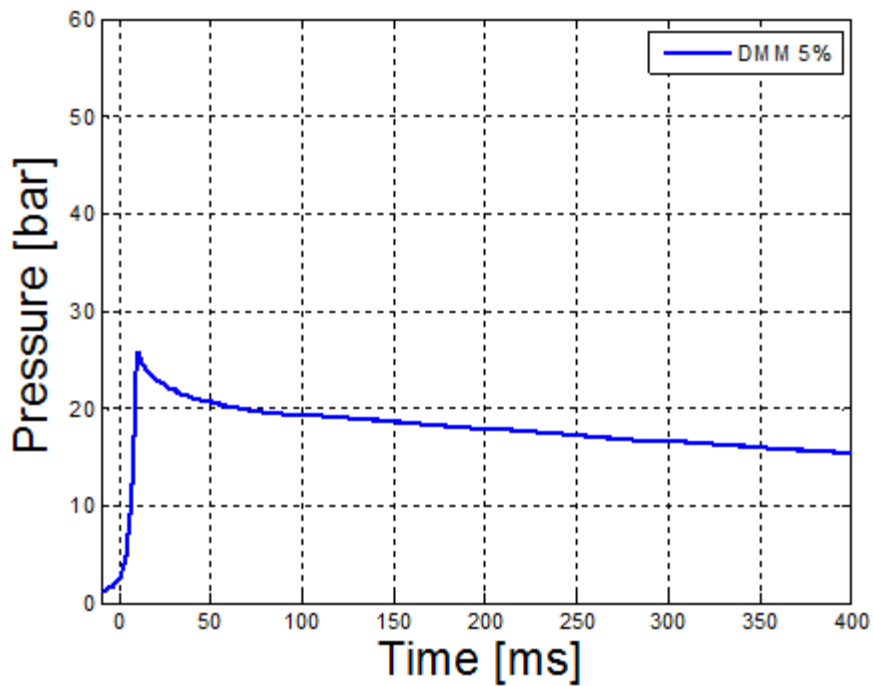


Figure 3.12 Auto-Ignition testing of 5% Dimethoxymethane (DMM) in in lean ($\phi= 0.4$), premixed methane/air mixtures in the RCM.

3.2.2 Effect of Additives on Minimum Ignition Energy of Methane/Air Mixtures

After concluding the auto-ignition experiments for each of the three additives, it was possible to progress to MIE testing. The initial conditions of the methane additive MIE testing are the same as the pure methane/air MIE testing, summarized in Table 3.3. The pulse energy of the laser was systematically varied from a high pulse energy that resulted in a high probability of ignition, to a low pulse energy that resulted in no ignition

DTBP at concentrations of 0.2% and 1% were added to lean methane/air mixtures with an equivalence ratio of $\phi = 0.4$ and tested to determine their effect on the MIE of methane/air mixtures in the RCM. An initial laser energy that resulted in 100% ignition probability was determined. In the case of DTBP, 5 mJ laser pulse energy resulted in 100% probability of ignition for both concentrations. From this initial energy level the laser pulse energy was systematically reduced until an ignition probability of zero was reached. In the case of DTBP, the lower energy level was determined to be 4 mJ for both concentrations tested. At each of the pulse energies, at least three tests were performed to insure that the stochastic nature of MIE was fully characterized. For this study, ignition events were characterized as any test that experienced a quantifiable pressure rise after the firing of the laser, which indicated the presence of heat release from chemical reaction of the fuel/air mixture. After collecting data from the necessary number of experiments, the probability of ignition and laser energy vectors were input into MATLAB to generate the MIE curves which were then plotted along with the baseline MIE curve for comparison. Figure 3.10 presents the results of the DTBP MIE experiments in comparison to the baseline.

One metric to compare the performance of additives is MIE_{90} , which is the energy level that results in a 90% ignition probability. The MIE_{90} is calculated from a curve fit generated

from the raw data since no data points fall exactly on the 90% line. For 0.2% DTBP, a value of $MIE_{90}=4.8\text{mJ}$ was determine and for 1% DTBP, a value of $MIE_{90}= 4.6 \text{ mJ}$ was determine. Both of the calculated MIE_{90} values for DTBP are significantly less than the baseline methane/air MIE_{90} value of 7.2 mJ, which represents a 33% and 36% reduction in MIE, respectively for the DTBP additive.

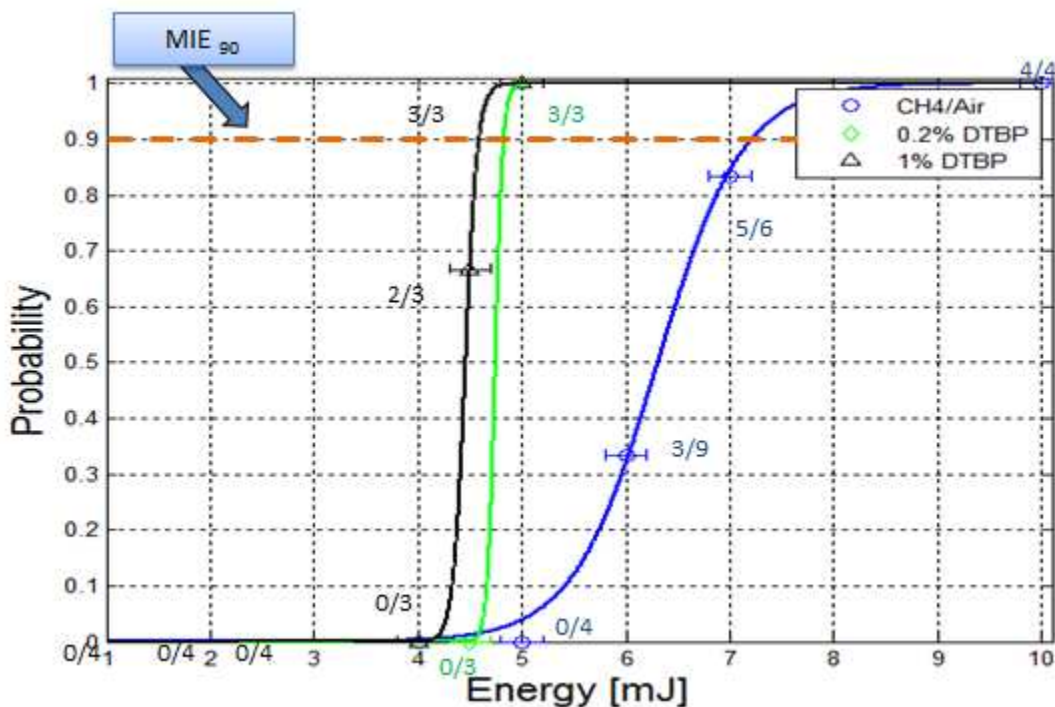


Figure 3.13 Results of Minimum Ignition Energy Testing of 1,1-Di (tert-butylperoxy).

Nitromethane (NM) was tested to determine the MIE_{90} for 0.2%, 1%, and 5% concentrations blended into a methane/air mixture at an equivalence ratio of $\phi = 0.4$. For the NM, the MIE_{90} was determined to be 4.7 mJ, 2.7 mJ and 2.3 mJ for NM concentrations of 0.2%, 1% 5%, respectively. Therefore, the addition of NM resulted in a 35%, 63%, and 68% reduction, respectively, in the MIE in comparison to the baseline methane/air mixture. The results suggest that the addition of varying concentrations of NM to methane/air mixtures results in a non-linear reduction in MIE. When 5% NM was added to a methane/air mixture, the MIE approaches the

MSE of the mixture. Figure 3.11 illustrates the ability of NM to lower the MIE of methane/air mixtures.

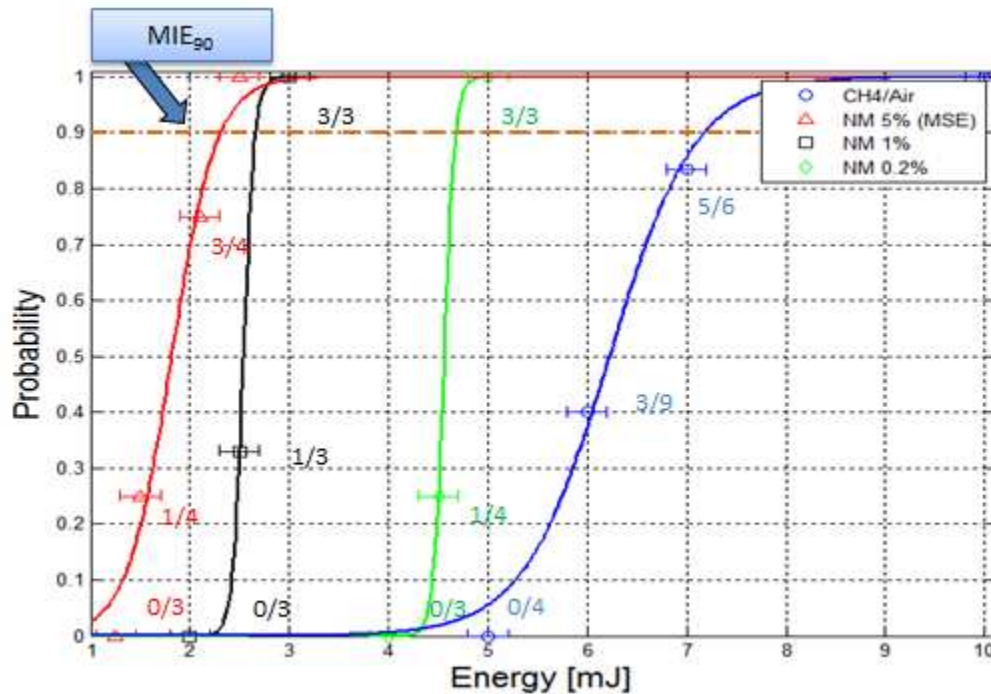


Figure 3.14 Results of Minimum Ignition Energy Testing of Nitromethane (NM) in methane/air mixtures at $\phi=0.4$.

Finally, DMM was tested to observe its effect on the MIE of methane/air mixtures. DMM was tested at the concentrations of 0.2%, 1%, and 5%, and the respective MIE_{90} were determined to be 2.4 mJ, 5.2 mJ, and 2.3 mJ. Figure 3.12 illustrates the effects of DMM addition on MIE. These reductions in MIE represent 67%, 27%, and 68% reductions, respectively, in comparison to the baseline methane/air mixtures. Similar to the behavior of 5% NM addition, 5% DMM resulted in the MIE approaching the MSE of the mixture. However, the performance of 0.2% DMM concentration when compared to the higher 1% concentration was particularly notable. Specifically, the lower 0.2% DMM concentration appears to outperform the higher concentration in reducing the MIE of the mixture, which was a characteristic that defied explanation and was not observed in any of the other additives. To further investigate this

phenomenon and determine if it was a repeatable result, the experiments with 0.2% DMM were repeated, along with even lower DMM concentrations of 0.04% to determine their effect on methane/air MIE.

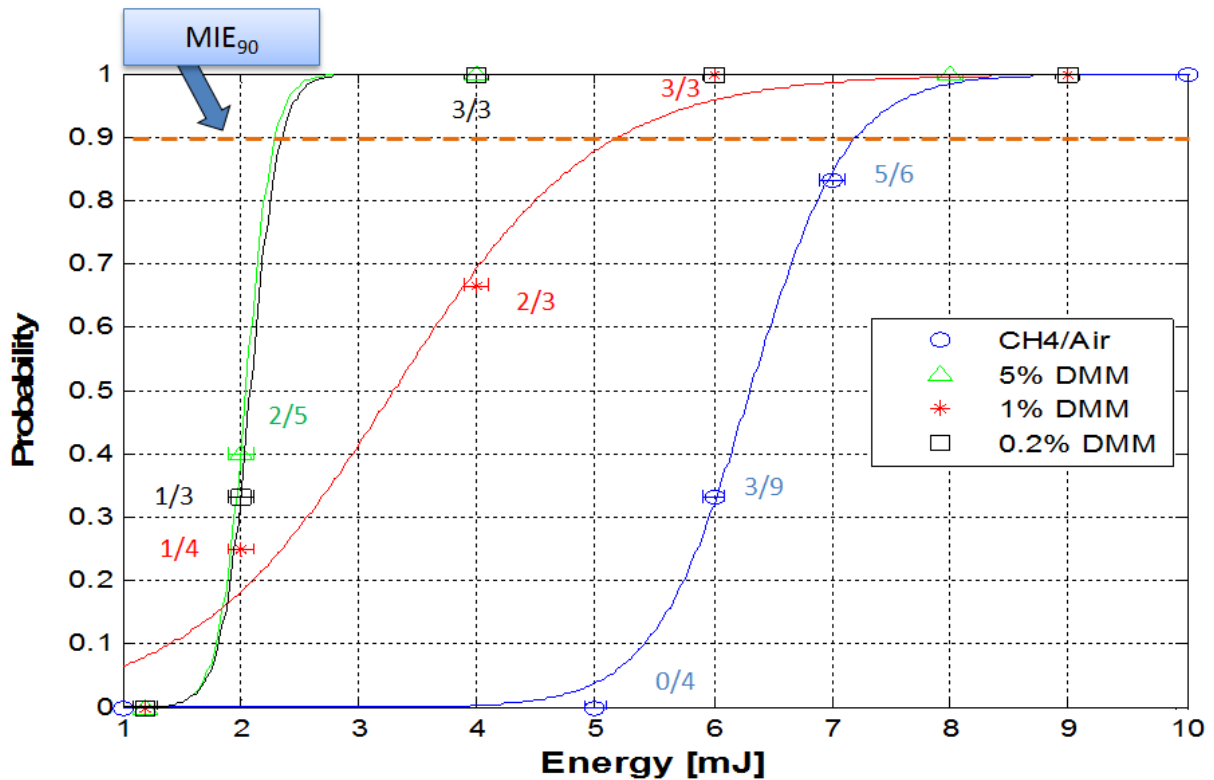


Figure 3.15 Results of Minimum Ignition Energy testing of Dimethoxymethane.

Figure 3.13 illustrates the additional MIE testing of DMM at the lowest concentrations of 0.04% and 0.2%. When the 0.2% DMM experiments were repeated, the MIE₉₀ increased to 4.1 mJ compared to the previously measured 2.4 mJ. The most likely explanation for this reduction in MIE is that the RCM combustion chamber, fuel filling lines, or liquid fuel blending chamber had become contaminated with a previously tested additive, which is an issue that has been experienced in the past. To solve the contamination issue, the combustion chamber, fuel lines, and liquid fuel mixing tank were heated to 70°C while being evacuated for approximately 2 hours. This procedure, known as baking, vaporizes and evacuates any unwanted contaminants.

When the extremely low concentration of 0.04% was investigated its MIE_{90} was observed to be 7.2 mJ, equal to the MIE_{90} of the pure methane/air baseline. At such low concentrations DMM therefore has no effect on the MIE of Methane/Air mixtures.

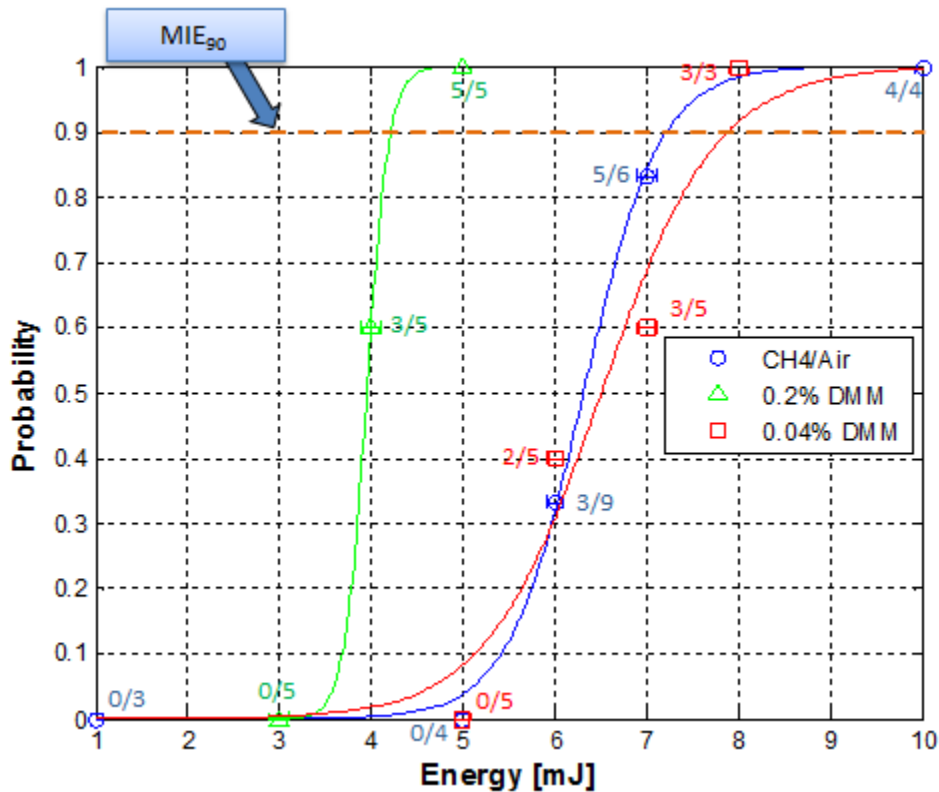


Figure 3.16 Results of Continued Minimum Ignition testing of Dimethoxymethane.

3.2.3 Effect of Additives on Lean Limit of Methane/Air Mixtures

After conclusion of baseline methane/air lean limit testing, it was possible to transition into lean limit testing of the three different methane fuel additives: DMM, DTBP and NM. All three additives were tested at a concentration of 1% to insure that auto-ignition did not occur, and the energy content at each of the different equivalence ratios tested was held constant. Laser firing time and energy were held constant at 26 ms after the start of compression and 5mJ pulse energy. The remaining initial conditions for lean limit testing were identical to those summarized above in Table 3.2.

Similar to MIE testing, the metric used for comparison of the lean limit reduction performance of each additive was $\phi_{\text{Min}90}$, which was defined as the equivalence ratio required to result in a 90% combustion efficiency ($\chi=0.9$). The $\phi_{\text{Min}90}$ value was calculated from the logistic curve fit of the data in a similar manner to way that the MIE_{90} was calculated. Lean limit tests at varying equivalence ratios were conducted and their pressure traces were input into the MATLAB Heat Release program. To generate the logistic curve fits for lean limit data, the combustion efficiencies of each additive were input into the MATLAB code along with the corresponding equivalence ratio vectors. Using these logistic function curve fits, the equivalence ratio that would result in 90% combustion efficiency were then extrapolated.

When DTBP was tested for its ability to reduce the lean limit of methane/air mixtures, a value of $\phi_{\text{Min}90}$ of 0.43 was observed, which represents an 8.5% reduction in the lean limit. For NM, a value of $\phi_{\text{Min}90}$ of 0.36 was observed, which represents a 23.4% decrease in the lean limit. Finally, DMM exhibited a $\phi_{\text{Min}90}$ of 0.53, which represents an increase in the lean limit of 12.8% percent. Figure 3.14 presents the results of the natural gas fuel additive lean limit testing.

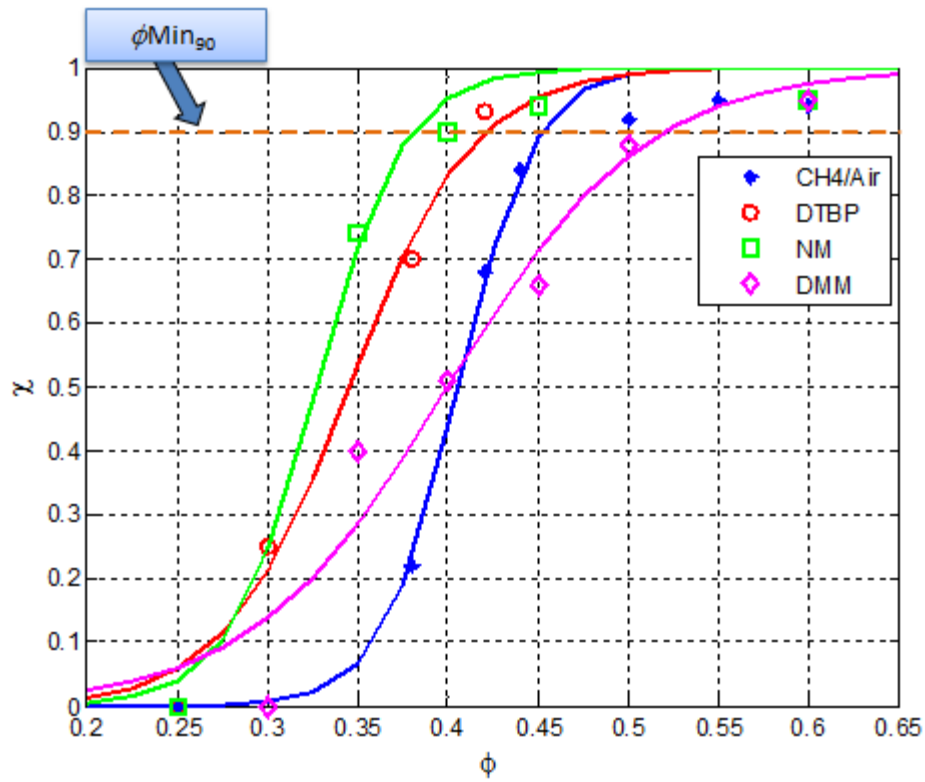


Figure 3.17 Lean Limit Testing of 1,1-Di (tert-butylperoxy) (DTBP), Nitromethane (NM), and Dimethoxymethane (DMM).

4 THE EFFECT OF ADDITIVES ON HOMOGENEOUS AUTO-IGNITION OF GASOLINE SURROGATE FUELS

In this chapter, the results of the gasoline fuel additive study conducted in the CSU RCM are presented. The fuel additives were added to gasoline surrogate fuels, which included 100% isooctane, and toluene reference fuel (TRF) blends (toluene, n-heptane and isooctane). The effect of the fuel additives on measured ignition delay period and fractional low temperature heat release were examined. The isooctane and TRF results were compared against time-dependent, 0-dimensional computations using detailed chemical kinetics.

Since the study presented in this thesis represents the first use of the CSU RCM with liquid fuels, the performance of the RCM was benchmarked against data obtained by other investigators [27]. Specifically, an ignition delay study of pure isooctane was conducted in the CSU RCM and compared against previously published isooctane ignition delay data from other RCM's and shock tubes [27]. The measured ignition delay data from the CSU RCM was also compared against CHEMKIN simulation results using best available detailed chemical kinetic mechanisms.

4.1 CHEMKIN Modeling

The chemical kinetics modeling software CHEMKIN [48] was employed to model the homogeneous compression and ignition process in the RCM. The modeling study was used to generate simulated isooctane ignition delay data to compare against the RCM isooctane ignition delay data (obtained in this study and by previous investigators) and to inform decisions on the subsequent additive testing in which additives were added to isooctane and TRF blends. The detailed chemical kinetic mechanism developed by Mehl (approximately 1537 species and 5935

reactions) was selected for use when modeling the homogeneous compression-ignition experiments in the RCM for two reasons [49]. First, particular attention was devoted to linear and branched saturated hydrocarbons (n-heptane and isooctane), olefins (1-hexene), and aromatics (toluene) when developing the Mehl chemical mechanism. Second, the Mehl chemical mechanism was validated previously against experimental data from RCMs and Shock Tubes, which will be shown later to closely agree with the experimental data from the CSU RCM.

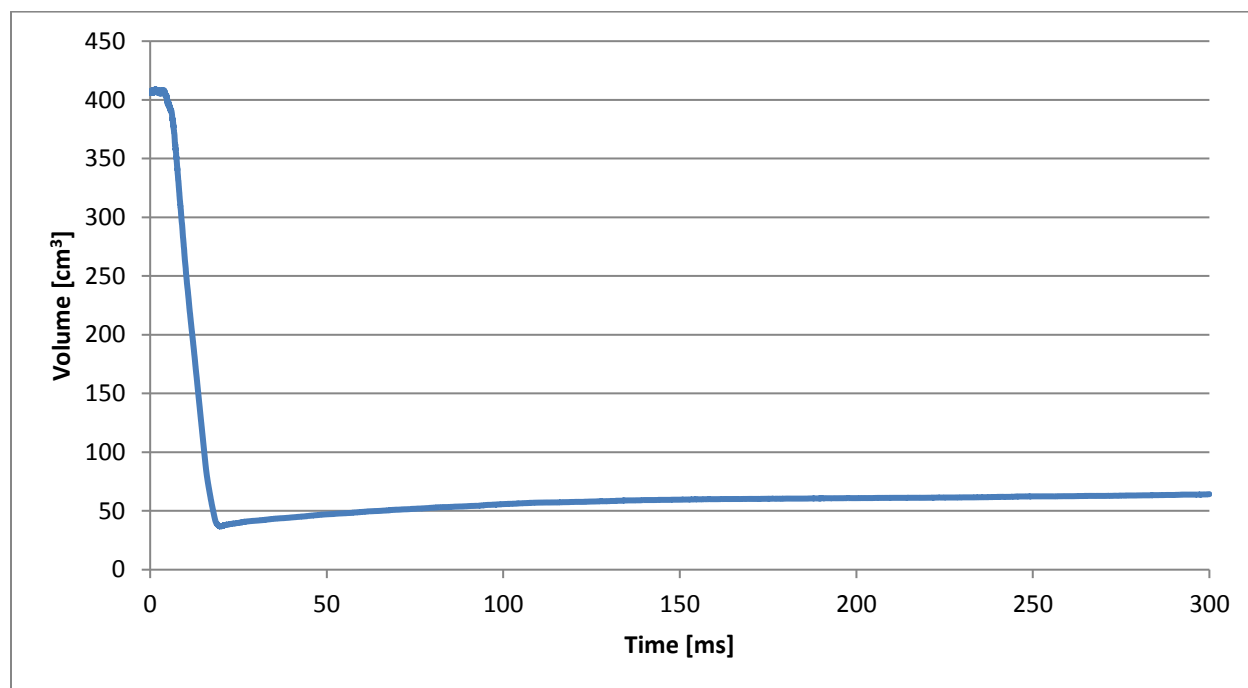


Figure 4.1 RCM Volume vs. Time curve.

Initial simulations were performed utilizing a volume vs. time curve for the compression cycle of the RCM, see Figure 4.1. Although the actual volume of the RCM is fixed after compression to top dead center (TDC), the volume vs. time curve that was input into CHEMKIN included an artificial expansion stroke after TDC, which reproduced the pressure decrease that is observed experimentally after compression due to temperature decrease in the compressed gas mixture from heat loss to the combustion chamber walls. As shown in Fig. 4.2, this technique effectively reproduces the experimental pressure decrease observed after compression.

However, because of the size of the chemical kinetic mechanism, these computations were extremely time consuming, taking approximately 24 hours to complete one computation. Therefore, after several initial simulations were completed using the full RCM volume vs. time data, subsequent computations were performed using constant volume conditions at a fixed initial temperature and pressure, which corresponded to the compressed pressure and temperature in the RCM at TDC. The use of constant volume computations greatly decreased the time required for each simulation, thereby enabling examination of a large array of potential experimental conditions (fuel composition, compressed temperatures and pressures). However, the homogeneous ignition delay behavior in these simulations differs slightly from the experiments because in the latter case the temperature is decreasing during the chemical induction period due to heat loss, whereas in the constant volume computations the temperature remains fixed during the chemical induction period.

The initial conditions of the constant volume simulations were obtained by calculating the temperature and pressure time averages from the end of compression to the start of combustion. To confirm that a constant volume approximation was reasonable, two simulations of the ignition delay of a stoichiometric mixture of 30% toluene, 20% isooctane, and 50% n-heptane were performed. One simulation utilized the full volume trace and the other utilized the constant volume assumption. The initial temperature and pressure of the full volume trace simulation were 300 K and 1 bar, and the time averaged initial temperature and pressure of the constant volume simulation were 634 K and 19.53 bar.

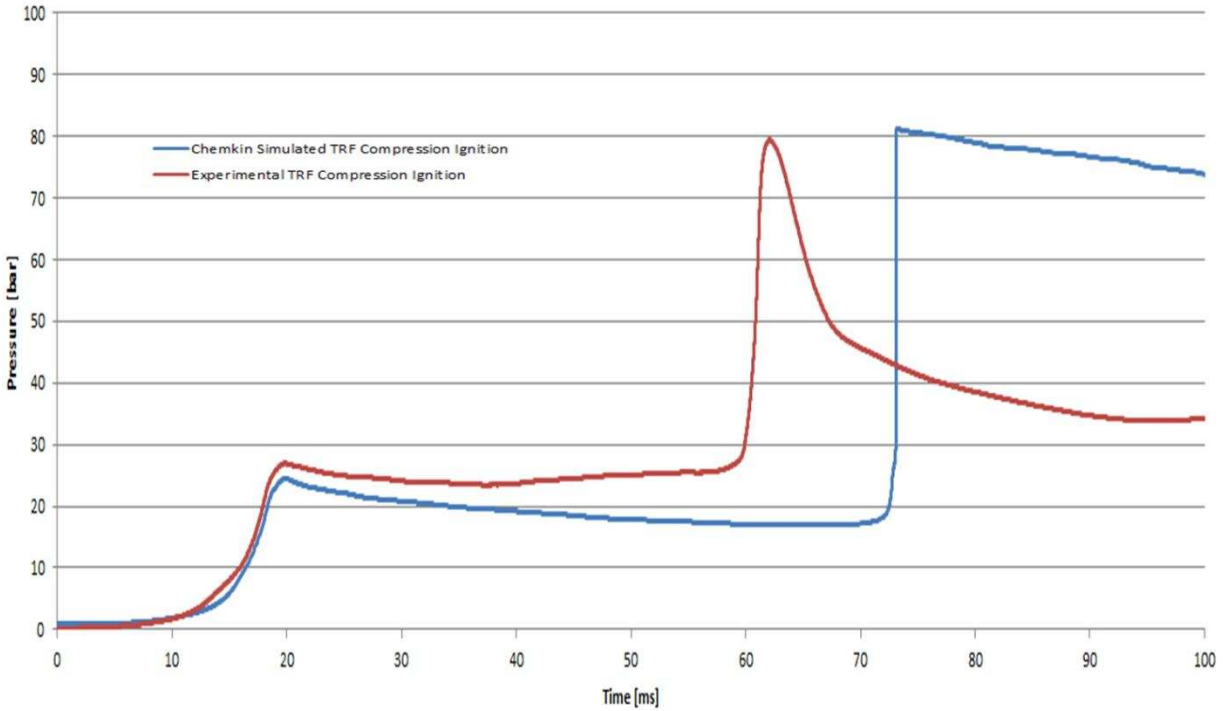


Figure 4.2 Simulated pressure vs. time for a stoichiometric blend of 30% Toluene, 20% iso-octane, 50% n-heptane in air with initial conditions of 1 bar and 300 K. Computations were performed using varying volume vs. time data.

As shown in Fig. 4.2, the variable volume RCM simulation, the pressure initially begins at 1 bar at time zero and then is adiabatically compressed to approximately 25 bar over the next 20 ms. Once the volume reaches a minimum at TDC, the volume slowly expands, which is contradictory to the experiments wherein the pistons are held in the TDC position by pneumatic pressure in the air chambers. Figure 4.1 displays the RCM combustion chamber volume vs. time curve. In the simulation, the volume expands after TDC to slowly decrease the pressure in the combustion chamber simulating heat losses from the hot compressed gases inside the combustion chamber to the cold combustion chamber walls. Approximately 46 ms after TDC, the entire gaseous mixture homogeneously ignites. The heat released in the combustion process results in the pressure inside the combustion chamber increasing from approximately 17 bars to 81 bars in

only 3 ms. After the maximum combustion pressure is reached, the pressure decreases due to the simulated expanding volume.

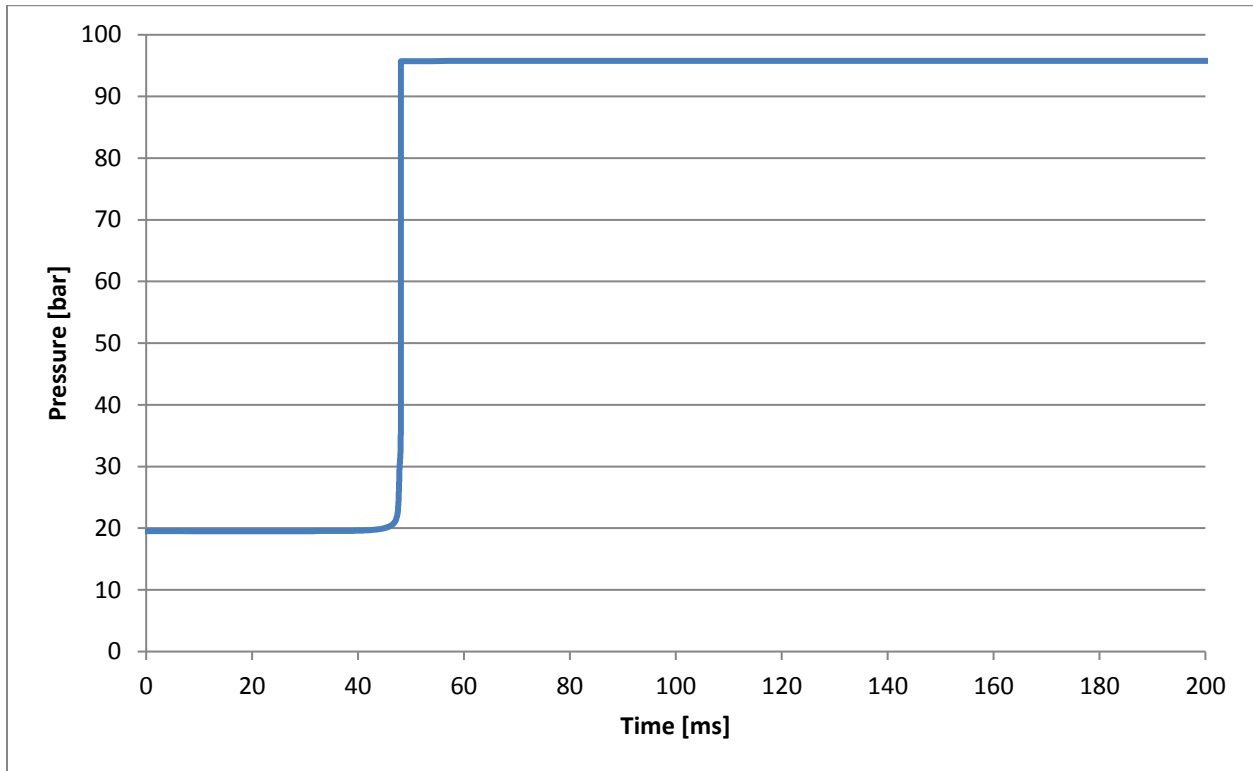


Figure 4.3 Simulated pressure vs. time for a stoichiometric blend of 30% Toluene, 20% isooctane, 50% n-heptane in air with initial conditions of 1 bar and 300 K. Computations were performed using constant volume.

In the constant volume simulation the pressure initially starts at 19.53 bars at time zero and does not decrease as in variable volume simulation because there is no mechanism to simulate heat loss. After approximately 40 ms heat release due to combustion causes the pressure to increase to approximately 95 bars. The peak combustion pressure in the constant volume simulation is significantly higher (95 bar vs. 81 bar) than the peak combustion pressure observed in the full volume trace simulation. The higher peak pressure in the constant volume simulation is due to difference in pressure between the two computations prior to the onset of ignition. For the constant volume computation, the pressure prior to onset of ignition is the fixed value of

19.53 bar, whereas for the full volume trace simulation, the pressure decreases below 17 bar prior to ignition.

It was observed that the start of combustion of the full volume trace simulation occurred approximately 46 ms after peak compressed pressure was achieved, and the start of combustion of the constant volume simulation occurred approximately 40 ms after the beginning of the simulation. The difference in ignition delay between the simulation run utilizing the full RCM volume trace and the constant volume assumption is 6 ms, which equates to 13% difference. Therefore it was concluded that conducting simulations using the constant volume assumption was reasonable since the greatly reduced simulation times would enable a much higher number of simulation conditions to be performed.

Once the decision was made to use the constant volume assumption when conducting CHEMKIN simulations it became possible to conduct compressed temperature sweeps of the different isooctane/O₂/inert mixtures and develop Arrhenius plots in the form of log (ignition delay period) vs. T⁻¹. Two ignition delay studies were conducted by varying initial temperature over a broad range. One study used nitrogen (N₂) as the diluent and the other used Argon (Ar) as the diluent. These computation ignition delay studies were conducted to determine whether the type diluent had a substantial effect on the predicted ignition delay period, which could be caused differences in the third body efficiencies of N₂ and Ar. The initial temperature of both the ignition delay studies was varied between 500 K and 1200 K by 50 K increments. The results indicated that the diluent type has only a minor effect on the predicted ignition delay period. This result suggested that modifying the compressed temperature of the isooctane/oxidizer mixture in the RCM by controlling the initial temperature of the mixture will be equally effective as

modifying the diluent, which can affect the compressed temperature by means of varying the ratio of specific heats of the mixture, γ , of the mixture.

4.2 Isooctane Ignition Delay Experiments

Three classes of isooctane/O₂/inert mixtures were investigated in the RCM through the use of three different classes of O₂/inert gases. The three classes of O₂/inert mixtures were synthetic Airgas Zero Air, a mixture of 21% O₂ and 79% N₂, and custom variable mixtures of 21% O₂/N₂/Ar in which the ratio of N₂ to Ar were varied. The purpose for testing three different oxidizer mixtures was threefold. First, to investigate the effect of different diluent third body efficiencies on the isooctane ignition delay curve. Second, to observe if different oxidizer mixtures would result in closer agreement between experimental ignition delay data and CHEMKIN model data. Finally, to study the two different methods for modifying the compressed pressure inside the RCM combustion chamber and their effects on ignition delay. Each compressed temperature data point was repeated between three and five times in the RCM. The average ignition delay period for each fuel/oxidizer combination at each compressed temperature is plotted in Fig 4.4 on a log scale versus 1000/T, where T is the compressed temperature. In Fig. 4.4, the error bars represent the standard deviation of the ignition delay period measurement at each compressed temperature.

Isooctane blended with synthetic Airgas Zero Air were initially tested in the RCM across a wide range of compressed temperatures. To vary the compressed temperature of the isooctane/Zero Air mixtures, the initial temperature of the mixture was varied by controlling the RCM test section temperature. Next, isooctane was blended with a blend a custom variable mixture of 21% O₂/N₂/Ar and was again tested in the RCM across a wide range of compressed temperatures. By varying the ratio of N₂ to Ar in the oxidizer mixture, the ratio of specific heats

(γ) of the entire isooctane/oxidizer/inert mixture was varied, which resulted in a variation in the compressed temperature of the mixture. When the ignition delay results of the first two classes of oxidizer mixtures were compared, it became clear that there existed a discrepancy in the results. This discrepancy prompted an investigation into the exact composition of the synthetic Zero Air. It was discovered that the specifications for the actual composition of Zero Air allow for a very wide variation in composition between 19.5% O₂/80.5% N₂ and 23.5% O₂/76.5% N₂ [50]. As a result, it was impossible to know with certainty whether the isooctane/Zero Air mixtures were being tested at stoichiometric conditions. However, since the two different oxidizer mixtures utilized different methods for modifying the compressed temperature of the mixture it was still not possible to conclude that the composition of the Zero Air was the reason for the discrepancy in the results from the two techniques. Therefore, a third class of oxidizer mixtures was tested to gain more insight.

The third class of oxidizers blended with isooctane consisted of 21% O₂ and 79% N₂ which were blended in-house and the average compressed temperature of the isooctane/oxidizer mixtures were modified by controlling the initial temperature of the RCM's test section. Instead of measuring the ignition delay periods of these isooctane/oxidizer mixtures over a wide range of compressed temperatures, three different compressed temperatures were selected to compare the results of these methods of controlling the compressed temperature. Results showed very good agreement between the ignition delay measurements obtained while using the 21% O₂/N₂/Ar oxidizer mixtures and the 21% O₂ and 79% N₂. Therefore, the decision was made to proceed using mixtures blended using the gas blending manifold containing 21% O₂ to ensure that the equivalence ratio was known with a higher level of certainty.

To verify that the ignition delay results from the CSU RCM agreed with those published in the literature, the results were compared against data compiled in a comprehensive study by Goldsborough [27] that includes isooctane ignition delay measurements over a wide range of compressed temperatures and pressures from numerous RCMs and shock tubes. Since there is no standardized design for RCM's or shock tubes, the data collected by Goldsborough varied over a wide range of compressed pressures. To compensate for the fact that not all ignition delay data were acquired at the same pressure, Goldsborough normalized all ignition delay results to two pressures, 10 atm and 45 atm, and then created two overall trend lines encompassing results from all facilities [27]. When conducting experiments in the CSU RCM at initial pressures of 1000 mbar, the compressed pressure is approximately 28 bar, which lies almost exactly equidistant between 10 atm and 45 atm. The CSU RCM ignition delay measurements fell between those normalized by Goldsborough to 10 and 45 atm, which indicates that the CSU RCM produces ignition delay measurements that are consistent with the literature.

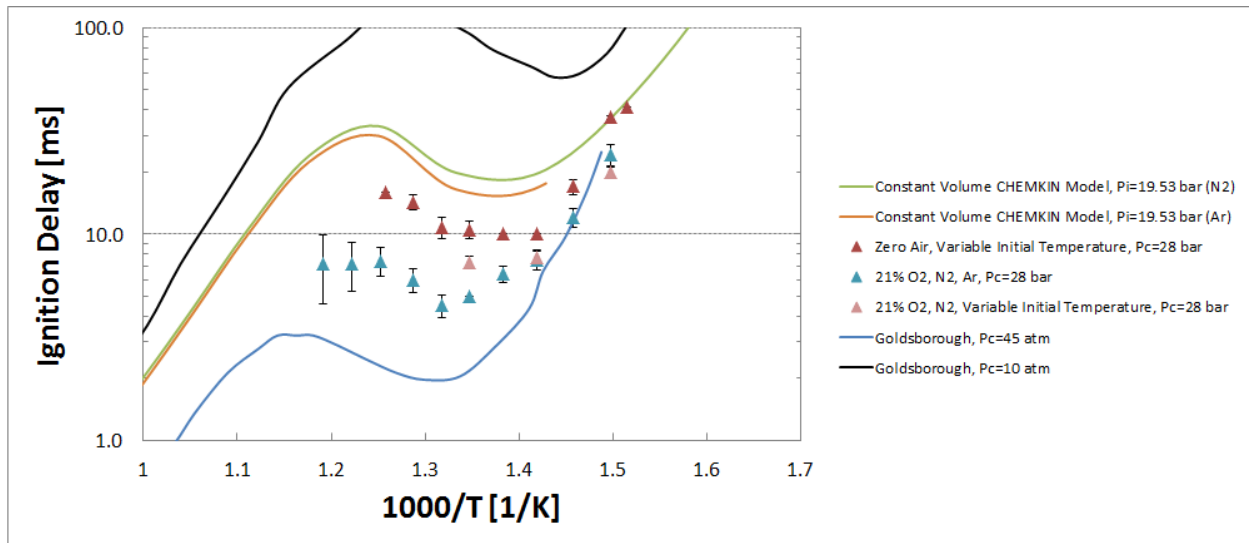


Figure 4.4 Simulated, experimental, and published Isooctane Ignition Delay Curves.

Figure 4.5 is an example pressure vs. time trace from one experimental run conducted in the RCM for a stoichiometric mixture of isooctane, 21% O₂, X% N₂, and Y% Ar at a compressed

pressure of 705 K. It can be observed from the pressure trace that after the maximum compressed pressure is reached there is a short induction period during which the pressure decreases due to heat transfer to the chamber walls after which the pressure increases to the maximum combustion pressure in two stages. The first stage of pressure increase is due to low temperature heat release (LTHR) from chemical reactions between the fuel and oxygen that lead to chain branching at low temperatures. However, the first stage of pressure increase is short lived because, as the temperature of the gas increases, the fuel/oxidizer mixture enters into the negative temperature coefficient (NTC) region within which chain termination reactions dominate and the overall reaction rate slows down. Due to this reduction in chemical reactivity, heat release decreases resulting in a plateauing of the pressure trace. After a secondary induction period, the pressure dramatically increases to the maximum compressed pressure as a result of high temperature heat release due to the development of a radical pool that results in chain branching. The maximum pressure obtained in the experiment shown in Fig. 4.5 due to high temperature heat release is approximately 92 bars. Immediately after reaching the maximum combustion pressure, the pressure trace decreases sharply because the combustion chamber pressure transducer is a non-temperature compensated model. Therefore, the pressure data acquired after the peak pressure (approximately 18 ms in Fig. 4.5) is not accurate.

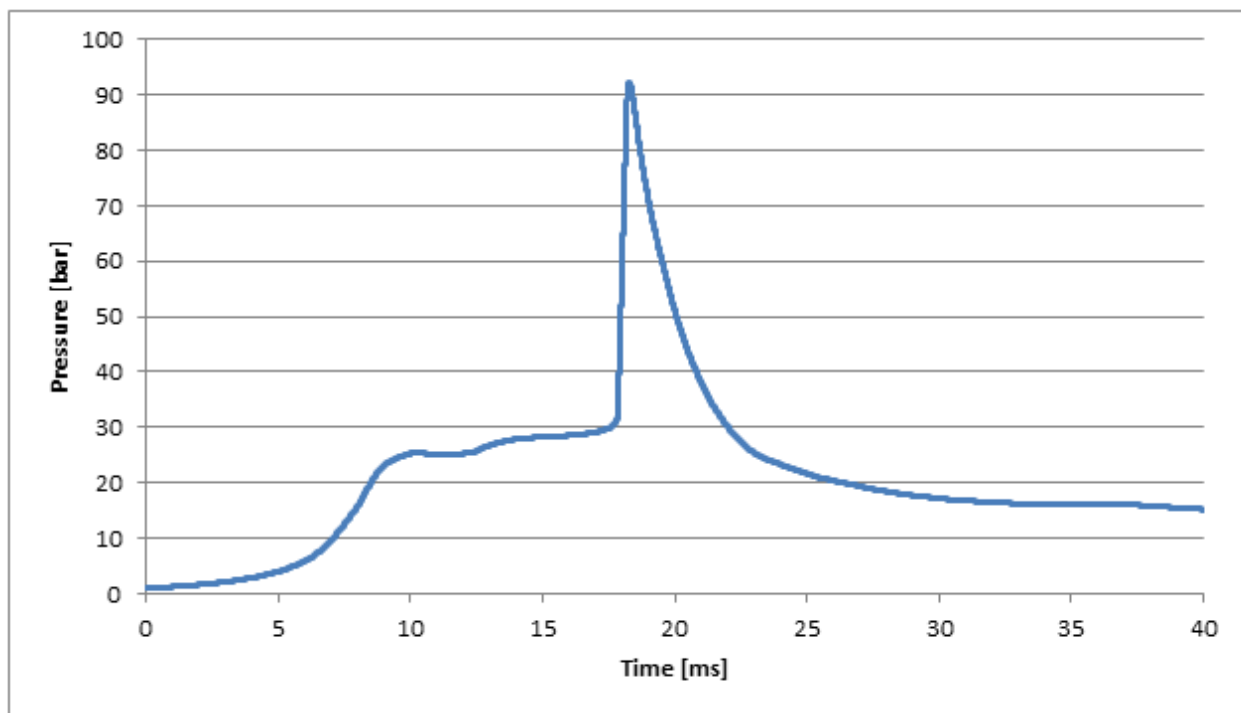


Figure 4.5 Pressure Trace from Experimental Run in the RCM of Stoichiometric isooctane/21%O₂/X%N₂/Y%Ar Mixture at a compressed temperature of 705 K.

After concluding the isooctane testing in the RCM, additional CHEMKIN simulations of stoichiometric isooctane mixtures were conducted using the full RCM volume vs. time data as an input for comparison against the experimental data. Figure 4.6 is the pressure vs. time trace of a CHEMKIN simulation of the auto-ignition of isooctane in the RCM utilizing the full RCM volume trace. When the experimental pressure trace is compared to the CHEMKIN simulated pressure trace, there are similarities where the simulation reproduces experimental observations but there are a few key areas in which the simulation deviates from the experimental results.

The CHEMKIN simulation accurately captures the compressed pressure, heat loss (both after the end of compression and the end of combustion), two stage ignition, and maximum combustion pressure of the gaseous mixture. However, the simulation does not accurately reproduce the measured experimental ignition delay period. The measured ignition delay from the experiment was 6.9 ms, while the CHEMKIN simulation predicted an ignition delay of 33.4

ms. When the data are plotted in Arrhenius format (log of ignition delay vs. $1000/T$), the discrepancy between the measured and predicted ignition delay period are not as apparent. The discrepancy between simulated and experimental ignition delay are reasonably consistent with that found in the literature and are most likely a consequence of inaccuracy of the chemical kinetic mechanism.

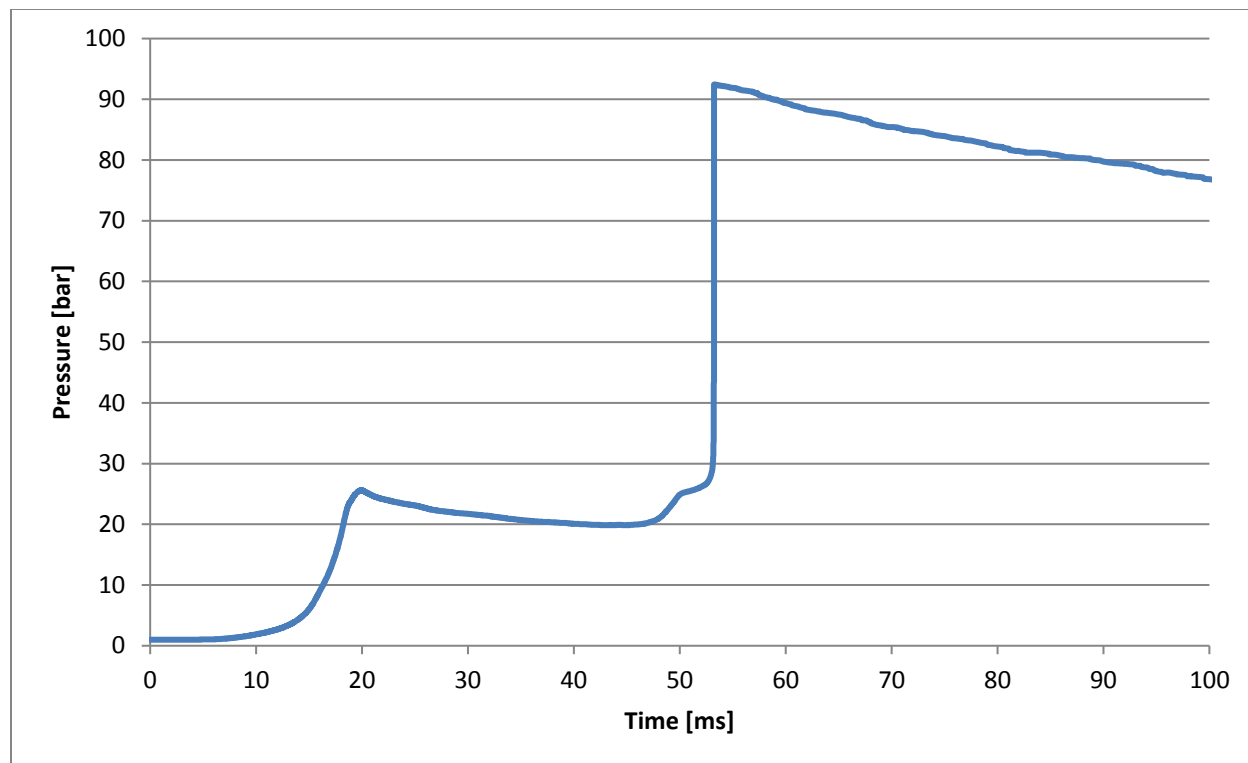


Figure 4.6 Pressure Trace from CHEMKIN Simulation of Stoichiometric Isooctane Mixture at a compressed Pressure of 705 K.

4.3 Toluene Reference Fuel Ignition Delay Testing

Once the experimental isooctane baseline experiments were completed and compared against model predictions and data found in the literature, baseline ignition delay data were acquired for a Toluene Reference Fuel (TRF) blend that would serve as the base fuel for the gasoline additive testing. Real fuels such as gasoline are mixtures of thousands of different hydrocarbon species (e.g., normal alkanes, branched alkanes, aromatics, olefins), making

research into their behavior difficult. In an attempt to standardize gasoline research, surrogate fuels, such as TRF's, are used to simulate real fuels. TRF's are composed of blends of isooctane, n-heptane, and toluene, which represent the three largest classes of hydrocarbons found in gasoline. The ratio of these three species determines the overall reactivity of the mixture. Increasing the content of n-heptane in the TRF blend will increase the overall reactivity of the blend. Conversely, increasing the isooctane and toluene content of the blend will decrease the reactivity of the blend.

Initially, the goal was to determine a TRF blend that would have moderate duration ignition delays - on the order of 50 ms – in the RCM at low temperatures. Moderate duration ignition delays are desirable at low compressed temperatures so that ignition delay periods at higher compressed temperatures are long enough (< 2 ms) to be accurately measured in the RCM. To assist in finalizing the composition of the TRF to be used as the base fuel, CHEMKIN simulations were performed simulate multiple different fuel compositions. Instead of doing a full parametric variation across the range of compressed temperatures, a single set of initial conditions were chosen to run the constant volume simulation at for each of the different TRF mixtures. Table 4.1 summarizes the results of the CHEMKIN ignition delay investigation of different TRFs.

Table 4.1 Stoichiometric toluene reference fuel ignition delay calculations. Constant volume simulations were conducted with initial temperature and pressure of 634 K and 19.53 bar, respectively. Full volume trace simulations were conducted with initial temperature and pressure of 300 K and 1 bar.

Simulation Number	Percent Toluene	Percent Iso-Octane	Percent N-Heptane	Initial Conditions	Ignition Delay
1	30%	50%	20%	Full Volume Trace (FVT)	No Ignition
2	30%	20%	50%	FVT	46 ms

3	30%	20%	50%	Constant Volume (CV)	40.3 ms
4	30%	35%	35%	CV	50 ms
5	30%	45%	25%	CV	61.1 ms
6	30%	50%	20%	CV	85 ms
7	30%	60%	10%	CV	127 ms
8	30%	45%	25%	FVT	No Ignition
9	30%	35%	35%	FVT	No Ignition
10	30%	30%	40%	FVT	120 ms

Simulations performed with the full RCM volume trace had initial temperatures and pressures of 300 K and 1 bar, while simulations performed with the constant volume assumption used initial temperatures and pressures of 634 K and 19.53 bar. For all the simulations, the volume percentage of toluene was held constant at 30% while the percentages of isooctane and n-heptane were varied. Toluene is classified as an aromatic hydrocarbon, so the decision to hold the toluene content constant was to simulate real gasolines, which typically contain approximately 30% aromatic compounds. Ultimately, after performing a number of constant volume and full volume trace simulations the TRF that was selected for use as the baseline fuel in the RCM was 30% toluene, 60% isooctane, 10% n-heptane. The reason this composition of TRF was selected for baseline testing was that it exhibited the longest ignition delay of any of the fuel mixtures simulated.

After the composition of the TRF baseline fuel was selected, ignition delay testing was conducted in the RCM. Equivalence ratios of 1 and 0.75 were tested and their results are plotted in Figure 4.7. Each data point in Fig. 4.7 is the average of three to five measurements, and the

error bars plotted represent the standard deviation of those measurements. CHEMKIN constant volume simulations were also conducted for the TRF blend at both the $\phi=1$ and $\phi=0.75$ over a range of initial temperatures of 500K to 1200K and an initial pressure of 19.53 bar. Simulated results were plotted on Figure 4.7 for comparison against experimental data. Experimental data exhibited excellent agreement with the simulated results at low compressed temperatures, but as temperature increased experimental results exhibited shorter ignition delays than the model predicted. This same behavior was observed in the study of isooctane ignition delays. Although the experimental data deviated from the predicted results of the model, the experimental results of both equivalence ratios exhibited an NTC region like the model had predicted. Also, as expected, the leaner TRF blend proved to be less reactive than the stoichiometric blend and exhibited longer ignition delays.

Another observation worth noting is the apparent increase in error at higher compressed temperatures. This phenomenon has two potential explanations. First, the log scale used on the ignition delay axis exaggerates differences at the very short ignition delays observed at high compressed pressures. Second, as the RCM reaches the lower limit of measurable ignition delays, approximately one to two milliseconds, the percentage variability of results increases.

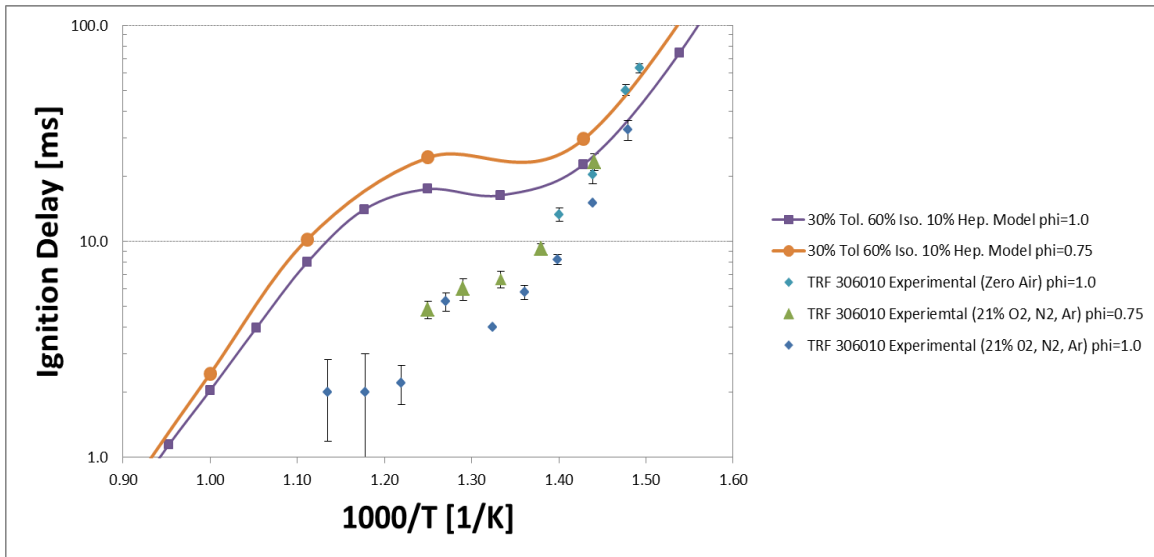


Figure 4.7 Simulated and experimental Toluene Reference Fuel Ignition Delay Curves.

4.4 Gasoline Fuel Additive Testing

For the gasoline additive testing, a small batch of the baseline TRF blend was produced at the sponsors facility. Three separate two-liter fuel containers were shipped to CSU. One of the fuel containers contained baseline fuel without additive, one base fuel combined with 200 ppm Additive 1, and the third base fuel combined with 1000 ppm Additive 1. Due to the proprietary nature of gasoline additive research, the chemical formulas of the gasoline additives are not included herein and are referred to as Additive 1, 2 and 3, respectively.

Upon receiving the fuel shipment from the sponsor the baseline fuel was tested in the RCM and compared to the previous baseline results before proceeding to Additive 1 testing. Results showed that the sponsor blended base fuel exhibited slightly different ignition delay behavior in comparison to the TRF blends produced at CSU. Although the difference between the previously compiled baseline ignition delay curve and the sponsor fuel baseline ignition delay curve was minimal, that the decision was made to use the sponsor fuel baseline curve for comparison with the additive blends. It would be impossible to detect the performance of extremely low additive concentrations without using the sponsor fuel baseline. The baseline

ignition delay experiments were repeated using the sponsor provided baseline fuel with initial conditions of $\phi=1$ and initial pressures of 1000 mbar and 850 mbar in the RCM. The guidance of the sponsor guided the decision to form a baseline curve for a stoichiometric Toluene Reference Fuel mixture at an initial pressure of 850 instead of investigating a lean mixture as before. This decision was made due to the fact that gasoline engines are almost always operated at stoichiometric conditions, but not always at sea level pressures.

After completing the new baseline ignition delay measurements, Additive 1 was tested in the RCM. The conditions that Additive 1 was tested under were 200 ppm and 1000 ppm concentrations, initial pressures of 850 and 1000 mbar, initial temperature of 300 K, and compressed temperatures ranging from 675 K to 800 K. The compressed temperature was varied by varying the Ar to N₂ ratio, which resulted in variation of the γ of the mixture. Figure 4.8 displays the results of Additive 1 testing. The ignition delay results of testing Additive 1 are plotted on a log scale of Ignition Delay vs. $1000/T$. Also plotted for comparison on Figure 4.3 are constant volume CHEMKIN simulations for initial pressure of 850 and 1000 mbar, and the results of the sponsor baseline fuel ignition testing in the RCM.

Comparing the ignition delay results of the base fuel against the base fuel plus Additive 1 yields two main observations. First, the addition of Additive 1 increases the overall reactivity of the base fuel and decreases ignition delay periods across the full temperature range. Second, Additive 1 displays a saturation characteristic. The performance of Additive 1 at 200 ppm is almost identical to the performance of the 1000 ppm concentration. One explanation for this effect is that Additive 1 is so reactive that a very low concentration is able to initiate the combustion process of the base fuel present. Another explanation is that both 200 ppm and 1000

ppm, 0.02% and 0.1% respectively, are simply too low of concentrations to fully observe the effect that Additive 1 has on the ignition delay of the base fuel.

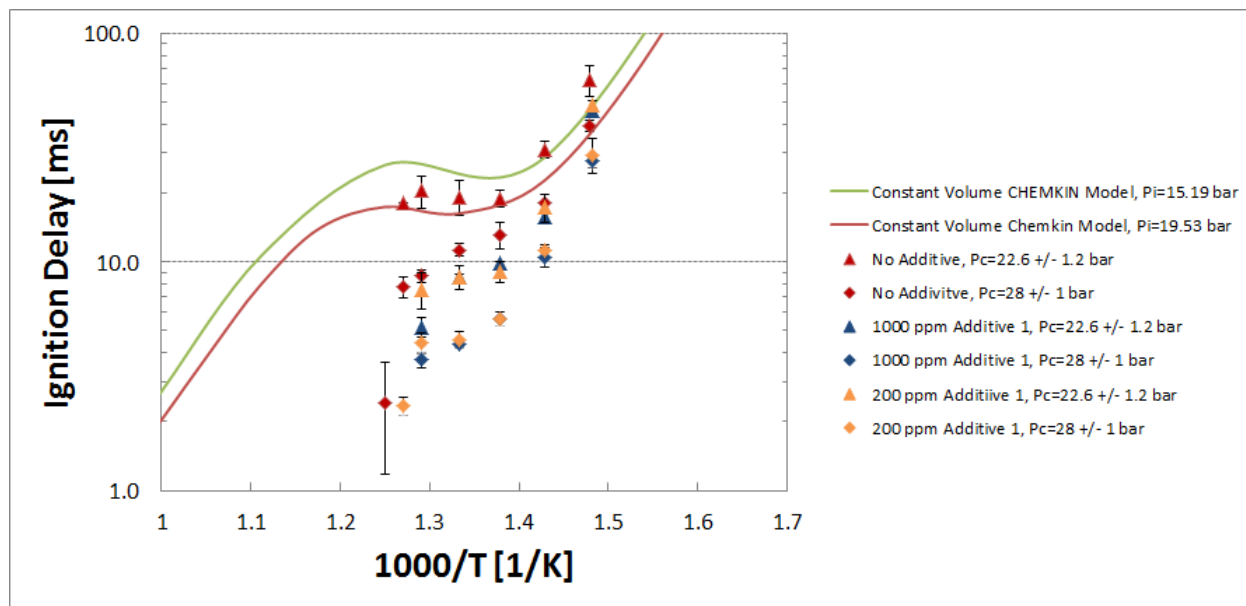


Figure 4.8 Additive 1 in TRF Base Fuel Ignition Delay Curves.

After reporting the performance of Additive 1 to the sponsor the decision was made to forgo further testing of Additive 1 at lower equivalence ratio, and instead transition to testing Additive 2 in the RCM. Additive 2 was mixed with the base fuel in Richmond, California and shipped to CSU. The sponsor sent Additive 2 in concentrations of 200 ppm and 1000 ppm blended with base fuel, similar to Additive 1. The decision was made to first test Additive 2 at an initial pressure of 1000 mbar and then compare to the performance of Additive 1. Figure 4.9 illustrates the performance of both concentrations of Additive 2, along with the baseline and CHEMKIN simulation results for comparison.

Comparison of the performance of Additive 2 and the baseline yielded two observations. First, Additive 2 appeared to increase the reactivity of the base fuel (similar to observations for Additive 1) and decrease ignition delays compared to the baseline. Second, the increase in Additive 2 concentration from 200 ppm to 1000 ppm resulted in a quantifiable decrease in

ignition delays across the entire compressed temperature range except for one point. At the highest compressed temperature investigated, 775 K, the ignition delay of 200 ppm was shorter than the ignition delay of 1000 ppm. However, the 200 ppm data point and the 1000 data point fall within the uncertainty. The simplest explanation for this observation is that, at extremely short ignition delays, 200 ppm and 1000 ppm of Additive 2 exhibit the same performance.

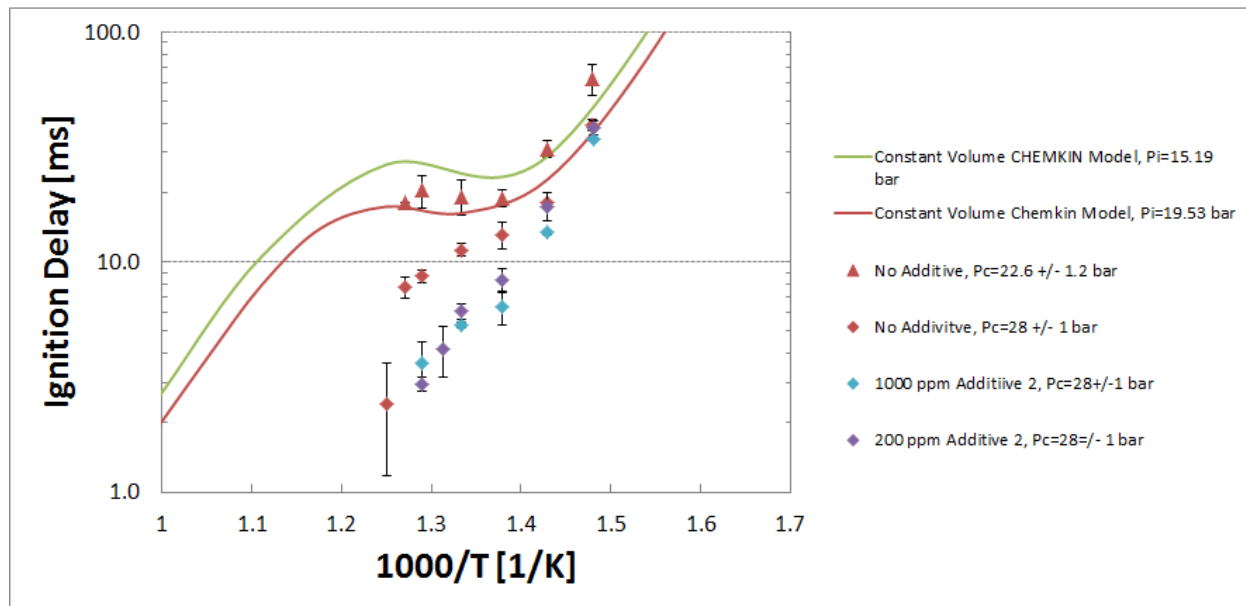


Figure 4.9 Additive 2 in TRF Base Fuel Ignition Delay Curves.

Figure 4.10 displays the ignition delay results of Additive 1 and 2 at an initial pressure of 1000 mbar plotted against the baseline for comparison. From Figure 4.10 it is clear that both Additive 1 and 2 increase the reactivity of the base fuel and decrease the ignition delay. It is also clear that Additive 1 has a stronger effect on the ignition delay of the TRF blend than Additive 2. Because of these findings, the decision was made to forgo testing Additive 2 at the reduced initial pressure of 850 mbar. Instead the decision was made to transition to testing additives in a new base fuel to be able to observe the difference in additive performance in different base fuels. Isooctane was selected as the new base fuel for additive testing for two reasons. First, in the RCM community, isooctane is considered the benchmark for ignition delay testing [reference

Goldsborough]. Second, isooctane is significantly less likely to generate soot during combustion than the TRF fuel, because the aromatic compound Toluene is known to produce more soot than alkanes such as isooctane [51] [52] [53].

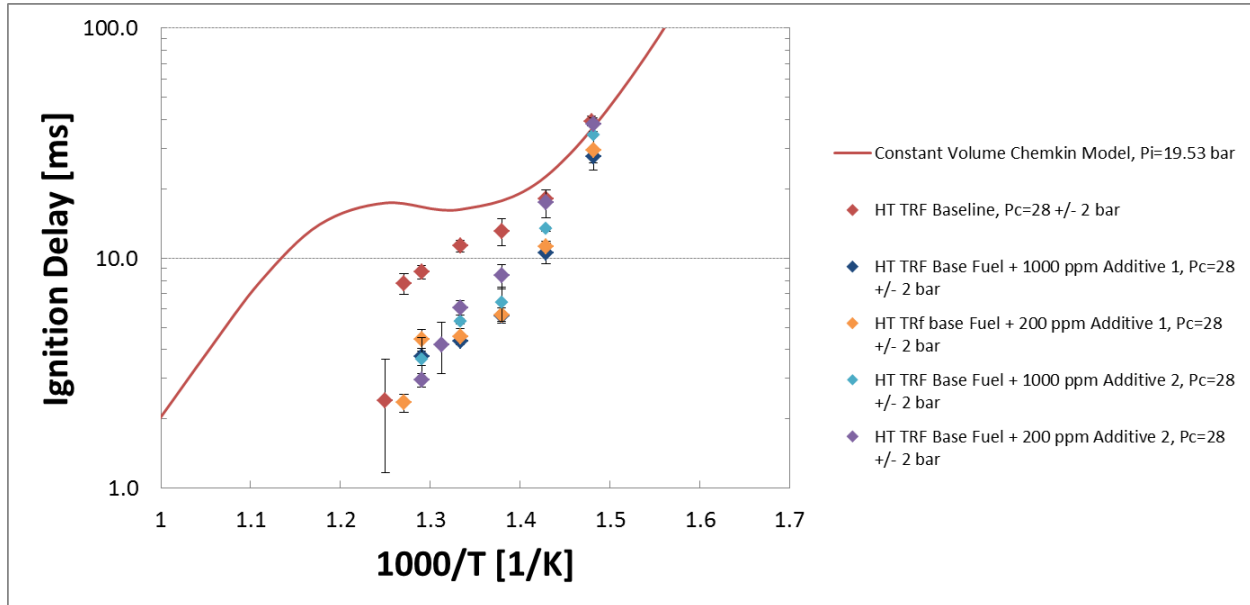


Figure 4.10 Comparison of Additive 1 and Additive 2 Performance in TRF Base Fuel.

A major difficulty that was encountered during the testing of Additive 1 and 2 when blended with the TRF was that the combustion chamber valve tip melted after experiments that resulted in ignition. Due to this difficulty, it became tediously slow to collect ignition delay data because of the time required to change the combustion chamber valve tip between each test, as well as the time required to machine replacement valve tips out of PEEK. The initial hypothesis to explain this phenomenon was that the combustion of the TRF base fuel was generating soot, which was coating the valve tip and melting the PEEK. However, this initial theory was later proven incorrect when it was discovered that the valve seat that the combustion chamber valve tip sealed against had become warped. The combustion chamber valve seat was purposefully machined to be very thin, approximately 0.05 in, to reduce the combustion chamber dead volume when the pistons were at top dead center. However, due to the thickness of the valve seat it was

susceptible to being warped by the valve tip repeatedly being forced against it all the while being repeatedly rapidly heated and cooled. The thin nature of the valve seat presented a challenge to solve because it was impossible to press back into place without breaking the valve seat.

After exploring different solutions, the solution that was finally settled upon was to replace the existing needle type valve with a new ball type valve that did not utilize the warped valve seat to seal the combustion chamber. However, the replacement of the combustion chamber valve created a new problem, an increase in combustion chamber dead volume. Now, due to the design of the new combustion chamber valve, the compressed temperature and pressure of the gases inside the combustion chamber would be reduced at all the previous tested temperatures due to the reduction in the compression ratio of the RCM. To rectify this problem, an increase in initial temperature and pressure was required to achieve the same compressed temperature and pressure as with the original valve. The initial temperature needed to be increased 4 K to 304 K, and the initial pressure needed to be increased by 54 mbar to 1054 mbar. To verify that these changes in initial conditions did in fact result in achieving the desired compressed conditions, the ignition delay performance of pure isooctane was checked against the previously established baseline. Good agreement was observed when comparing the isooctane testing with the new valve against the previous baseline; therefore the transition was made to additive testing in isooctane base fuel.

The 1000 ppm concentration of Additive 2 was selected to be the first additive to be tested in the isooctane base fuel. The decision to begin additive testing in Iso-Octane with Additive 2 was made because Additive 1 was not soluble in isooctane in concentrations high enough to test. The results of the Additive 2 ignition delay testing in isooctane are presented below in Figure 4.11. Also plotted for comparison in Figure 4.11 are the isooctane ignition delay base line and

the CHEMKIN model results utilizing the Mehl mechanism [49]. Thanks to the help of Siddhesh Bhoite, new Chemkin 0-D model results were obtained that much more closely reproduce the experimental RCM conditions. By varying the ratio of N₂ to Ar in the model to change the compressed conditions, significantly closer agreement was achieved between experimental and model results.

The ignition delay testing of Additive 2 in the isooctane base fuel yielded unique results when compared with the previous testing of Additive 2. When Additive 2 was tested in the TRF base fuel, the additive increased the reactivity and shortened ignition delays at all compressed temperatures. However, when Additive 2 was blended with isooctane the opposite results were observed. Instead of increasing the reactivity of the base fuel at all the compressed temperatures that were investigated, Additive 2 decreased the reactivity of the isooctane base fuel and increased the ignition delay at almost every compressed temperature investigated. One theory for this reversal in performance is that depending on which base fuel Additive 2 is blended with, the compressed temperatures tested may fall in different regions of the explosion limits, which would cause the base fuels to behave differently and potentially be affected differently by the same additive.

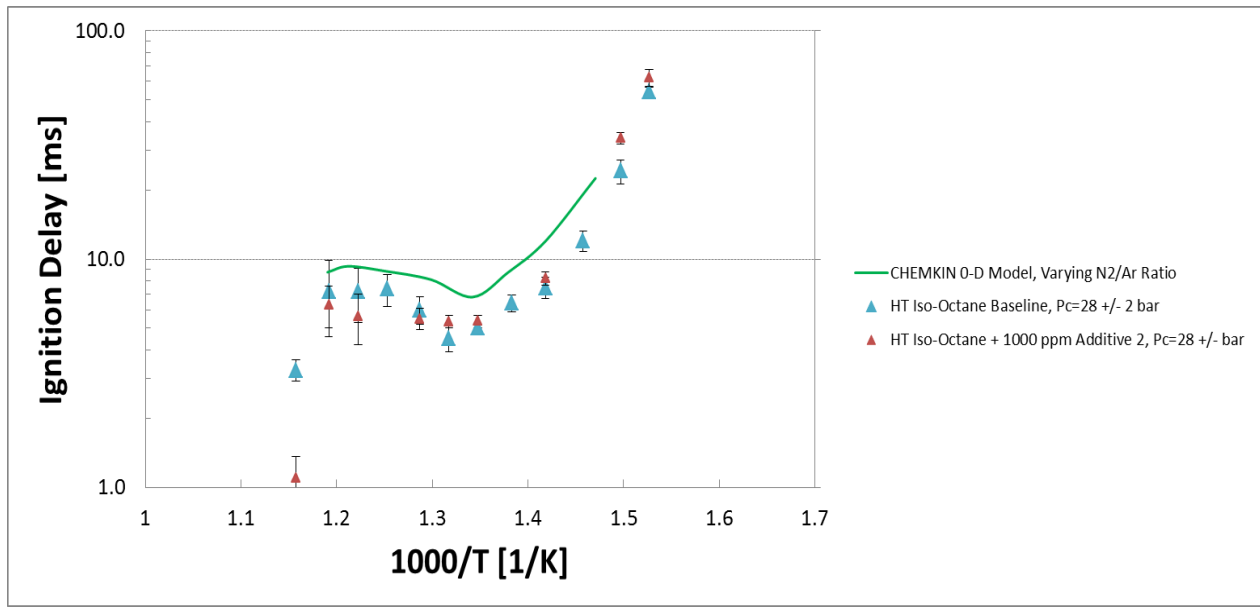


Figure 4.11 Additive 2 in Isooctane Base Fuel Ignition Delay Curve.

After presenting the results of the Additive 2 ignition delay, the sponsors of this research directed the next phase of testing towards a new additive that had shown considerable promise in their internal testing. The results of the ignition delay testing of Additive 3 in isooctane are presented below in Figure 4.12 along with the isooctane baseline and CHEMKIN model results for comparison. Similar to the behavior of Additives 1 and 2 when blended with the TRF base fuel, Additive 3 decreased the ignition delays of the isooctane base fuel at all of the compressed temperatures tested.

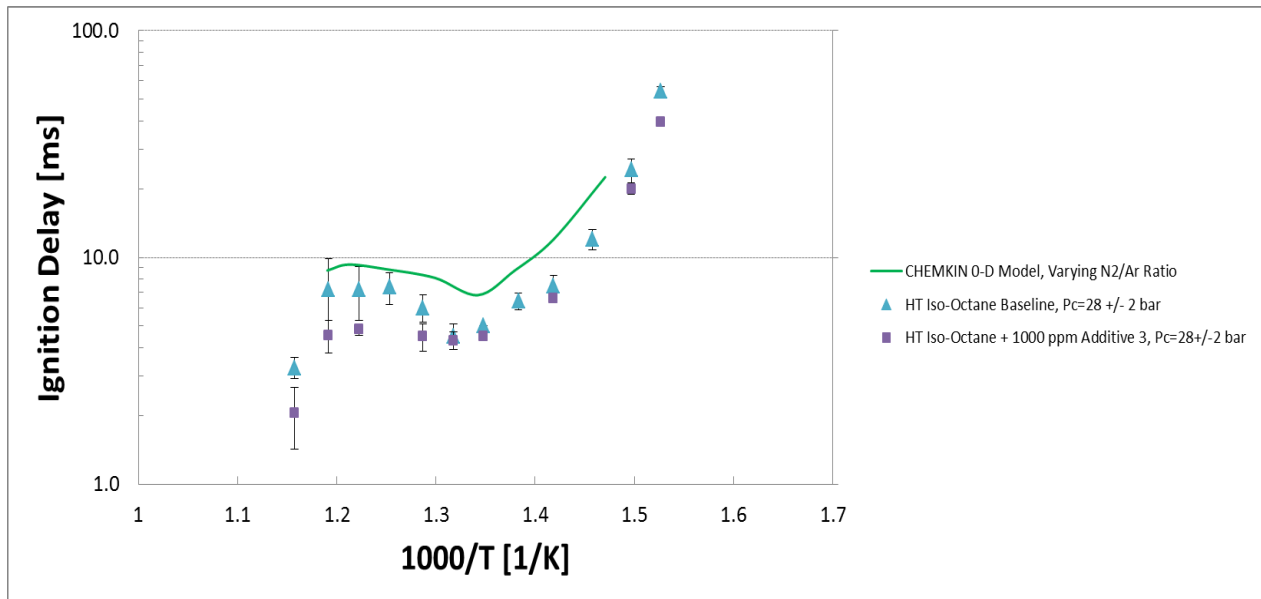


Figure 4.12 Additive 3 in Isooctane Base Fuel Ignition Delay Curve.

Next, a radical scavenger called Diphenyl Amine was blended with isooctane and shipped to CSU. Before testing, it was hypothesized that the addition of the Diphenyl Amine would reduce the reactivity of the isooctane by reacting with the initial radicals produced during the combustion process, thereby slowing the combustion process and resulting in increased duration ignition delays. However, after concluding testing in the RCM, it became evident that in the pressure and temperature regime that the RCM operates within, the Diphenyl Amine was actually increasing the reactivity of the isooctane. Figure 4.13 presents the results of the Diphenyl Amine testing.

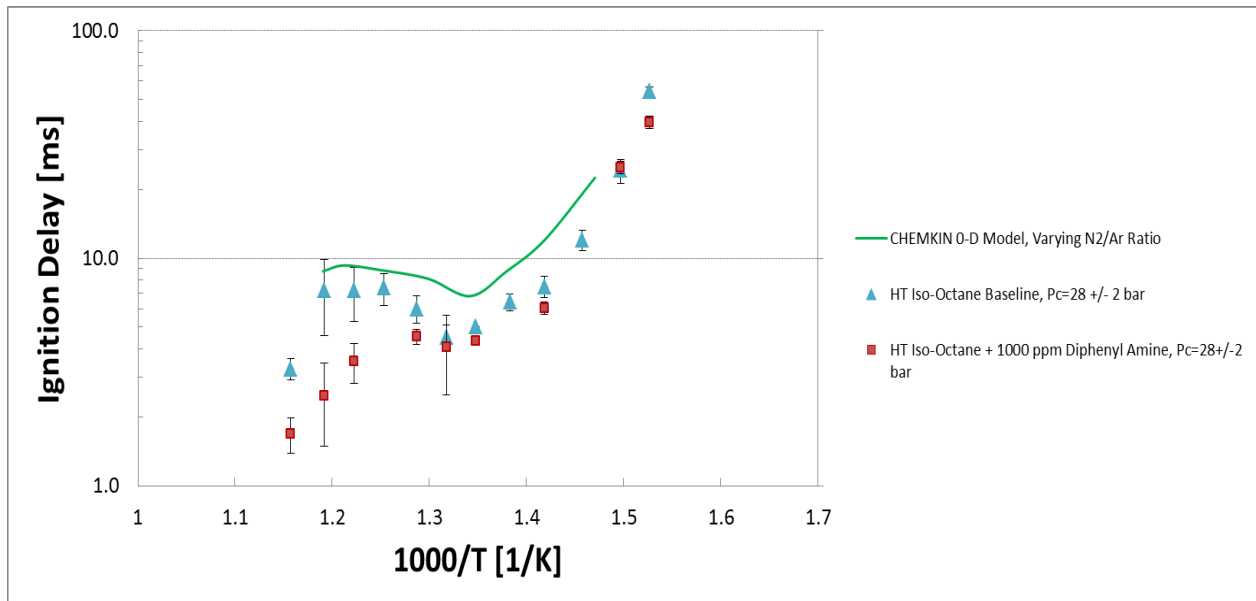


Figure 4.13 Diphenyl Amine in Isooctane Base Fuel Ignition Delay Curve.

The additive MoDTC was also tested in the RCM at the directing of the sponsor. Normally, MoDTC is used as a friction reduction additive in engine oils [54] [55] [56] [57] [58]. However, the sponsor of this research has hypothesized that small concentrations of MoDTC could be responsible for causing Super Knock in spark ignited internal combustion engines. Under this hypothesis, small amounts of engine oil containing the additive MoDTC find their way into the combustion chamber due to blow by between the piston and cylinder wall, and these trace amounts of MoDTC are the initiator for abnormal combustion events such as Super Knock. Therefore, the sponsor was interested in the auto ignition characteristics of MoDTC to see if it did in fact alter the combustion characteristic of gasoline surrogate fuels. Figure 4.14 presents the results of the ignition delay testing of MoDTC, along with baseline and model results for comparison. At almost every compressed temperature tested, with the exception of the second and third to hottest compressed temperatures, the MoDTC had very negligible effect on the ignition delay characteristics of isooctane. Therefore, it can be concluded that it is unlikely that MoDTC is responsible for initiating abnormal combustion events such as Super Knock.

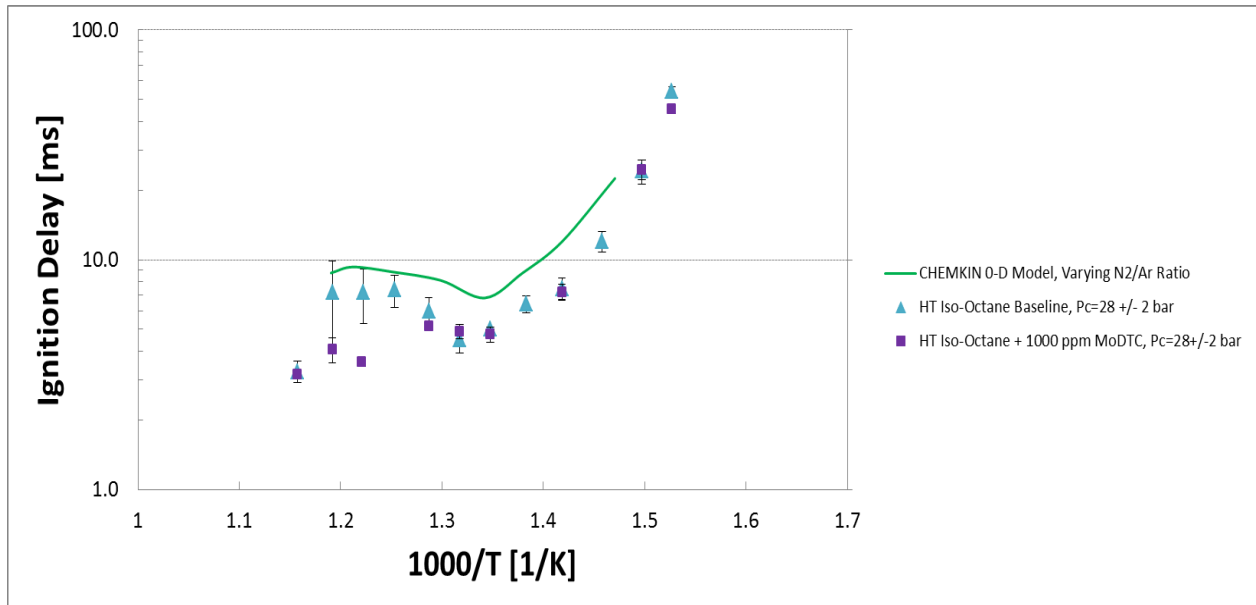


Figure 4.14 MoDTC in Isooctane Base Fuel Ignition Delay Curve.

To determine the process by which some additives affected ignition delay periods, a heat release analysis was performed to determine the effect of the additives on low temperature and high temperature heat release. The decision was made to analyze the isooctane baseline and the isooctane + additive data first, and then move on to analyzing the TRF baseline and TRF + additive data in the hopes of discovering a correlation between heat release and ignition delay.

Using a modified version of a heat release rate model previously developed by Dumitrache, et al [59] for the laser ignition research, the pressure vs. time data was analyzed for instantaneous rate of heat release and net integrated heat release in the combustion chamber. The heat release rate model proved only accurate when analyzing combustion events with ignition delays longer than 10 ms. Although the higher compressed temperature combustion was not able to be analyzed, data that was able to be analyzed resulted in valuable observations.

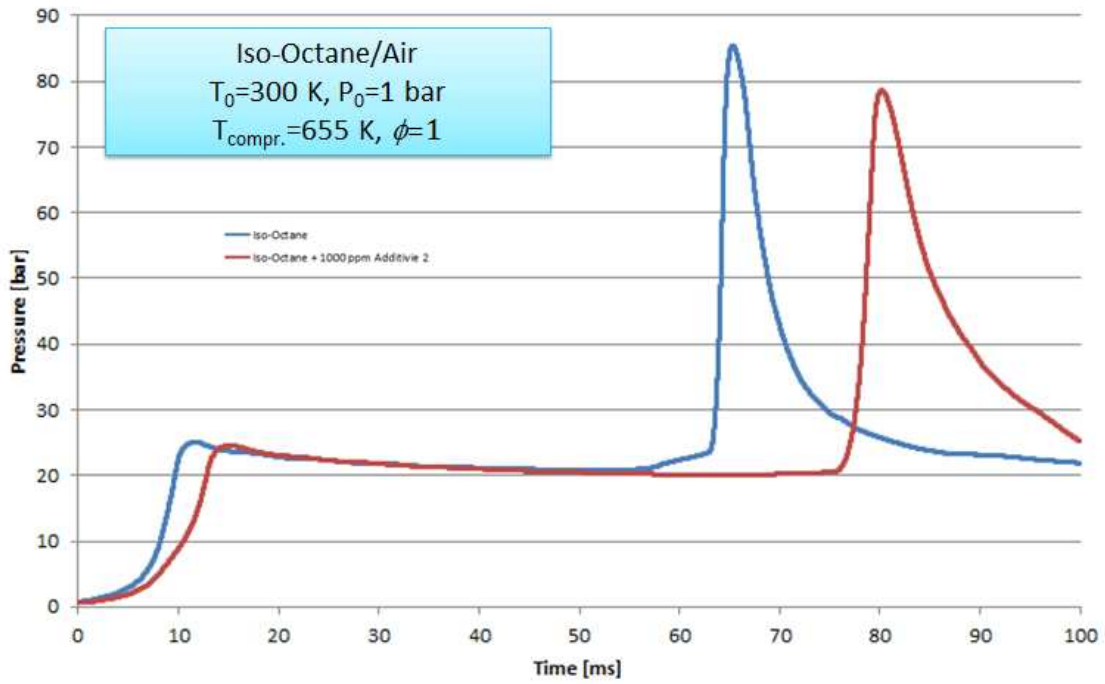


Figure 4.15 Isooctane and Isooctane + 1000 ppm Additive 2 Pressure vs. Time.

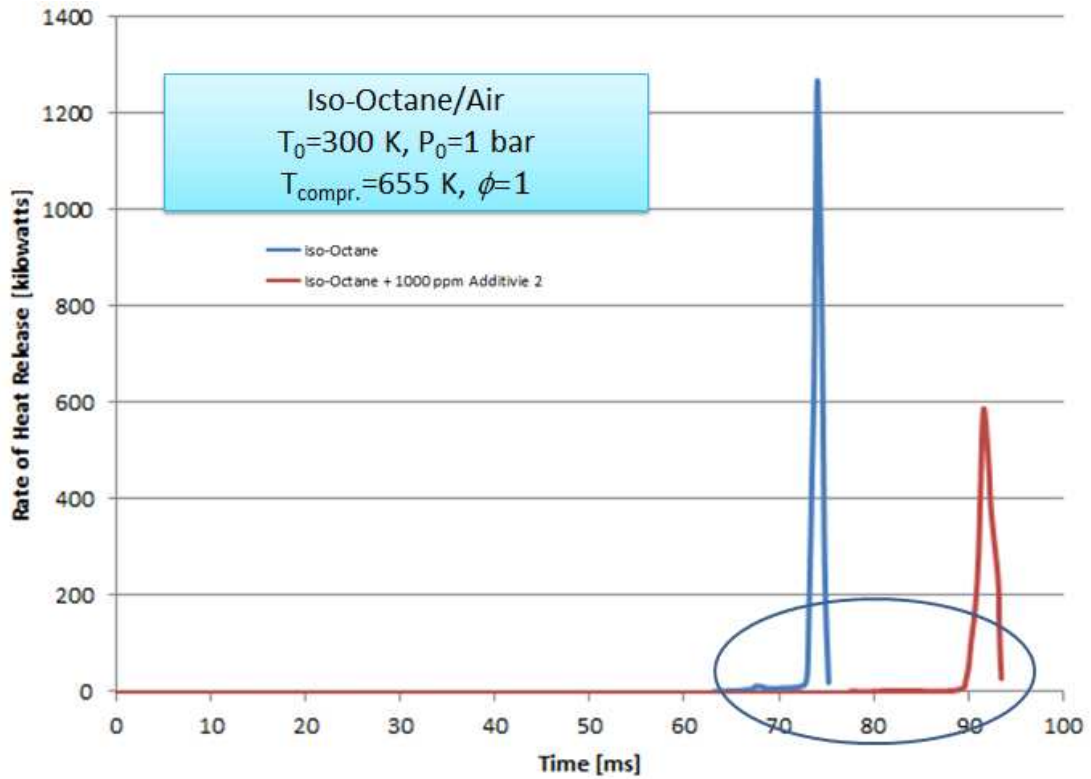


Figure 4.16 Isooctane and Isooctane + 1000 ppm Additive 2 Instantaneous Rate of Heat Release.

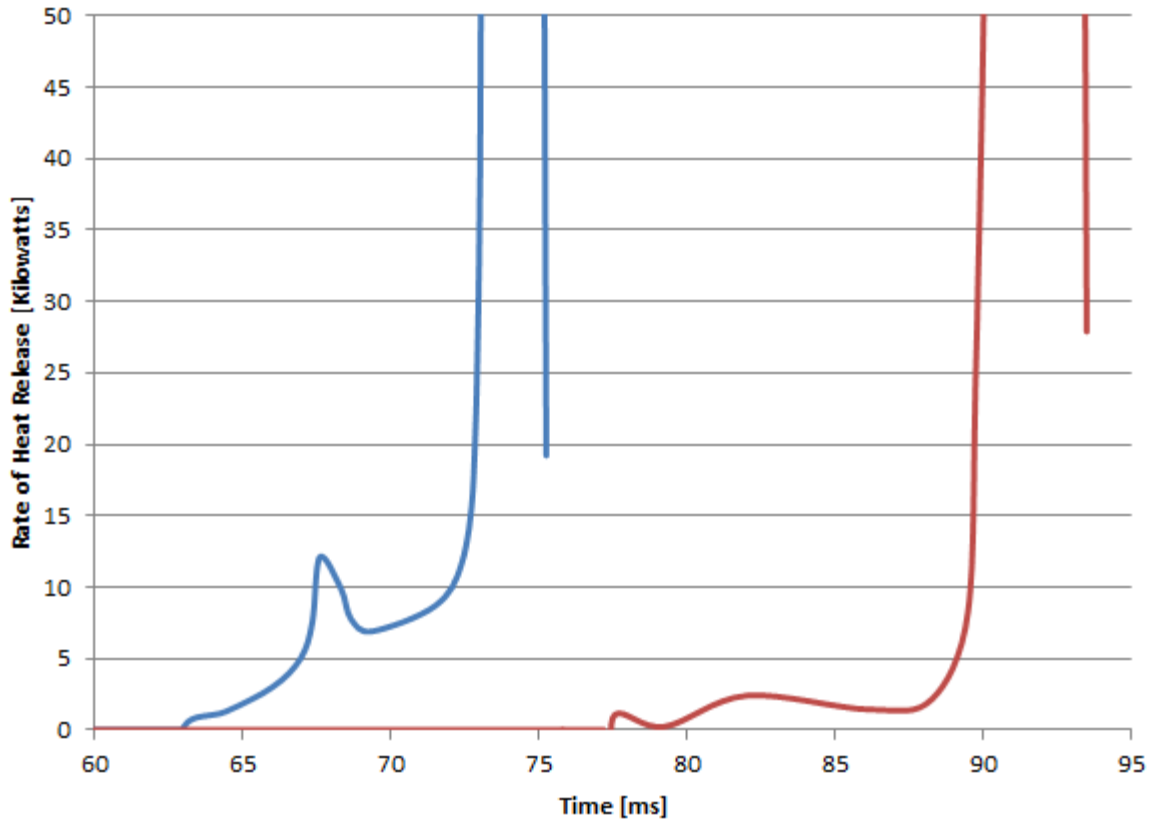


Figure 4.17 Isooctane and isooctane + 1000 ppm Additive 2 Low Temperature Heat Release.

Figure 4.15 illustrates the effect of the addition of 1000 ppm Additive 2 on the isooctane pressure vs. time curve. The increase in ignition delay due to the addition of Additive 2 is immediately obvious. However, perhaps less obvious is the decrease in low temperature heat release due to the addition of Additive 2. Looking closely at the pressure traces, it can be seen that the isooctane/additive blend (red line) did not exhibit two stage ignition behavior, which is in contrast to the pure isooctane case (blue curve) that exhibited a pressure increase prior to the high main ignition event. To better quantify the reduction in low temperature heat release observed with the addition of Additive 2, the pressure and volume data from the RCM were input into the heat release model to calculate the instantaneous rate of heat release for isooctane and isooctane + 1000 ppm Additive 2. Figure 4.16 displays the calculated instantaneous rate of

heat release for isooctane and isooctane + 1000 ppm Additive 2 for the entire time history from these experiments. Figure 4.17 displays an exploded view of the low temperature portion of the instantaneous heat release. It can be observed from Figure 4.17 that the addition of Additive 2 decreased the amount of low temperature heat release in comparison to the base isooctane case.

It is hypothesized that this reduction in low temperature heat release is responsible for the increase in the ignition delay for the isooctane/Additive 2 blend in comparison to the baseline isooctane case. Low temperature heat release results in temperature rise during the chemical induction period (as evidenced by the pressure rise in the experiments), which reduces the induction period for the main high temperature ignition event.

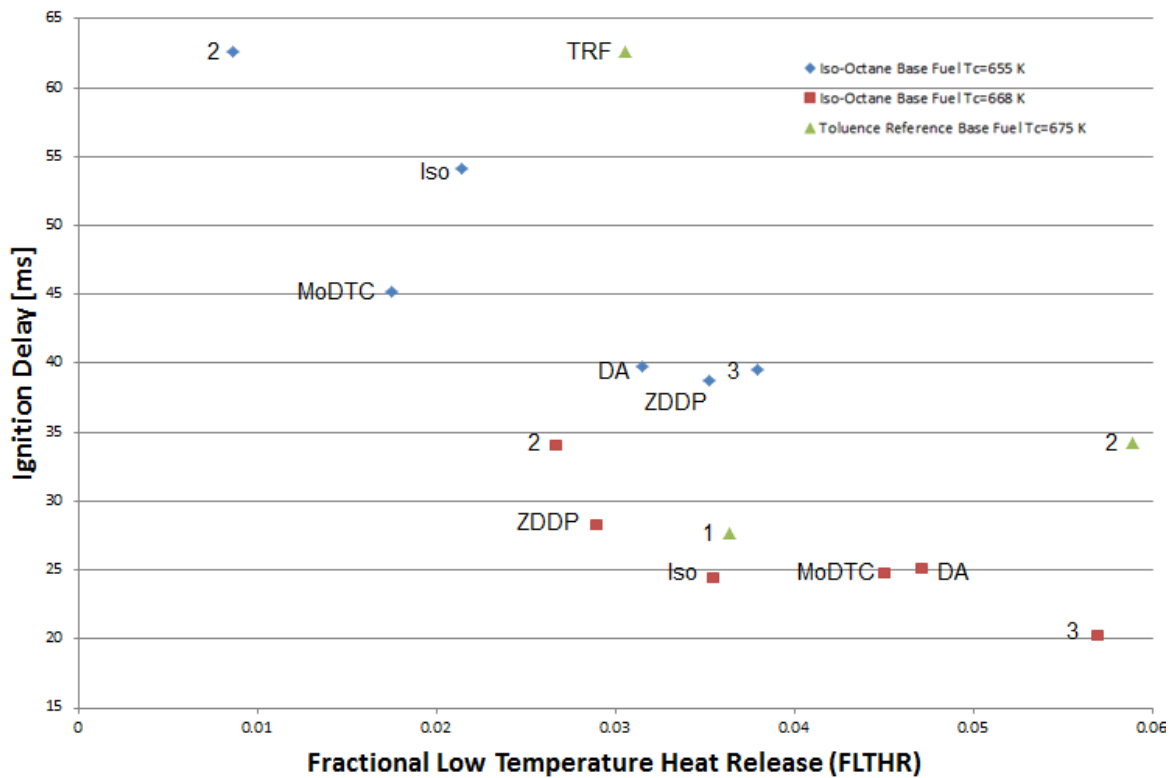


Figure 4.18 Fractional Low Temperature Heat Release vs. Ignition Delay.

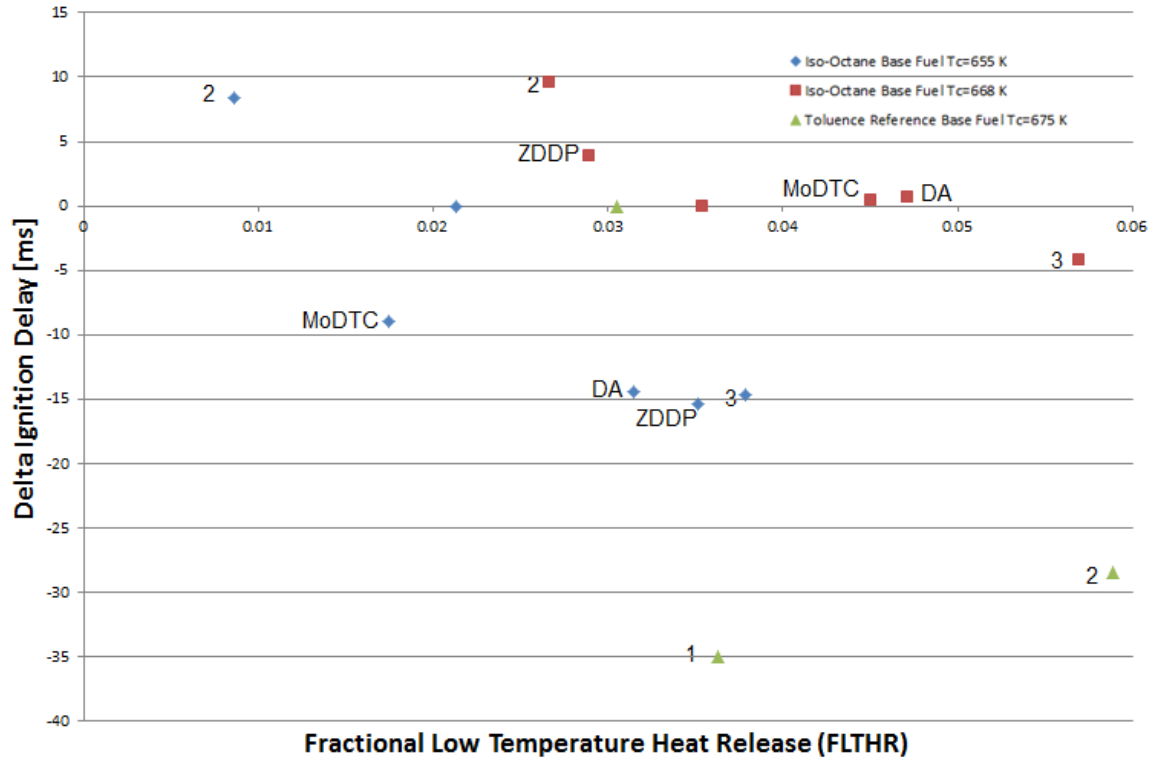


Figure 4.19 Fractional Low Temperature Heat Release vs. Delta Ignition Delay.

The heat release analysis of the isooctane base line data revealed distinct low and high temperature heat release events. However, when the 1000 ppm Additive 2 cases were analyzed it became clear that there was a marked decrease in the amount of low temperature heat release. Figures 4.18 and 4.19 illustrate the relationship between ignition delays and fractional low temperature heat release. To calculate the fractional low temperature heat release (FLTHR), first the time when combustion transition between low temperature heat release and high temperature heat release is noted from the instantaneous rate of heat release graph. In Figure 4.17, the isooctane base fuel (blue curve) transitions from low temperature heat release to high temperature heat release at approximately 69 ms. Next, the amount of net heat release at this transition time is divided by the final net heat release and multiplied by 100% to obtain the value of fractional low temperature heat release. The FLTHR are plotted versus corresponding ignition delays in Figure 4.18, and the FLTHR are plotted versus Δ ignition delays in Figure 4.19.

At the compressed temperature of 655 K, the FLHR for the isooctane base fuel was 9.0% +/- 0.8%, compared to only 5.7% +/- 1.4% when 1000 ppm Additive 2 was blended with the isooctane base fuel. The decrease in low temperature heat release is believed to be the reason that Additive 2 increases the ignition delays of the isooctane base fuel.

5 CONCLUSIONS AND FUTURE WORK

A study of the effects of fuel additives on laser ignition and auto-ignition is reported. The primary motivation for this study was to examine the combustion of natural gas and gasoline type fuels at elevated temperatures and pressures such as those experienced in internal combustion engines. To this end, the Colorado State University Rapid Compression Machine was employed to repeatedly adiabatically and homogeneously compress fuel/oxidizer mixtures.

Methane/Air mixtures from stoichiometric conditions to $\phi=0.25$ were ignited in the RCM using a Nd:YAG pulsed laser ($\lambda=1064$ nm and pulse duration 12 ns). The minimum spark energy, minimum ignition energy, heat release, and lean limit of pure methane/air mixtures were measured. This data was compared to data published in the literature, and used as a baseline for comparison to methane fuel additive performance. Testing of methane/air mixtures yielded a lean limit $\phi_{MIN90}=0.47$ and a minimum ignition energy $MIE_{90}=7.2$ mJ, both values are lower than those reported in the literature. At the highest concentrations tested addition of methane fuel additives (1,1-Di (tert-butylperoxy), Nitromethane, and Dimethoxymethane) resulted in lean limit ϕ_{MIN90} of 0.43, 0.36, and 0.53 and MIE_{90} of 4.6 mJ, 2.3 mJ, and 2.3 mJ respectively.

Gasoline is a complex fuel requiring the use of fuel surrogates to repeatedly emulate its performance. During this study isooctane, n-heptane, and toluene were used to mimic gasoline. Pure isooctane was utilized to validate the performance of the CSU RCM against results published in the literature, and as a base fuel for additive testing. Using CHEMKIN a custom toluene reference fuel mixture was developed to serve as a second base fuel for gasoline additive testing at elevated temperatures and pressures inside the RCM. Baseline ignition delay curve was established for both the isooctane and TRF base fuels to be compared to additive

results. Five different gasoline additives specified by the study sponsor were tested in the RCM and their effect on the ignition delay of the base fuel was observed. Experiments were conducted to determine the ignition delay, heat release rate, and net heat release of the gasoline surrogate/air mixtures with and without fuel additives. Results show that the majority of the additives increased the reactivity and decreased the ignition delays of the base fuels. However, Additive 2 in the isooctane base fuel was found to decrease the reactivity and increased the ignition delays of the base fuel at select conditions.

Future research will concentrate on three separate areas: High Speed Schlieren Imaging, New Gasoline Fuel Additives, and CFD Modeling. Using the previously developed High Speed Schlieren Imaging setup, a comprehensive study of the laser ignition and auto-ignition of natural gas and gasoline type fuels will be conducted inside the RCM. This study will hope to shed light on how spark kernel formation affects combustion, and how flame propagation inside the combustion chamber relates to perceived heat release and perceived ignition delays. Recent research has focused on the cause of the phenomena Super Knock in small displacement turbocharged direct injection spark ignited engines. One popular theory for the cause of Super Knock is that small amounts of engine lubrication oil are entering the combustion chamber because of blow by and then auto-igniting during compression. However, currently no ignition delay data exists for engine lubrication oil, or the different lubrication additives currently used. The RCM could generate high quality ignition delay data for engine oil and lubrication additives advancing the study of Super Knock. Finally, the compression and combustion processes in the RCM are in the process of being modeled using the CFD software CONVERGE. The aim with this project is to provide a better theoretical understanding of auto-ignition and laser ignition

processes resulting in combustion inside the RCM. The modeled results will be compared to the High Speed Schlieren Images of actual combustion processes in the RCM.

6 BIBLIOGRAPHY

- [1] U.S. Department of Energy, "Quadrennial Technology Review 2015 Internal Combustion Engines Chapter 8: Technology Assessments," U.S. Department of Energy, 2015.
- [2] M. S. Bak, S.-K. Im and M. A. Cappelli, "Successive laser-induced breakdowns in atmospheric pressure air and premixed ethane–air mixtures," *Combustion and Flame*, vol. 161, pp. 1744-1751, 2014.
- [3] J.-L. Beduneau, B. Kim, L. Zimmer and Y. Ikeda, "Measurements of minimum ignition energy in premixed laminar methane/air flow by using laser induced spark," *Combustion and Flame*, vol. 132, pp. 653-665, 2002.
- [4] D. Bradley, C. Sheppard, I. Suardjaja and R. Woolley, "Fundamentals of high-energy spark ignition with lasers," *Combustion and Flame*, vol. 138, pp. 55-77, 2004.
- [5] H. Kopecek, S. Charareh, M. Lackner, C. Forsich, F. Winter, J. Klausner, G. Herdin, M. Winrotter and E. Wintner, "Laser Ignition of Methane-Air Mixtures at High Pressures and Diagnostics," *Journal of Engineering for Gas Turbines and Power*, vol. 127, pp. 213-219, 2005.
- [6] T. Phouc, "Laser spark ignition: experimental determination of laser-induced breakdown thresholds of combustion gases," *Optics Communications*, pp. 419-423, 2000.
- [7] T. X. Phuoc and F. P. White, "Laser-Induced Spark Ignition of CH₄ /Air Mixtures," *Combustion and Flame*, vol. 199, pp. 203-216, 1999.
- [8] P. D. Ronney, "Laser versus conventional ignition of flames," *Optical Engineering*, vol. 33,

- no. 2, pp. 510-521, 1994.
- [9] C. Strozzi, P. Gillard and J.-P. Minard, "Laser-Induced Spark Ignition of Gaseous and Quiescent N-Decane– Air Mixtures," *Combustion Science and Technology*, vol. 186, pp. 1562-1581, 2014.
- [10] M. Weinrotter, H. Kopecek, M. Tesch, E. Wintner, M. Lackner and F. Winter, "Laser ignition of ultra-lean methane/hydrogen/air mixtures at high temperature and pressure," *Experimental Thermal and Fluid Sciences*, vol. 29, pp. 569-577, 2005.
- [11] S. O. Akansu, Z. Dulger, N. Kahraman and T. N. Veziroglu, "Internal combustion engines fueled by natural gas—hydrogen mixtures," *International Journal of Hydrogen Energy*, vol. 29, pp. 1527-1539, 2004.
- [12] P. Geng and H. Zhang, "Combustion and emission characteristics of a direct-injection gasoline engine using the MMT fuel additive gasoline," *Fuel*, vol. 144, pp. 380-387, 2015.
- [13] B. Nagalingam, F. Duebel and K. Schmillen, "PERFORMANCE STUDY USING NATURAL GAS, HYDROGEN- SUPPLEMENTED NATURAL GAS AND HYDROGEN IN AVL RESEARCH ENGINE," *International Journal of Hydrogen Energy*, vol. 8, no. 9, pp. 715-720, 1983.
- [14] R. Sierens and E. Rosseel, "Variable Composition Hydrogen/ Natural Gas Mixtures for Increased Engine Efficiency and Decreased Emissions," *Journal of Engineering for Gas Turbines and Power*, vol. 122, pp. 122-140, 2000.
- [15] E. Weber de Menezes, R. Cataluna, D. Samios and R. da Silva, "Addition of an azeotropic ETBE/ethanol mixture in eurosUPER-type gasolines," *Fuel*, vol. 85, pp. 2567-2577, 2006.
- [16] R. da Silva, R. Cataluna, E. Weber de. Menezes, D. Samios and C. M. Sartori Piatnicki,

- "Effect of additives on the antiknock properties and Reid vapor pressure of gasoline," *Fuel*, vol. 84, pp. 951-959, 2005.
- [17] R. Sonntag and G. Van Wylen, *Introduction to Thermodynamics Classical And Statistical*, John Wiley & Sons, Inc, 1991.
- [18] C. R. Ferguson and A. T. Kirkpatrick, *Internal Combustion Engines Applied Thermosciences*, New York: John Wiley & Sons, Inc, 2001.
- [19] Department of Energy, "U.S. Energy Information Administration," June 2014. [Online]. Available:
http://www.eia.gov/pub/oil_gas/natural_gas/analysis_publications/ngpipeline/index.html. [Accessed 2016].
- [20] A. J. Marchese, T. L. Vaughn, D. J. Zimmerle, D. M. Martinez, L. L. Williams, A. L. Robinson, A. L. Mitchell, R. Subramanian, D. S. Tkacik, J. R. Roscioli and S. C. Herndon, "Methane Emissions from United States Natural Gas Gathering and Processing," *Environmental Science and Technology*, vol. 49, no. 17, pp. 10718-10727, 2015.
- [21] Natural Gas Supply Association, "Natural Gas," 20 September 2013. [Online]. Available: <http://naturalgas.org/naturalgas/transport/>. [Accessed 2016].
- [22] E3 Spark Plugs, "E3's History-Making Spark Plugs," 2014. [Online]. Available: <http://e3sparkplugs.com/e3s-history-making-spark-plugs/>. [Accessed 2016].
- [23] Bosch Auto Parts, "Invention from Bosch providing reliable ignition in combustion engines since 1902," [Online]. Available: http://de.bosch-automotive.com/en/parts_and_accessories/service_parts_1/spark_plugs_1/history_1/history_1. [Accessed 2016].

- [24] Grace's Guide, "Lodge Plugs," 2016. [Online]. Available:
http://www.gracesguide.co.uk/Lodge_Plugs. [Accessed 2016].
- [25] Sparkplugs Limited, "CHAMPION SPARK PLUGS - HISTORY AND PRODUCTS," 2014.
[Online]. Available: <http://www.sparkplugs.co.uk/champion-products-history>. [Accessed
2016].
- [26] D. Seyferth, "The Rise and Fall of Tetraethyllead," *Organometallics*, vol. 22, pp. 5154-5178,
2003.
- [27] S. S. Goldsborough, "A chemical kinetically based ignition delay correlation for iso-octane
covering a wide range of conditions including the NTC region," *Combustion and Flame*, vol.
156, pp. 1248-1262, 2009.
- [28] National university of Ireland Galway, "Rapid Compression Machine (RCM)," 13 April 2005.
[Online]. Available: <http://www.nuigalway.ie/chem/rapidcm.htm>. [Accessed 2016].
- [29] C. Morley, *Gaseq*, 2005.
- [30] J. Griffiths, Q. Jiao, W. Kordylewski, M. Schreiber, J. Meyer and K. Knoche, "Experimental
and numerical studies of ditertiary butyl peroxide combustion at high pressures in a rapid
compression machine," *Combustion and Flame*, vol. 93, pp. 303-315, 1993.
- [31] P. Desgroux, L. Gasnot and L. Sochet, "Instantaneous temperature measurement in a rapid-
compression machine using laser Rayleigh scattering," *Applies Physics B LAser and Optics*,
vol. 61, pp. 69-72, 1995.
- [32] G. Kukkadapu, K. Kumar, C. Sung, M. Mehl and W. Pitz, "Autoignition of gasoline and its
surrogates in a rapid compression machine," in *Proceedings of the Combustion Institute*, 2013.
- [33] H. Curran, A. Heufer, R. Monaghan and R. Richardson, "The NUIG RCM - Data analysis and

- simulation," in *RCM Workshop*, Chicago, 2012.
- [34] J. Wurmel and J. Simmie, "CFD studies of a twin-piston rapid compression machine," *Combustion and Flame*, vol. 141, pp. 417-430, 2005.
- [35] G. Mittal and C. J. Sung, "Aerodynamics inside a rapid compression machine," *Combustion and Flame*, vol. 145, pp. 160-180, 2006.
- [36] Omegadyne, "DPG409 Series High Accuracy Digital Pressure Gauge," 2012. [Online]. Available: <https://www.omega.com/manuals/manualpdf/M4978.pdf>. [Accessed 2016].
- [37] MKS Baratron, "MKS Baratron Type 722A Absolute Pressure Transducer Instruction Manuel," 2016. [Online]. Available: <http://www.mksinst.com/Docs/R/722A-MAN.pdf>. [Accessed 2016].
- [38] Air Liquide, "High Pressure Cylinders," 2016. [Online]. Available: <https://industry.airliquide.us/high-pressure-cylinders>. [Accessed 26 September 2016].
- [39] J. Heywood, *Internal Engine Combustion Fundamentals*, New York: McGraw Hill, 1988.
- [40] J. Gatowski, E. Balles, K. Chun, F. Nelson and J. Heywood, "Heat Release Analysis of Engine Pressure Data," SAE Technical Paper 841359, 1984.
- [41] B. Lewis and G. Von Elbe, *Combustion, Flames, and Explosions of Gases*, New York: Academic Press, 1987.
- [42] C. Arcoumanis and T. Kamimoto, *Flow and Combustion in Reciprocating Engines*, Berlin: Springer-Verlag, 2009.
- [43] C. Dumitrache, N. Wilvert, A. Yalin and M. Schneider, "Laser Plasma Formation Using Dual Pulse Pre-Ionization," in *44th AIAA Plasmadynamics and Lasers Conference*, San Diego, CA, 2013.

- [44] N. Glumac, G. Elliot and M. Boguszko, "Temporal and Spatial Evolution of the Thermal Structure of a Laser Spark in Air," in *43rd AIAA Aerospace Science Meeting and Exhibit*, Reno, NV, 2005.
- [45] CAS Solution, "Substance Details CAS Registry Number: 110-05-4 CA Index Name: Peroxide, bis(1,1-dimethylethyl)," 2016. [Online]. Available: <http://www.commonchemistry.org/ChemicalDetail.aspx?ref=110-05-4>. [Accessed 26 September 2016].
- [46] CAS Solution, "Substance Details CAS Registry Number: 75-52-5 CA Index Name: Methane, nitro-," 2016. [Online]. Available: <http://www.commonchemistry.org/ChemicalDetail.aspx?ref=75-52-5>. [Accessed 26 September 2016].
- [47] CAS Solution, "Substance Details CAS Registry Number: 109-87-5 CA Index Name: Methane, dimethoxy-," 2016. [Online]. Available: <http://www.commonchemistry.org/ChemicalDetail.aspx?ref=109-87-5>. [Accessed 26 September 2016].
- [48] *CHEMKIN*, San Diego, CA: Reaction Design, 2013.
- [49] M. Mehl, W. J. Pitz, C. K. Westbrook and H. J. Curran, "Kinetic modeling of gasoline surrogate components and mixtures under engine conditions," in *Proceedings of the Combustion Institute*, 2011.
- [50] *Zero Air Safety Data Sheet*, Airgas, 2014.
- [51] M. Frenklach, "Reaction mechanism of soot formation in flames," *Physical Chemistry Chemical Physics*, vol. 4, pp. 2028-2037, 2002.

- [52] M. Frenklach and H. Wang, "Detailed modeling of soot particle nucleation and growth," in *Twenty-Third Symposium (International) on Combustion*, Orleans France, 1991.
- [53] H. Richter and J. Howard, "Formation of polycyclic aromatic hydrocarbons and their growth to soot—a review of chemical reaction pathways," *Progress in Energy and Combustion Science*, vol. 26, no. 4-6, pp. 565-608, 2000.
- [54] M. De Barros Bouchet, J. Martin, T. Le Mogne, P. Bilas, B. Vacher and Y. Yamada, "Mechanisms of MoS₂ formation by MoDTC in presence of ZnDTP: effect of oxidative degradation," *Wear*, vol. 258, pp. 1643-1650, 2005.
- [55] S. Kosarieh, A. Morina, E. Laine, J. Flemming and A. Neville, "The effect of MoDTC-type friction modifier on the wear performance of a hydrogenated DLC coating," *Wear*, vol. 302, pp. 890-898, 2013.
- [56] A. Morina, A. Neville, M. Priest and J. Green, "ZDDP and MoDTC interactions in boundary lubrication—The effect of temperature and ZDDP/MoDTC ratio," *Tribology International*, vol. 39, pp. 1545-1557, 2006.
- [57] M. De Barros Bouchet, J. Martin, T. Le-Mogne and B. Vacher, "Boundary lubrication mechanisms of carbon coatings by MoDTC and ZDDP additives," *Tribology International*, vol. 38, pp. 257-264, 2005.
- [58] M. De Feo, C. Minfray, M. De Barros Bouchet, B. Thiebaut and J. Martin, "MoDTC friction modifier additive degradation: Correlation between tribological performance and chemical changes," *Royal Society of Chemistry Advances*, vol. 5, pp. 93786-93796, 2015.

7 APPENDIX A: RAPID COMPRESSION MACHINE OPERATION

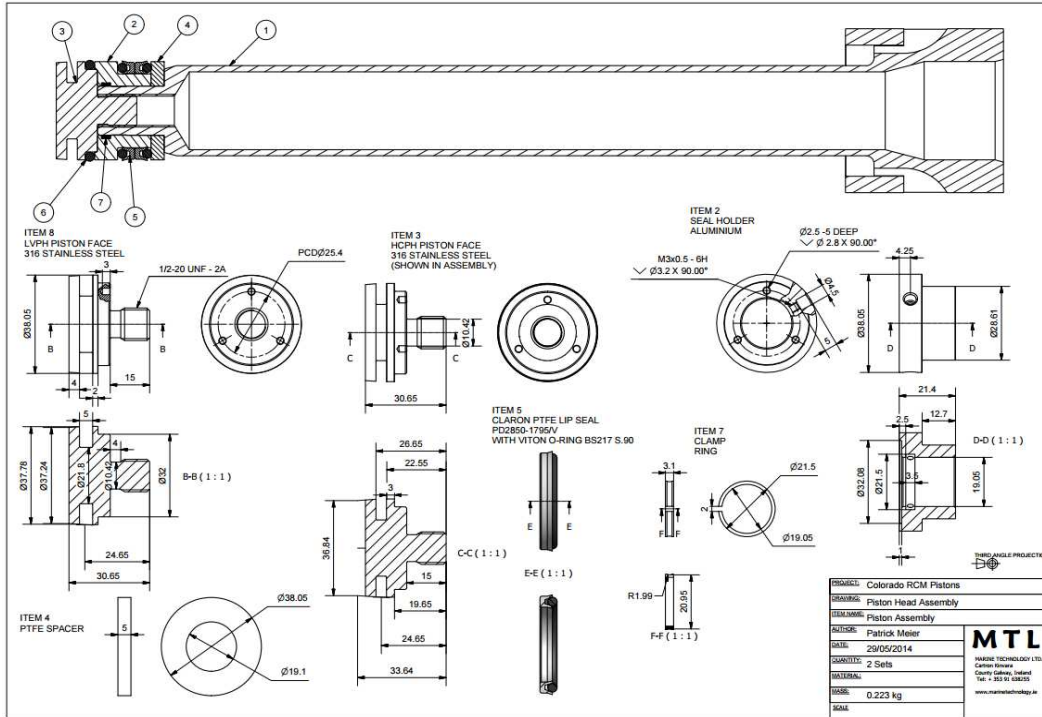


Figure 7.1 Rapid Compression Machine Piston Head Assembly.

Operate the RCM is a very involved process requiring many individual actions to be performed. The exclusion of a single step could result in the data from a test not being recorded, an expensive piece of hardware being damaged, or the test simply not operating. Therefore it is incredibly important that each step be completed correctly before moving on to the next step.

7.1 Turning the Rapid Compression Machine On

- 1) Turn lab exhaust system on.
- 2) Switch RCM vacuum pump on.
- 3) Switch RCM Main Power to ON position.
- 4) Turn RCM Power Switch to ON position.
- 5) Open RCM building air value.

- 6) Press RCM RESET button.
- 7) When the Retraction Vacuum button illuminates the RCM is ready for testing.

7.2 Firing the Rapid Compression Machine

- 1) Press the illuminated Retraction Vacuum button.
- 2) Switch on the piston retraction vacuum pump.
- 3) When the Locking Pressure button illuminates, turn off the piston retraction pump.
- 4) Open combustion chamber valve, safety ball valve, pressure indicator valve, and vacuum valve.
- 5) Open combustion chamber filling valve and vacuum the combustion chamber down.
Typically the combustion chamber is vacuumed to below 5 mbar as indicated on the digital pressure gage.
- 6) Once the Combustion Chamber has been vacuumed down to a low pressure, fill the combustion chamber with Nitrogen to a pressure of 1 bar and perform a compression test to insure that all the products of combustion from the previous test have been removed.
 - a. To perform a compression test close the combustion chamber filling valve, combustion chamber valve, safety ball valve, pressure indicator valve, and vacuum valve.
 - b. Press the illuminated Locking Pressure button to pressurize the oil chambers. The hydraulic locking pressure may need to be increased depending on the condition of the RCM seals. In which case switch the RCM into manual mode and increase the hydraulic locking pressure before continuing on to the next step.
 - c. Press the illuminated Drive Pressure button to pressurize the air chambers.
 - d. Once the RCM finishes pressurizing the air chambers, double check that the combustion chamber valve and safety ball valve are closed. Press the Kistler Charge Amplifier

measure button to turn on the combustion chamber pressure sensor, making sure that the green measure light illuminates. Press the PicoScope Go button to collect the pressure vs, time data, making sure that a blue square surrounds the Go button. Switch the illuminated Confirm Fuel Charge switch to the right.

- e. The RCM is now ready to fire. Press the illuminated Initiate button to fire the RCM.
 - f. Switch the Confirm Fuel Charge switch back to the left, and press the measure button again to turn off the pressure sensor.
- 7) Press the illuminated Retraction Vacuum button and turn the retraction pump on.
 - 8) When the Locking Pressure button illuminates turn off the retraction pump.
 - 9) Open combustion chamber valve, safety ball valve, pressure indicator valve, vacuum valve, and combustion chamber filling valve vacuuming the combustion chamber down to a low pressure.
 - 10) Once the combustion chamber has been vacuumed down to a low pressure the combustion chamber can be filled with a fuel and oxidizer mixture from the blending manifold. Fuel and oxidizer mixtures are mixed based on partial pressures using the combustion chamber pressure indicator.
 - 11) Once the combustion chamber has been filled with the fuel and oxidizer mixture close the combustion chamber valve, safety ball valve, pressure indicator valve, vacuum valve, and combustion chamber filling valve. Wait eight minutes to allow molecular diffusion to homogenize the mixture.
 - 12) After eight minutes press the illuminated Locking Pressure button, and then the illuminated Drive Pressure button.

- 13) Once the RCM finishes pressurizing the air chambers, double check that the combustion chamber valve and safety ball valve are closed. Press the Kistler Charge Amplifier measure button to turn on the combustion chamber pressure sensor, making sure that the green measure light illuminates. Press the PicoScope Go button to collect the pressure data, making sure that a blue square surrounds the Go button. Switch the illuminated Confirm Fuel Charge switch.
- 14) The RCM is now ready to fire. Press the illuminated Initiate button to fire the RCM.
- 15) Switch the Confirm Fuel Charge switch back to the left, and press the measure button again to turn off the pressure sensor.
- 16) Repeat steps 1-15 for each subsequent test.

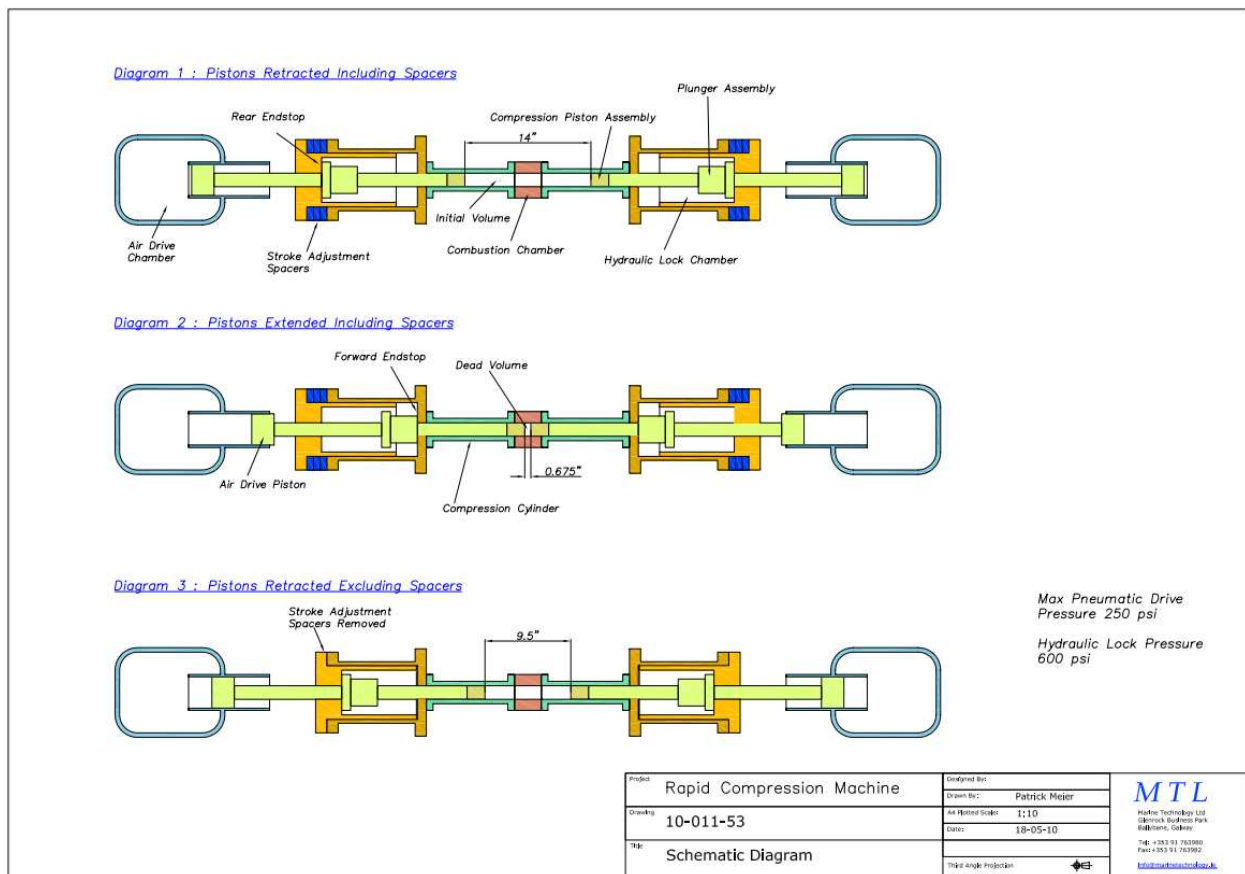


Figure 7.2 Rapid Compression Machine Piston Positions.

8 APPENDIX B: RAPID COMPRESSION MACHINE MAINTENANCE

The RCM is a complex precision tool and as such must be maintained on a regular basis. If maintained properly the RCM will continue to be key a research tool for decades to come at Colorado State University. To insure consistent operation periodic replacement of the RCM seals is required. In order to be able to access all the seals in the RCM for replacement, the entire machine must be disassembled into the individual component parts.

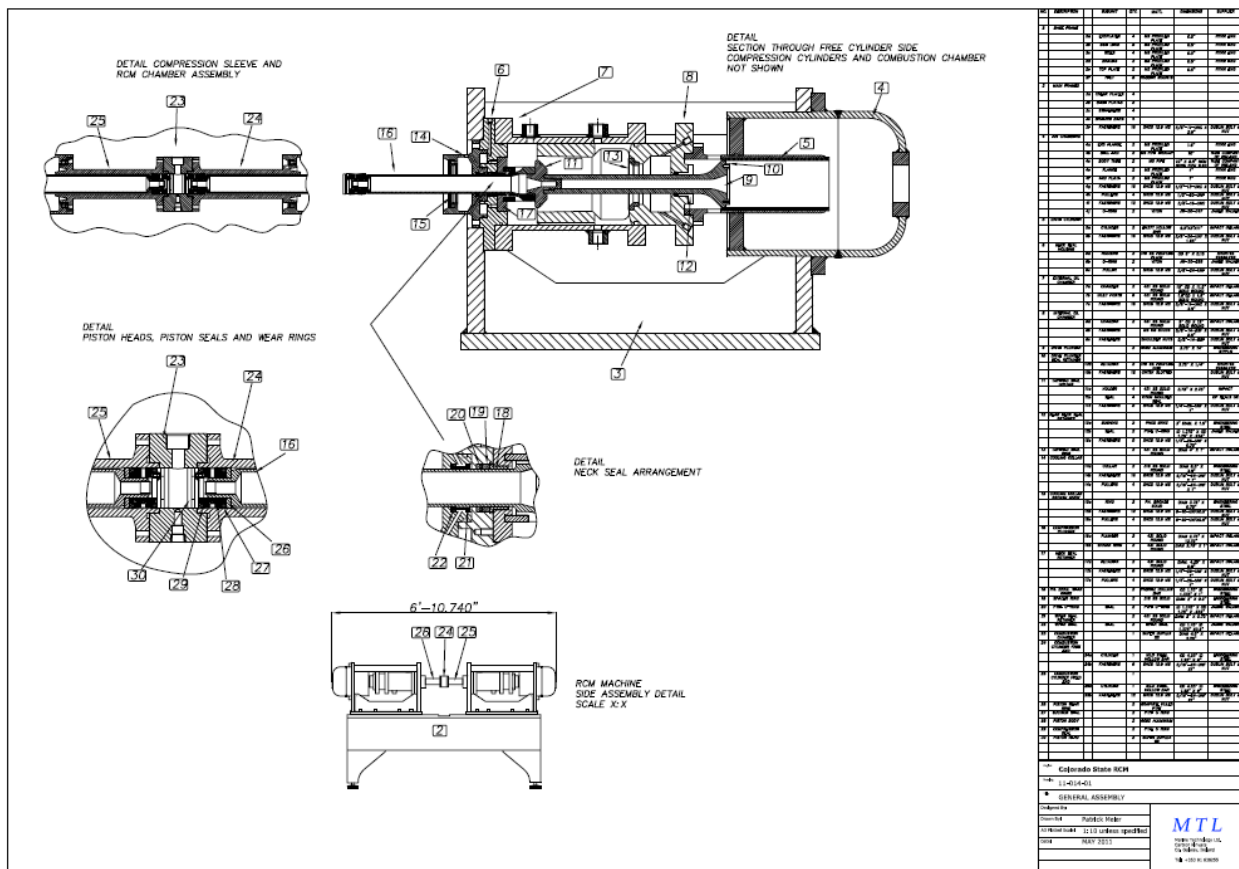


Figure 8.1 General Assembly Drawing of Rapid Compression Machine.

8.1 Rapid Compression Machine Disassembly

In order to replace the RCM seals the entire machine must be disassembled to its individual component parts. Not all the RCM's seals wear at the same rate; therefore some seals

must be replaced more regularly. Luckily the seals that wear the quickest, piston seals and wiper seals can be accessed by disassembling only the center section of the RCM.

8.1.1 Rapid Compression Machine Center Section Disassembly

- 1) Place the pistons in the retracted position.
- 2) Remove all heat wrap and heating tape from the center section of the RCM, and set aside.
- 3) Disconnect the combustion chamber filling line from the combustion chamber filling valve.
- 4) Disconnect the pressure sensor wire.
- 5) Remove the 12 combustion chamber bolts, and place in a safe place. Start by removing the six bolts that attach the combustion chamber to the Combustion Cylinder Free End, and then move on to removing the six bolts that connect the Combustion Chamber to the Combustion Cylinder Fixed End. If the fixed end bolts are removed first the Combustion Chamber and Combustion Cylinder Free End will rotate freely when the operator attempts to remove the free end bolts.
- 6) With one hand push the combustion cylinder free end into its respective cooling collar assembly, while holding the combustion chamber in the other hand to ensure that the chamber does not fall. Set the combustion chamber in a safe location.



Figure 8.2 Combustion Chamber.

- 7) Remove the 3 bolts that secure the Combustion Cylinder Fixed End, and place the bolts aside in a safe location. Remove the Combustion Cylinder Fixed End and place aside in a safe location.



Figure 8.3 Left Combustion Cylinder Fixed End, right Combustion Cylinder Free End.

8) Remove the Combustion Cylinder Free End, and place in a safe location.



Figure 8.4 Pistons in retracted position.

- 9) Go through the sequence to pressurize the hydraulic, pressurize the pneumatic sections, and fire the RCM. Making sure that nothing is in the path of the exposed pistons. Now that the pistons are in the fired position the setscrews that secure the Piston Heads to the Compression Plunger can now be accessed. Remove the entire Piston Head Assembly from the Compression Plunger and set aside in a safe location.



Figure 8.5 Right and Left Piston Head Assemblies.

- 10) Press the Retraction Vacuum button and turn on the retraction pump until the pistons return to the retracted position. Remove the 16 bolts that secure the left and right Cooling Collar, and set aside in a safe location.
- 11) Remove the left and right Cooling Collars and attached hydraulic fluid collection bottles. Set aside in a safe location. At this stage of disassembly, both the piston seals and the wiper seals can be replaced.

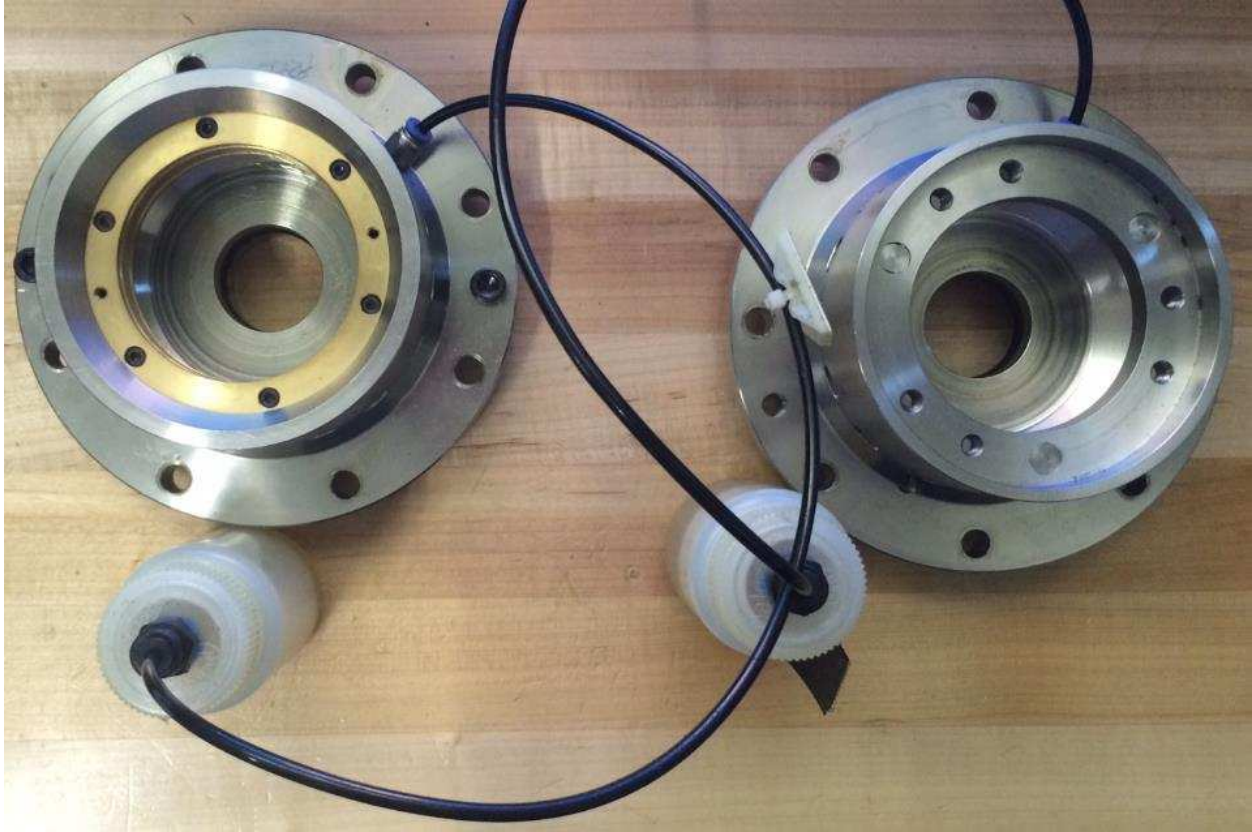


Figure 8.6 Right and Left Cooling Collars with attached Hydraulic Fluid Collection Bottles.

8.1.2 Rapid Compression Machine End Section Disassembly

The RCM has two end sections, one on the left and one on the right side of the machine. Since the two end sections are identical to one another, this section will detail how to disassemble only one of the end sections which can be repeated to disassemble the second end section. Even though the left and right end sections of the RCM are identical it is best practice to keep components from each side separate from one another to prevent future wear issues.

- 1) Drain the hydraulic fluid from the oil chamber by removing the bolt located on the bottom of the external oil chamber. Make sure to have a vessel positioned under the bolt before you begin unscrewing it. In the past a roasting pan has been used for this purpose, because the form factor of the pan allows it to be positioned below the oil chamber on the two ribs of the main frame while providing sufficient volume for the hydraulic fluid.



Figure 8.7 RCM Oil Chamber Drain Plug.

- 2) Remove the Pneumatic Filling Pipe that connects to the air chamber. Set aside in a safe location. If the Pneumatic Filling Pipe is not removed before the operator attempts to remove the linear transducer a vacuum may still exist inside the Air Chamber, which will prevent the linear transducer from being removed.
- 3) Remove the 6 bolts that secure the linear transducer. Carefully remove the linear transducer making sure to not damage the magnetic sensing rod. Set the linear transducer and associated bolts aside in a safe location.



Figure 8.8 Removing RCM Linear Transducer.

- 4) Remove the 8 bolts that secure the air chamber to the main frame of the RCM. Remove the air chamber and set aside in a safe location. Due to the weight of the air chamber and the tight tolerance between the air chamber and the RCM main frame, pusher bolts and at least two people are required to remove the air chambers.

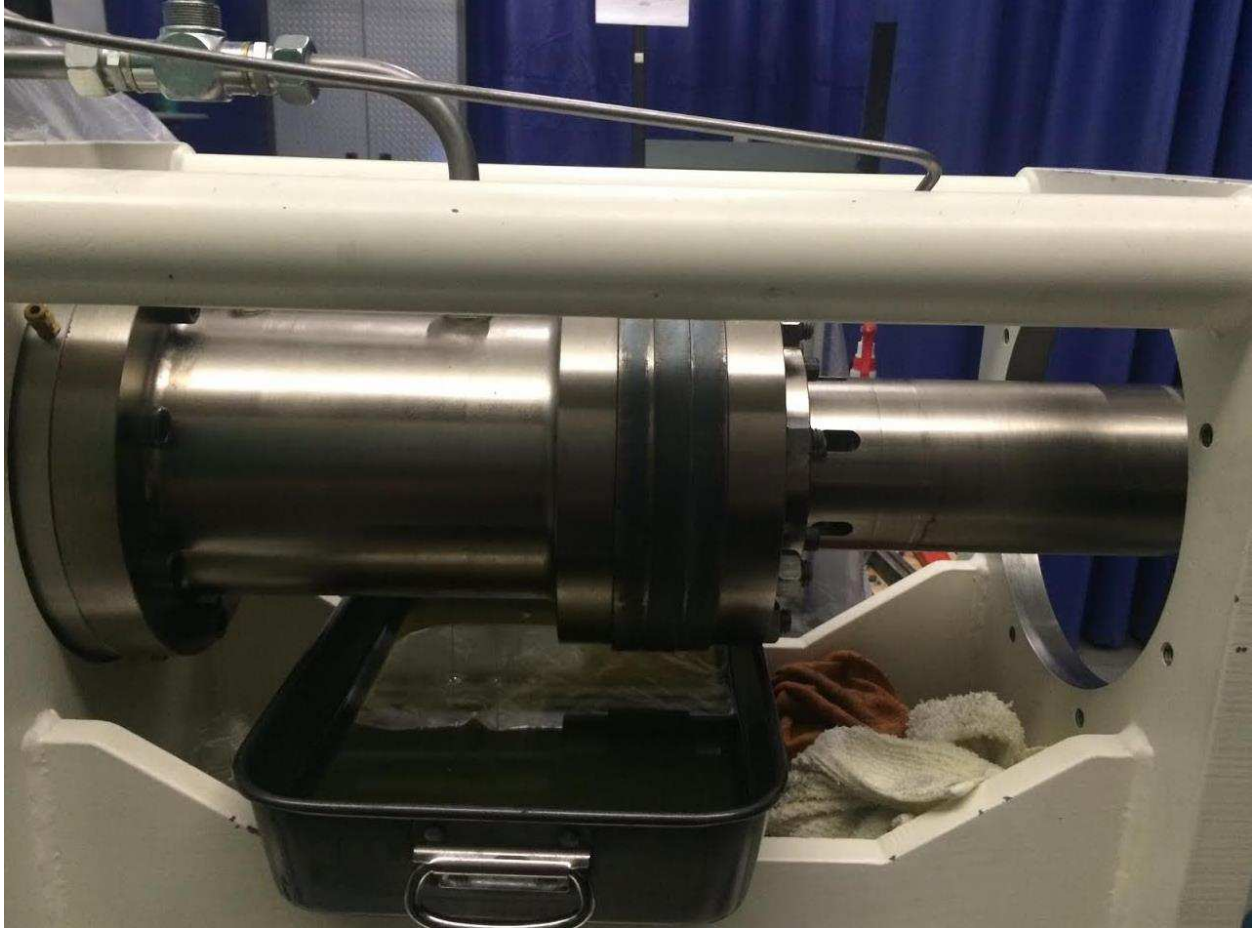


Figure 8.9 RCM with Air Chamber Removed and Hydraulic Fluid draining from External Oil Chamber into roasting pan.

- 5) Once the Air Chamber is removed manually cycle the piston to release any remaining trapped hydraulic fluid in the Oil Chamber. Make sure to have the roasting pan in position under the drain hole to prevent hydraulic fluid from flowing into the RCM Main Frame.

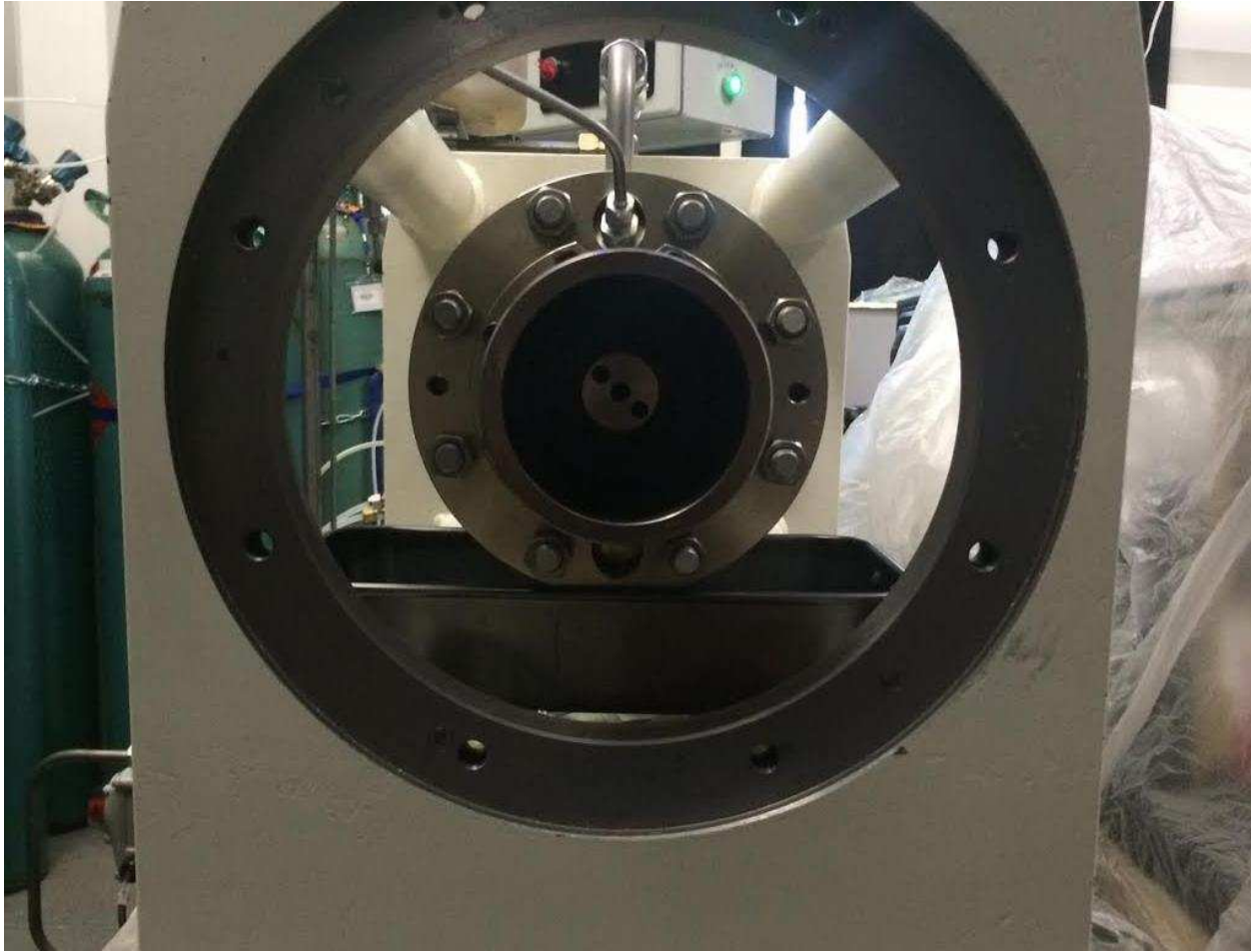


Figure 8.10 View of End of Drive Plunger, which must be manually pushed forward to release trapped hydraulic fluid.

- 6) Remove the 8 bolts that secure the Drive Cylinder to the end of the internal oil chamber. Remove the drive cylinder, making sure not to damage the drive plunger which resides inside the drive cylinder.
- 7) Disconnect the secondary hydraulic line from the Oil Chamber and allow all of the oil to drain from the central oil reservoir into a catch vessel. Once no more hydraulic fluid is draining from the secondary hydraulic line, disconnect the secondary hydraulic fluid line from the oil reservoir and set aside.

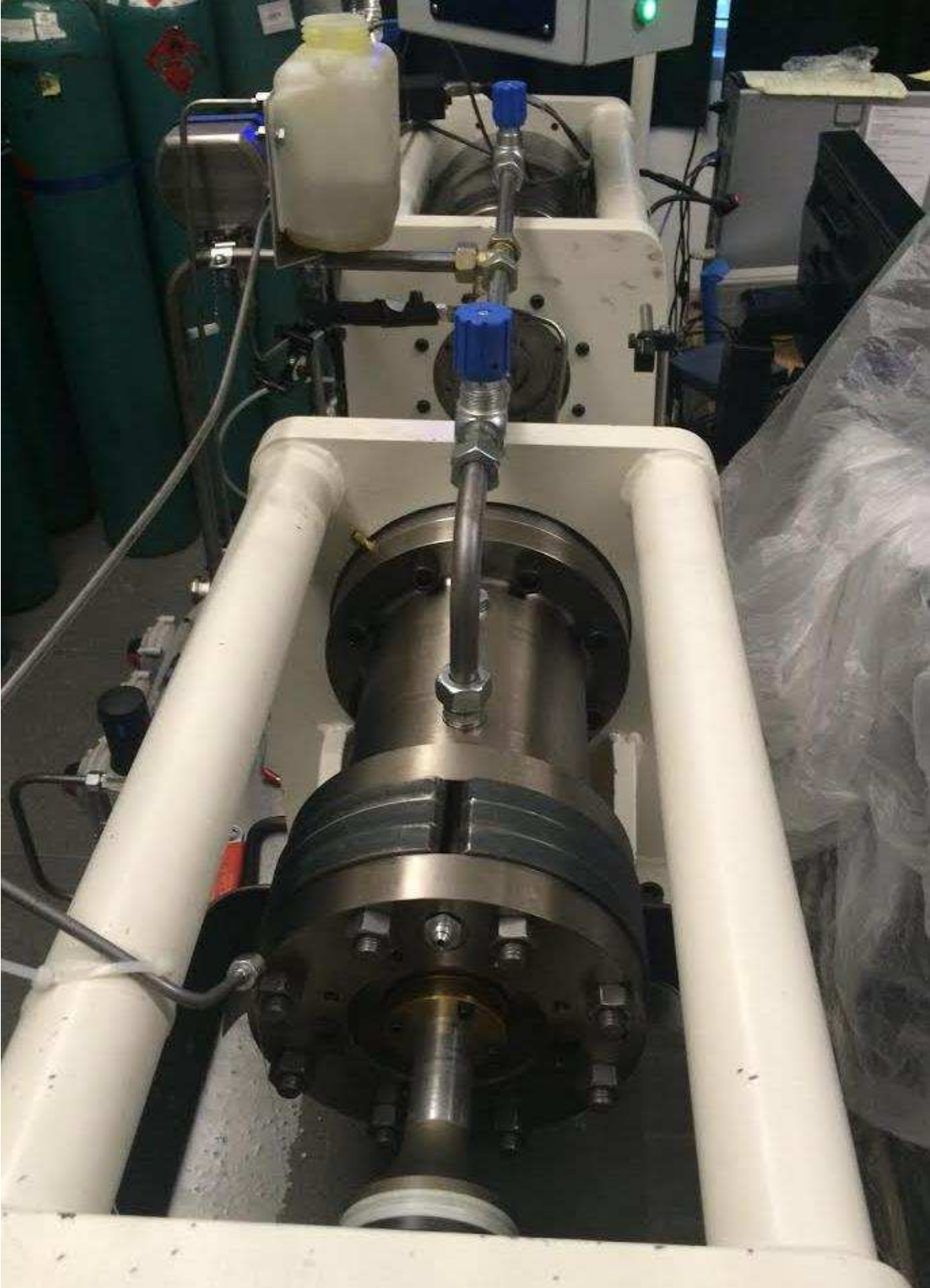


Figure 8.11 RCM with Drive Cylinder Removed and Secondary Hydraulic Line draining.

- 8) Remove the 8 nuts that secure the internal oil chamber to the external oil chamber. Remove the 6 compression spacers from between the internal oil chamber and the external oil chamber, set aside in a safe location.
- 9) Remove the internal oil chamber and drive piston assembly from the external oil chamber by pulling the internal oil chamber assembly straight back away from the RCM. Make sure to remove the internal Oil Chamber and Drive Piston Assembly in line with the RCM's major axis to prevent damaging the compression plunger. Make sure to have the roasting pan positioned underneath the end of the external oil chamber to catch any residual hydraulic fluid that did not drain out originally. Due to the mass of the internal oil chamber and drive piston assembly, the awkward position, and the slick oil coated surface two people are required to remove the internal oil chamber and drive piston assembly.
- 10) Use two strap wrenches to unscrew the Compression Plunger from the Drive Plunger and remove both pistons from the Internal Oil Chamber.



Figure 8.12 Using strap wrenches to unscrew Compression Plunger from Drive Plunger.

11) Disconnect and remove the main hydraulic line from the top of the external oil chamber.



Figure 8.13 Rapid Compression Machine Main Hydraulic Line.

- 12) Remove the 8 bolts that secure the external oil chamber and the neck seal housing to the main frame of the RCM. Once the bolts that secure the external oil chamber are removed nothing attaches the external oil chamber and neck seal housing to the frame of the RCM, therefore it is necessary to use a set of ratchet straps to support the external oil chamber. Remove the external oil chamber and neck seal housing from the RCM and set aside.



Figure 8.14 External Oil Chamber supported by Ratchet Strap.

13) The RCM has now been disassembled to a level that allows access to replace all of the RCM's different seals. To re-assemble the RCM work backwards from steps 12 to 1, working to attach the parts to the frame of the RCM instead of removing them.

9 APPENDIX C: RCM SEALS

The RCM has 15 different distinct seals located throughout the machine to prevent high-pressure gasses and fluids from escaping. Since Marine Technology Ltd. (MTL) manufactured the RCM, most of the seals come from distributors located in the United Kingdom. Due to complicated CSU purchasing policies, seal purchases were made through Patrick Meier at MTL. The one exception to this was the combustion chamber seals, which could be purchased through a domestic distributor. Table 9.1 lists the RCM's seals starting with those closest to the combustion chamber and progressing out to the air chambers.

Table 9.1 Rapid Compression Machine Seals.

Seal Name	Description	Location*	Distributor/Part#
Combustion Chamber Seal	Viton O-Ring	Between Combustion Chamber (23) and Combustion Chamber Sleeves (24)	McMaster-Carr / 9263K129 Abbey Seals / BS 225 V
Piston Seals	PTFE U-Ring and Viton O-Ring	Between Piston Head (30) and Piston Body (28)	Claron / PD2850-1795/V (U-Ring) Abbey Seals / BS 217 (O-Ring)
Wiper Seals	Radial Lip Seal	Cooling Collar (14)	Walkersele / L6T-1 USA DS-1375 1.375 WR137175-018-030M-P
Neck Seals	PTFE U-Ring and Viton O-Ring	Neck Seal Housing (6)	Claron / PU175137/1V (U-Ring)
Internal Cooling Collar Seal	Viton O-Ring	Cooling Collar (14)	Abbey Seals / BS 83370
External Cooling Collar Seal	Viton O-Ring	Cooling Collar (14)	Abbey Seals / BS 24770
Forward Hydraulic Oil Chamber Seal	Viton O-Ring	Between Seal Housing (6) and Oil Chamber (7)	Abbey Seals / BS 25670
Forward Taper Seal	Viton O-Ring	Between Taper Seal Holder (11) and Compression Plunger (16)	Abbey Seals / BS 21870
Rear Taper Seal	Viton O-Ring	Between Taper Seal Holder	Abbey Seals / BS 61770

		(11) and Drive Plunger (9)	
Rear Hydraulic Oil Chamber Seal	Viton O-Ring	Between External Oil Chamber (7) and Internal Oil Chamber (8)	Abbey Seals / BS 43370
Rear Neck Seal	Poly U-Seal	Between Internal Oil Chamber (8) and Rear Neck Seal Retainer (12)	Hallite / 605-43461
Drive Plunger Seal	Custom PTFD Seal	Between Drive Plunger (9) and the Drive Plunger Seal Retainer (10)	N/A
Air Chamber Seal	Viton O-Ring	Between Air Chamber (4) and Drive Cylinder (5)	Abbey Seals / BS 34770
Linear Transducer Seal	Viton O-Ring	between Air Chamber (4) and Linear Transducer	Abbey Seals / BS 23070
Combustion Chamber Valve Tip	Machined Peek	Between the Combustion Chamber (23) and the Needle Valve	Custom

*The numbers in parenthesis in the location column correspond to part call out numbers on the RCM general drawing, Figure 7.1.



Figure 9.1 Combustion Chamber Seals.



Figure 9.2 Piston Seals.



Figure 9.3 Wiper Seals.



Figure 9.4 Neck Seals.



Figure 9.5 Internal Cooling Collar Seals.

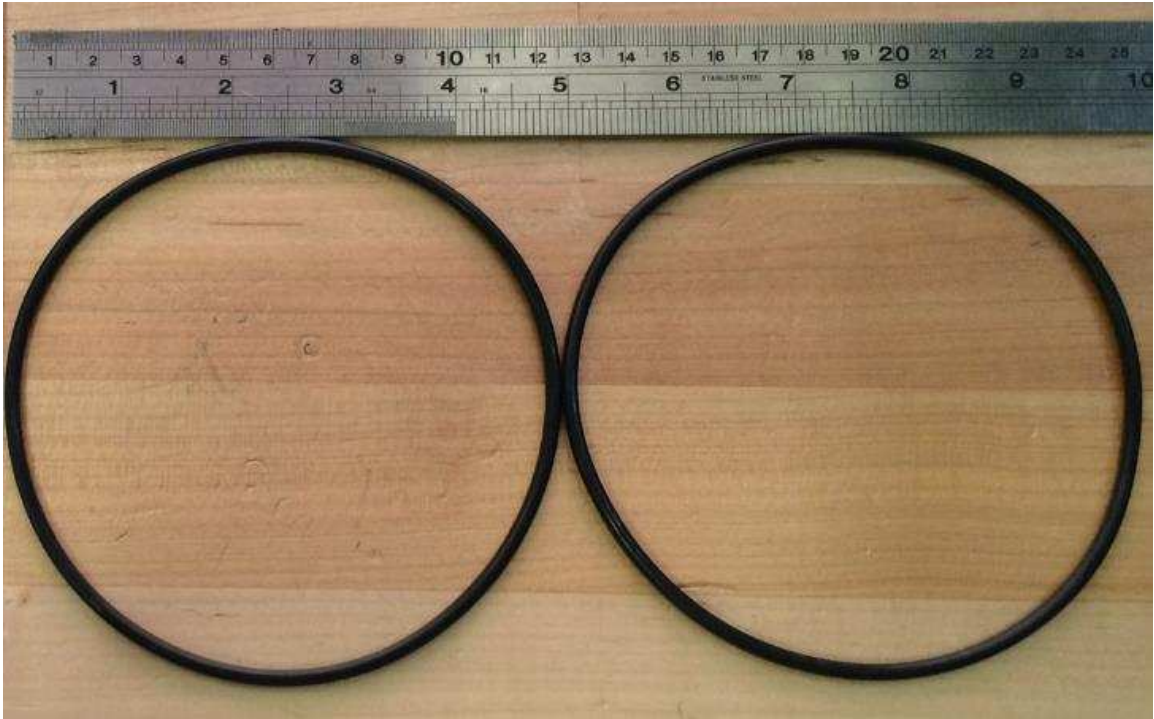


Figure 9.6 External Cooling Collar Seals.



Figure 9.7 Forward Hydraulic Oil Chamber Seals.



Figure 9.8 Forward Taper Seals.



Figure 9.9 Rear Taper Seals.



Figure 9.10 Rear Hydraulic Oil Chamber Seals.



Figure 9.11 Rear Neck Seals.

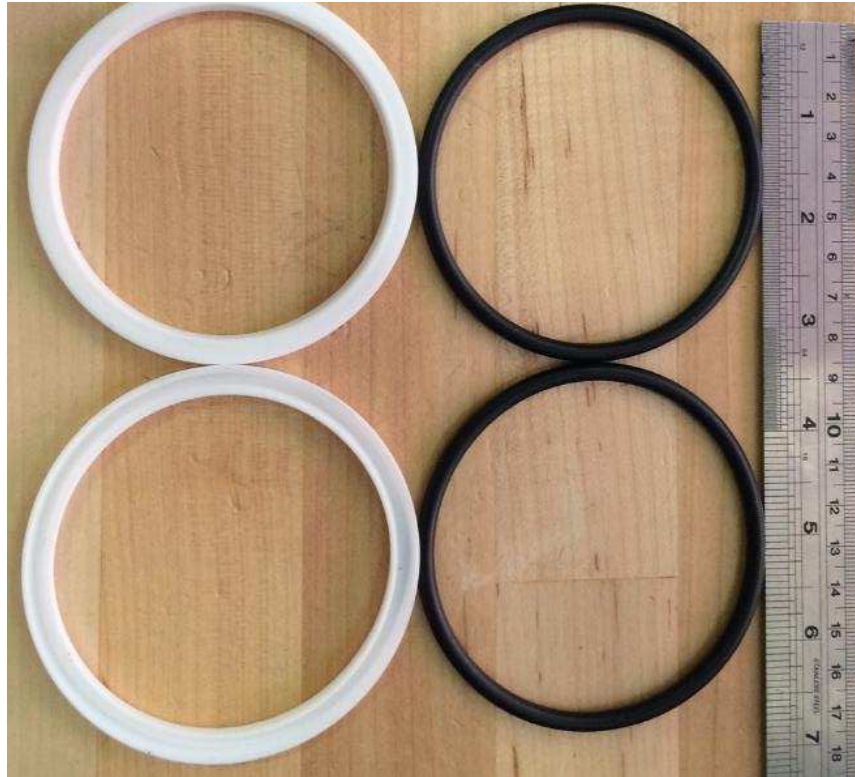


Figure 9.12 Drive Plunger Seals.



Figure 9.13 Air Chamber Seals.

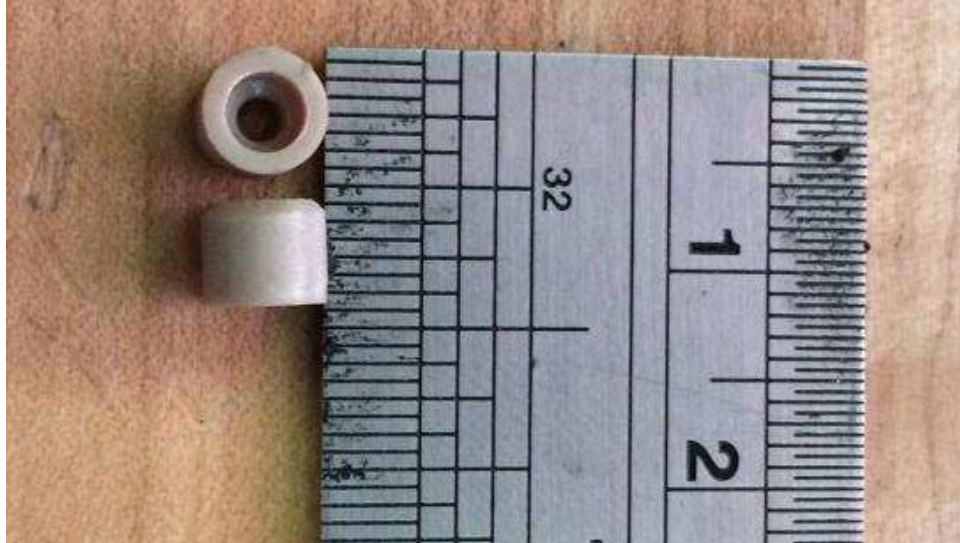


Figure 9.14 Combustion Chamber valve Tip.



Figure 9.15 Linear Transducer Seals.

10 APPENDIX D: RAPID COMPRESSION MACHINE TROUBLESHOOTING

10.1 Combustion Chamber Valve Tip Deterioration

The tip of the valve used to fill and seal the combustion chamber is made of Peek, a thermoplastic with excellent mechanical and chemical properties at high temperatures. During compression and combustion events the valve tip is one of the seals that prevents high temperature and pressure gases from escaping from the combustion chamber. However, as the valve tip becomes worn the amount of mass lost from the combustion chamber during compression and combustion events increases to an unacceptably level. Beside higher than normal mass losses, the other main symptom of the valve tip needing to be replaced is an increase in slack when closing the valve requiring the valve to be closed more than usual to obtain the same level to sealing force. Valve tip wear occurs due to two separate processes. First, repeated use over long periods of time eventually wears the tip down. However, this process can take months to occur. Second, soot formation during combustion events rapidly degrades the valve tip. In as few as two runs soot formation can ruin the valve tip. For this reason conditions that cause soot formation should be avoided.

10.2 Piston Seal Deterioration

The piston seals on the RCM are made up of a PTFE U-Ring and a Viton O-Ring that sits inside the U-Ring effectively acting as a spring to force the U-Ring between the piston and the combustion chamber sleeve. In conjunction with the valve tip, the piston seals prevent gases from escaping the combustion chamber. Piston seal wear occurs by friction between the seal and the combustion chamber sleeves during repeated firings of the RCM. The main symptoms that

the piston seals need to be replaced are increased mass losses during combustion and compression events, and an inability to vacuum the combustion chamber down to low pressures. Typically the piston seals need to be replaced about once per month.

10.3 Wiper Seal Deterioration

Under normal operation a small amount of hydraulic fluid escapes from the oil chamber even when the neck seals are working properly. To prevent this hydraulic fluid from making its way into the combustion chamber wiper seals are installed between the neck seals and the combustion chamber. Wiper Seal wear occurs from friction between the wiper seal and the drive compression plunger during normal operation. The main symptom that the wiper seals need replacing is extremely variable ignition delays. Ignition delays of the same fuel under the same conditions should only vary by approximately plus or minus 10%. Once ignition delays become more variable than plus or minus 10% it is time to replace the wiper seals. Typically wiper seals need to be replaced once every six months.

10.4 Neck Seal Deterioration

The RCM has two hydraulic fluid chambers mounted on either side of the combustion chamber which serve two specific purposes. First, prior to firing the hydraulic chambers serve to lock the drive pistons in place while the air chambers are being pressurized. Second, to slow the drive pistons as they reach top dead center after firing the RCM. In order to prevent hydraulic fluid escaping from the oil chambers a neck seal composed of a PTFE U-Ring and a Viton O-Ring is held between the neck seal housing and the compression plunger. Neck seal wear occurs due to friction between the seal and the compression plunger as the plunger is cycled back and forth during normal operation. The symptom that indicates the neck seals need to be replaced is if hydraulic pressure cannot be maintained while pressurizing the air chambers. If this is the case

the RCM will go into a fail-safe mode and quickly reduce the pressure in the air chambers by opening the releases. This occurs when the RCM detects that the hydraulic chambers are not of sufficiently high pressure to lock the pistons in place and prevent the RCM automatically firing. Typically the neck seals need to be replaced once every six months.

10.5 Non-synchronous Piston Firing

The RCM was designed to produce a laminar homogeneous adiabatic core inside the combustion chamber at the end of the compression stroke. In order to produce the adiabatic core both pistons must reach top dead center at the same time to prevent any turbulence generation. This is especially important when capturing high speed Schlieren images of combustion processes. To monitor how closely the piston positions overlap each other during compression a linear transducer records each piston's position in real time and outputs both in the PicoScope program. If the piston's positions do not closely overlap, each piston can be individually speed up or slowed down by adjusting either the left or right main hydraulic line valve to increase or decrease the rate at which pressure is reduced in the oil chambers when the RCM is fired.

10.6 Air Chamber Release Valve Not Closing

When preparing the RCM to be fired one of the last steps in the process is to pressurize the air chambers. For the air chambers to be pressurized the air chamber pressure release valve must be closed before the RCM begins pressurizing the air chambers. When the RCM is operating correctly the air chamber pressure release valve will audibly close when the Drive Pressure button is pushed and then the RCM will begin building pressure inside the air chambers. However, in certain circumstances the pressure release valve fails to close before the RCM begins attempting to pressurize the air chamber and then is unable to close once air is flowing out of the valve. In this situation the RCM has no way of sensing that the pressure release valve

is still open so the RCM will attempt to pressurize the air chamber indefinitely until the operator forces the process to stop. To correct this problem the operator must press the Emergency Stop button, then the Reset Button, and then go through the steps of retracting the pistons, pressurizing the hydraulic oil chamber and finally pressurizing the air chambers. In very rare situations the pressure release valve continues to not close after stopping and resetting the RCM as previously described. In this situation the best solution is to cycle the entire RCM off and on and then the problem will be solved. Due to the amount of time required to solve this problem it is usually best practice to vacuum the combustion chamber down and load a fresh fuel mixture just to be sure the results are accurate and repeatable.

11 APPENDIX E: RCM T_c UNCERTAINTY PROPAGATION

The temperature of the gases inside the combustion chamber of the RCM when the pistons reach Top Dead Center, but before heat transfer cools the mixture, is governed by the adiabatic compression equation.

$$T_c(T_1, \gamma) = T_1(r^{\gamma-1}) \quad (12)$$

Where T_c is the average temperature of the compressed gaseous mixture immediately before heat transfer to the combustion chamber wall begins, T₁ is the initial temperature of the mixture before the beginning of compression, r is the compression ratio of the RCM, and γ is the ratio of specific heats of the gaseous mixture. The uncertainty in being able to know T_c is a dependent on the uncertainty of the two independent variables T₁ and γ. However, since the function for T_c is a non-linear combination of independent variables interval propagation must be used to accurately constrain T_c uncertainty. The general equation used to calculate error propagation of non-linear functions is:

$$s_f = \sqrt{\left(\frac{\partial f}{\partial x}\right)^2 s_x^2 + \left(\frac{\partial f}{\partial y}\right)^2 s_y^2 + \left(\frac{\partial f}{\partial z}\right)^2 s_z^2 + \dots} \quad (13)$$

Where S_f is the standard deviation of function f, S_x is the standard deviation of variable x, S_y is the standard deviation of variable y, and S_z is the standard deviation of variable z. When the error propagation general equation is applied to the T_c function the resulting equation is as follows:

$$W_{T_c} = \sqrt{\left(\frac{\partial T_c}{\partial T_1} W_{T_1}\right)^2 + \left(\frac{\partial T_c}{\partial \gamma_{mix}} W_{\gamma_{mix}}\right)^2} \quad (14)$$

Where W_{T_c} is the standard deviation of T_c, W_{T₁} is the standard deviation of the initial temperature, and W_{γ_{mix}} is the standard deviation of the γ of the mixture. However, since the

equation for γ_{mix} is a non-linear function an error propagation is required to determine the standard deviation of γ_{mix} .

$$\gamma_{mix}(X_1, X_2) = 1 - \frac{(\gamma_1 - 1)(\gamma_2 - 1)}{X_1(\gamma_2 - 1) + X_2(\gamma_1 - 1)} \quad (15)$$

$$W_{\gamma_{mix}} = \sqrt{\left(\frac{\partial \gamma_{mix}}{\partial X_1} W_{X_1}\right)^2 + \left(\frac{\partial \gamma_{mix}}{\partial X_2} W_{X_2}\right)^2} \quad (16)$$

Where γ_1 is the ratio of specific heats for gas mixture 1, γ_2 is the ratio of specific heats for gas mixture 2, X_1 and X_2 are the mole fractions of gas mixtures 1 and 2 in the overall gas mixture. However, since X_1 and X_2 are once again non-linear functions error propagations must be performed to determine their standard deviations, W_{X_1} and W_{X_2} .

$$X_1(P_a, P_b, P_{tot,MT}, \rho) = \left(\frac{P_a + P_b}{P_{tot,MT}}\right) \rho \quad (17)$$

$$W_{X_1} = \sqrt{\left(\frac{\partial X_1}{\partial P_a} W_{P_a}\right)^2 + \left(\frac{\partial X_1}{\partial P_b} W_{P_b}\right)^2 + \left(\frac{\partial X_1}{\partial P_{tot,MT}} W_{P_{tot,MT}}\right)^2 + \left(\frac{\partial X_1}{\partial \rho} W_{\rho}\right)^2} \quad (18)$$

Where P_a is the partial pressure of constituent gas A in gas mixture 1, P_b is the partial pressure of constituent gas B in gas mixture 1, $P_{tot,MT}$ is the total pressure inside the liquid fuel mixing tank, and ρ is the volume percentage that gas mixture 1 occupies inside the RCM combustion chamber. W_{P_a} , W_{P_b} , $W_{P_{tot,MT}}$, and W_{ρ} are the respective standard deviations.

$$X_2(P_2, P_{tot}) = \left(\frac{P_2}{P_{tot}}\right) \quad (19)$$

$$W_{X_2} = \sqrt{\left(\frac{\partial X_2}{\partial P_2} W_{P_2}\right)^2 + \left(\frac{\partial X_2}{\partial P_{tot}} W_{P_{tot}}\right)^2} \quad (20)$$

Where P_2 is the partial pressure of gas mixture 2 in the RCM combustion chamber and P_{tot} is the total pressure inside the RCM combustion chamber. W_{P_2} and $W_{P_{tot}}$ are their respective standard deviations.

After calculating W_{X1} and W_{X2} , their values can be plugged into the equation for $W_{\gamma_{mix}}$. Similarly, after a value for $W_{\gamma_{mix}}$ is calculated it can be plugged into the equation for W_{Tc} . Below the uncertainty has been calculated for a compressed temperature of $T_c=864.3$ K utilizing the uncertainties of the liquid fuel mixing tank pressure transducer (0.08% of value), the RCM combustion chamber pressure transducer (0.5% of value), and the RCM combustion chamber temperature controller (± 1 K).

$$W_{X1} = \sqrt{\left(\frac{0.5}{1000 \text{ mbar}} (0.0008 * 442 \text{ mbar})\right)^2 + \left(\frac{0.5}{1000 \text{ mbar}} (0.0008 * 558 \text{ mbar})\right)^2 + \left(\frac{-0.5(442 \text{ mbar}) - 0.5(558 \text{ mbar})}{(1000 \text{ mbar})^2} (0.0008 * 1000 \text{ mbar})\right)^2 + \left(\frac{442 \text{ mbar} + 558 \text{ mbar}}{1000 \text{ mbar}} (0.005 * 0.5)\right)^2} = 0.0025$$

$$W_{X2} = \sqrt{\left(\frac{1}{1000 \text{ mbar}} (0.005 * 1054 \text{ mbar})\right)^2 + \left(\frac{-1054 \text{ mbar}}{(1054 \text{ mbar})^2} (0.005 * 1054 \text{ mbar})\right)^2} = 0.0071$$

$$W_{\gamma} = \sqrt{\left(\frac{-(1.272 - 1)(1.667 - 1)^2}{(0.5(1.667 - 1) + 0.5(1.272 - 1))^2} (0.0025)\right)^2 + \left(\frac{-(1.272 - 1)^2(1.667 - 1)}{(0.5(1.667 - 1) + 0.5(1.272 - 1))^2} (0.0071)\right)^2} = 0.0021$$

$$W_{T2} = \sqrt{((11.6^{1.38-1})(1 \text{ K}))^2 + ((304 \text{ K})\ln(1.38 - 1)(11.6^{1.38-1})(0.0021))^2} = 2.9832 \text{ K}$$

$$T_2 = 864.3 \pm 2.9832 \text{ K}$$